Polymer Masks for nanostructuring of graphene

Shvets, Violetta

Publication date:
2015

Document Version
Publisher's PDF, also known as Version of record

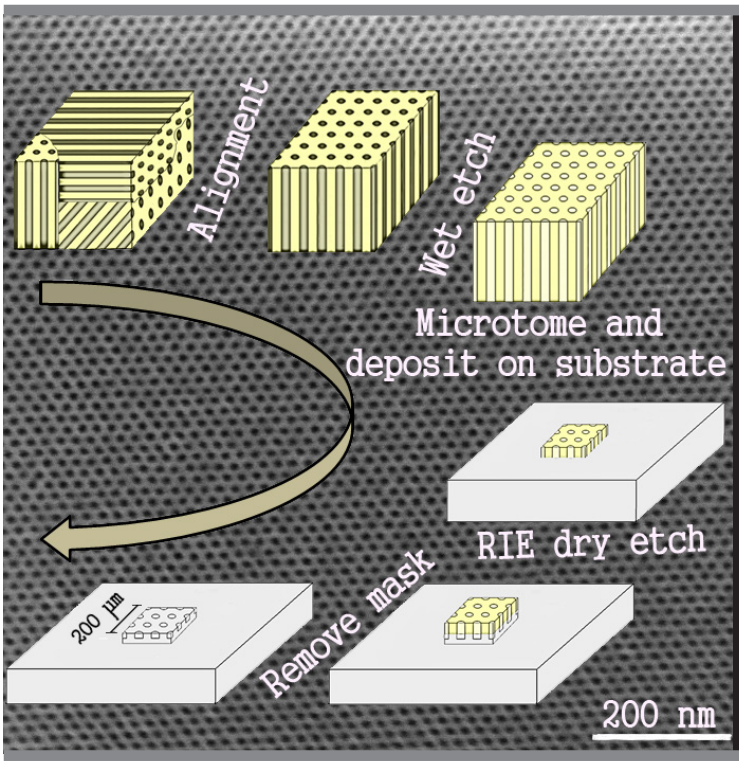

Polymer Masks for Nanostructuring of Graphene

Violetta Shvets
PhD Thesis July 2015

DTU Nanotech
Department of Micro- and Nanotechnology

Polymer Masks for Nanostructuring of Graphene

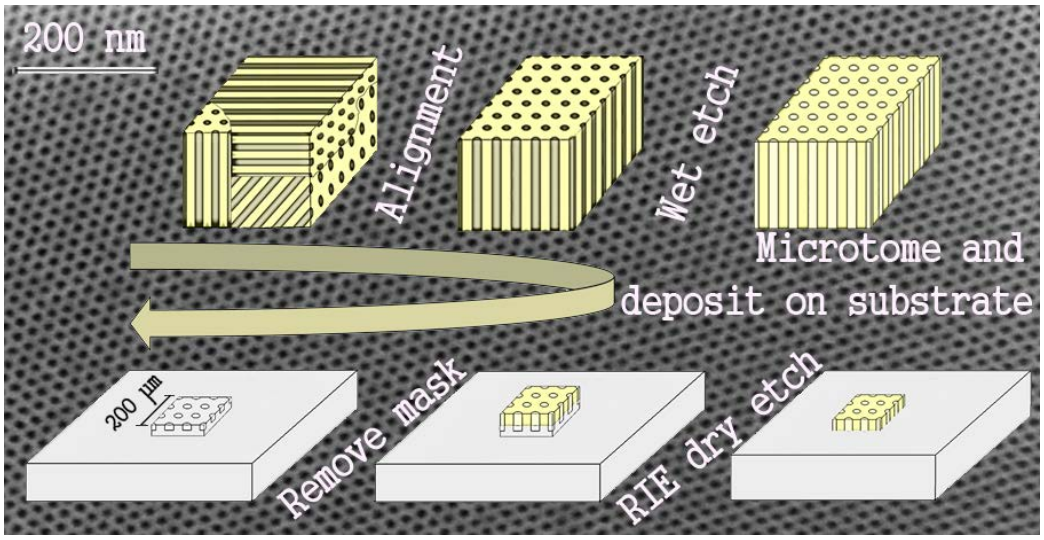

Violetta Shvets

Ph.D Thesis

July 2015

DTU Nanotech
Department of Micro- and Nanotechnology

Table of Contents

Acknowledgements

The work presented here as PhD thesis was carried out at the Center for Nanostructured Graphene, at the Department of Micro- and Nanotechnology, Technical University of Denmark (DTU) for the period from August 2012 to August 2015. Microtoming was performed on Leica EMFCS ultracut UCT microtome at the Department of Chemical Engineering at DTU. Conventional block copolymer lithography and pattern transfer were performed at the National Center for Micro- and Nanofabrication DTU Danchip. The PhD study was financed by CNG project 65370.

First of all, I would like to thank my supervisor, senior scientist Sokol Ndoni and co-supervisors, professors Kristoffer Almdal and Peter Bøggild, for their great support, help and guidance during my time at the DTU.

I wish to express my appreciation to people, who helped me with experimental part: Alberto Cagliani for his guidance on conventional block copolymer lithography, Lars Schulte for polymer synthesis, Sozaraj Rasappa and Zhongli Wang for etching recipes, Lene Gammelgaard for graphene device fabrication, David Mackenzie for Raman measurements and for electrical measurements of back gated graphene devices.

I am grateful to all, who helped me to improve my PhD thesis: Peter Bøggild, Maksym Plakhotnyuk, Paramita Das and Lars Schulte. Special thanks to Sokol for the help with translation to Danish.

Abstract

This PhD project is a part of Center for Nanostructured Graphene (CNG) activities. The aim of the project is to develop a new lithography method for creation of highly ordered nanostructures with as small as possible feature and period sizes. The method should be applicable for graphene nanostructuring and allow electronic transport studies afterwards. To achieve this goal self-assembly properties of block copolymers are exploited. Micro phase separation in block copolymers can provide well-defined morphologies with nanometer-size features. A new lithography method utilizing *ex-situ* fabricated polymer masks is developed. Mask fabrication is realized by microtoming of 30-60 nm thin sections from pre-aligned polymer monoliths with different morphologies. The resulting polymer masks are then transferred to both silicon and graphene substrates. Hexagonally packed hole patterns with 10 nm hole diameter and 20 nm periodicity are successfully transferred to both substrates. The method allowed to realize the first ever transfer of moiré patterns to silicon. Furthermore, in collaboration with CNG, device with nanostructured graphene are fabricated and electrical measurements made on these devices demonstrated the opening of what could be interpreted as a band gap.

Dansk Resumè

Ph.D. projektet er del af forskningsaktiviteterne som foregår i Center for Nanostrukturerede Graphene (CNG) på DTU. Formålet med projektet er at udvikle en ny litografisk metode baseret på selvorganisering af blok copolymerer (BCP), som kan bruges til fabrikationen af ordnede nanostrukturer på silicium og endnu vigtigere, på graphene. Kontrolleret nanostrukturering forventes at åbne et elektronisk energigab (eller båndgab) i graphene som kan muliggøre fabrikationen af graphene-baserede dioder og transistorer. Selvorganiserende BCP kan danne veldefinerede strukturer i nanometer-skala. Den nye litografi metode benytter sig af polymer masker fremstillet *ex-situ* ved hjælp af mikrotomering, som er forskellig fra den traditionelle metode hvor maskerne bliver fremstillet *in-situ*, vha. BCP spin-casting direkte på substratet. 30-60 nm tynde sektioner, med typiske størrelse på 200 x 300 μm^2 bliver mikrotemeret ud af makroskopiske nanoporøse polymer prøver med forskellige morfologier. De resulterende polymer masker overføres derefter til både silicium og graphene substrater. Mønstre af heksagonalt pakket huler med en periode på 20 nm og hul diameter på 10 nm overføres til begge substrater vha. reaktiv ion ætsning. Som en sidegevinst kunne vi vha. den nye metode opnå den første nogensinde overførsel af moiré mønstre på silicium. Endvidere, vha. elektriske målinger lavet i samarbejde med en anden gruppe på CNG, kunne vi demonstrer åbningen af et muligt båndgab på ca 20 meV på vores nanostrukturerede graphene.

Abbreviations

AFM atomic force microscopy

BCC body centered cubic

BCP block copolymer

BSE back scattered electrons

CNG center for nanostructured graphene

CNP charge neutrality point

$C_{\perp}$ cylinders perpendicular to the substrate

$C_{\parallel}$ cylinders parallel to the substrate

CVD chemical vapor deposition

D or dis disordered

DSA directed self-assembly

DTU Technical University of Denmark

DUV deep ultraviolet lithography

E_F Fermi energy

EUV extreme ultraviolet lithography

f volume fraction of the block

FET field-effect transistor

FL full surface-parallel lamellar morphology

GYR gyroid

HEMA 2-hydroxyethyl methacrylate

HEX hexagonally packed structure

HL half lamellar

HPL hexagonally perforated lamellar

HSQ hydrogen silsesquioxane

HY hybrid

ICP inductive coupled plasma

LAM lamellar

M_n number-average molecular weight

M_w weight average molecular mass

N degree of polymerization

nPB nanoporous polybutadiene

ODT order-disorder transition

OPD optical path difference

TBAF tetrabutyl ammonium fluoride

THF tetrahydrofuran

PB-b-PDMS 1,2-polybutadiene-*block*-polydimethylsiloxane

PB-b-PS polybutadiene-*block*-polystyrene

PDI polydispersity index

PDMS polydimethylsiloxane

PL perforated lamellar

PMMA poly methyl methacrylate

PS polystyrene

PS-b-PDMS poly(styrene)-block-polydimethylsiloxane

PS-*b*-PLMA poly(styrene)-block-poly(lauryl methacrylate)

PS-b-PMMA poly(styrene)-block-poly(methyl methacrylate)

PS-OH hydroxyl-terminated Polystyrene

PS-r-PMMA poly(styrene)-random-poly(methyl methacrylate)

rCP random copolymer

Rg radius of gyration

RIE reactive ion etching

rpm rotations per minute

S spherical morphology

SE secondary electrons

SEM scanning electron microscopy

TEM transmission electron microscopy

Tg glass transition temperature

TTG trivial transfer graphene

UV ultra-violet

Thesis structure

The PhD thesis begins with a literature overview and a presentation of basic principles of the used experimental methods. A number of different paths were followed in the course of the thesis work, as schematically illustrated in fig. 0.1. The experiments start with evaluation perspectives of single-lamellae mask preparation by wet etching, shortly described in subchapter 3.4. An attempt to reproduce results of conventional block-copolymer lithography by following a recipe from the literature is described in the chapter 4. This chapter is concluded by demonstration of pattern transfer to silicon.

The main activity of my PhD study has been the development of a microtome-based method for graphene nanostructuring. The concept was proved by pattern transfer to silicon (chapter 5). Nanoporous polymer monoliths with different morphologies were tested for mask preparation and pattern transfer. This approach appeared to be the most fruitful. Several patterns were transferred from the hexagonal morphology. A nanomesh was transferred to silicon from masks cut perpendicular to the cylinder axis. Moirè patterns were transferred in the case of two superimposed masks. By cutting at 45° to the cylinder axis, masks with elliptical pattern were obtained and corresponding slit-like patterns were transferred to silicon. Cutting parallel to the cylinder axis gave multilayer mask and transferred line pattern was unclear. Masks were cut off a nanoporous gyroid monolith and etching led to formation of HEX pattern overlapping with lines or waves. Masks from lamellar monoliths could not be prepared since polymer disintegrated during cutting.

The final chapter 6 is devoted to graphene. The microtome-based method was applied with minor changes and highly ordered graphene nanomeshes were successfully obtained. Back gated nanopatterned graphene devices were fabricated for transport measurements. An approach to create periodic strain superlattice by depositing graphene on a nanopillar array is tested (6.3). A schematic map of the thesis experimental part is drawn in fig. 0.1. Two types of precursors were used: bulk monoliths for ex-situ mask preparation and block copolymer solutions for traditional lithography. After the fabrication of the mask, an etching recipe is chosen and optimized. One recipe with oxygen-containing plasma is used to transfer pattern to graphene, while fluorine-containing plasmas are used for pattern transfer to silicon. The different types of obtained pattern are collected in the last column of fig. 0.1.

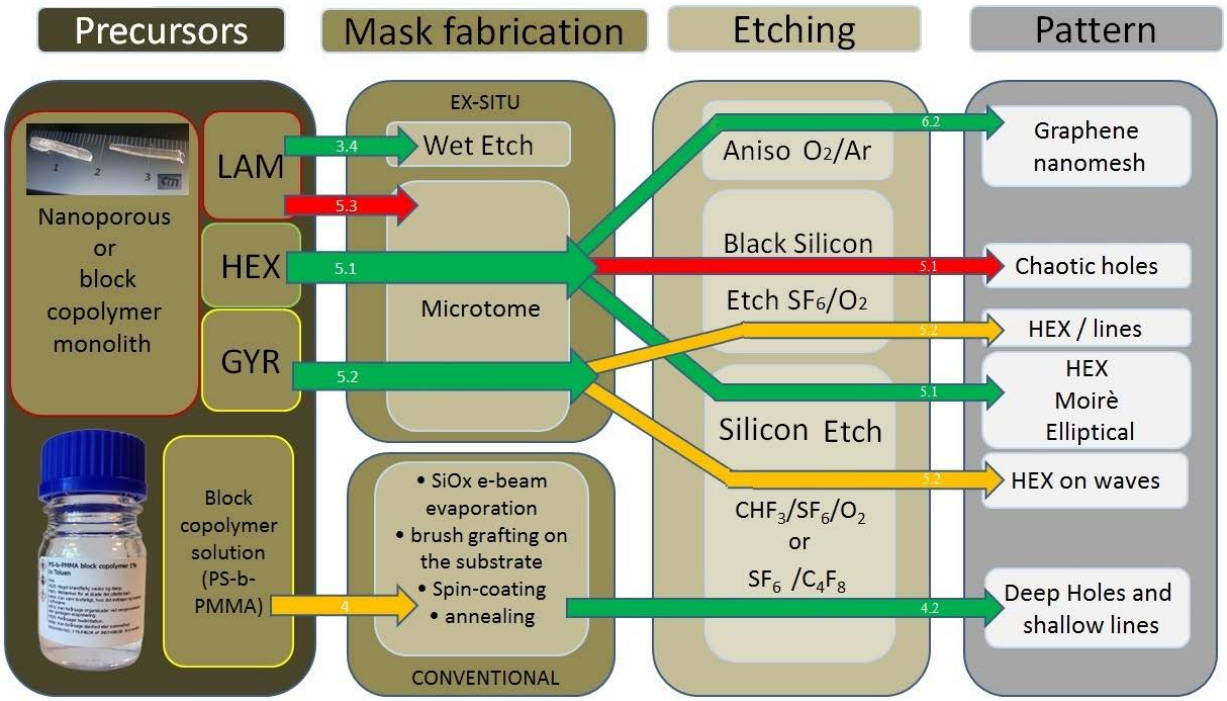

Fig. 0.1. Schematics of lithography methods realized in the thesis. Numbers on arrows refer to the chapter or subchapter, where the method is described. Colors of the arrows show how successful the respective methods: red – failure, yellow – partial success, green – success.

1. General introduction

This year "Moore's law", *i.e.* the observation that the number of transistors in a dense integrated circuit doubles every two years, became 50 years old. Silicon electronics is coming close to its limits, and building of the new post-silicon microelectronics is required. One of the promising materials to use in the post-silicon electronics is graphene. It is atomically thin and has large electrical and thermal conductivity, but the absence of a bandgap does not allow for an effective switching off of graphene transistors. Transforming graphene into an intrinsic semiconductor is important for both scientific studies and industrial fabrication of new devices [1].

1.1. Graphene and its properties

In 2010 Nobel Prize was given “for groundbreaking experiments regarding the two-dimensional material graphene” discovery of graphene and its properties investigation. Firstly isolated in 2004 [2], graphene is a single layer of the 3D graphitic crystal, an atomically thin 2D material, consisting of carbon atoms forming a honeycomb structure (Fig.1.1.1.). The covalent bonds between carbon atoms are formed by sp^2-hybridised orbitals.

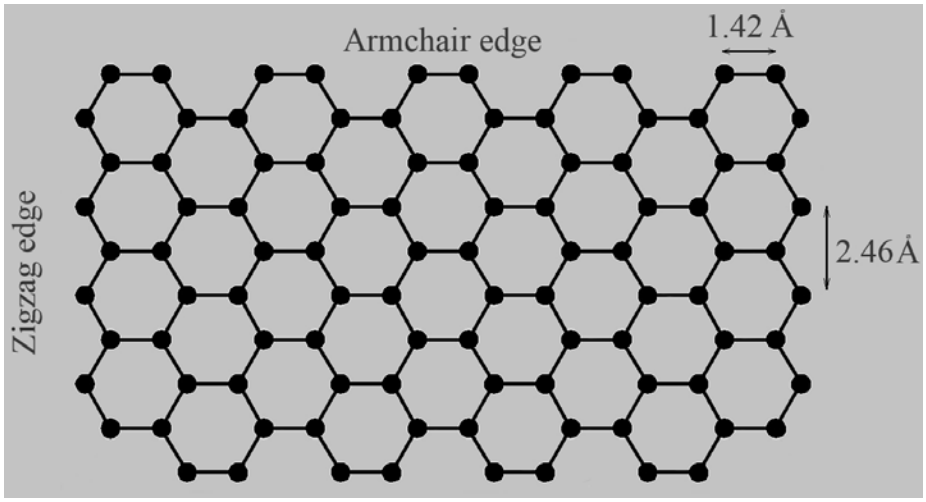

Fig. 1.1.1. Graphene atomic structure.

Graphene is very light material with huge surface area of 2630 m^2/g [3], the strongest material ever measured [4], with exceptional ability to retain its initial size after mechanical strain [5]. Its electronic properties include room temperature Hall effect, ballistic transport, high charge

carrier mobility 200 000 cm^3/v^2 [6] and huge sustainable currents (9108 A/cm^2). It is the best known electrical and thermal conductor [2]. All these exceptional properties made it very promising material for the future post-silicon electronics.

The electronic band structure of graphene was predicted theoretically [7] and confirmed experimentally [8]. Energy dispersion relation ***E(k)*** for graphene is shown in fig. 1.1.2. Six locations in momentum space in the corners of the Brillouin zone are called Dirac points. For low energies the dispersion relation is linear, with the conical valence and conduction bands meeting in the Dirac point, where the density of states is zero. Material with such electronic structure can be referred as zero-gap semiconductor.

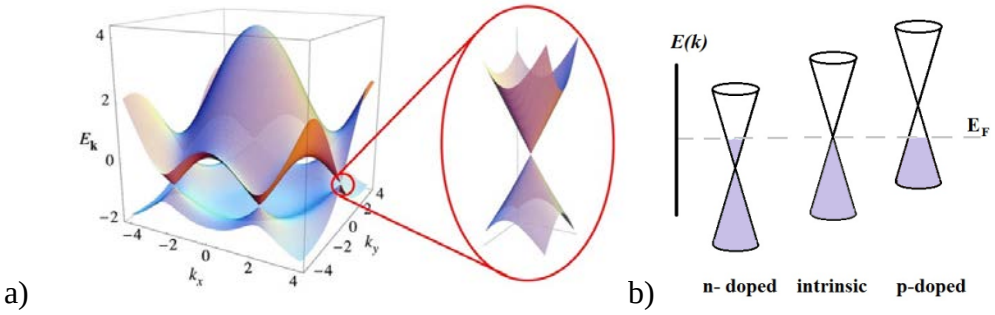

Fig.1.1.2. a) Electronic dispersion with zoom in of the energy bands close to one of the Dirac points. [9]. b) Doping shifts the Fermi level away from the Dirac point.

In graphene, electrons (or holes) transferred to graphene shift the Fermi level (E_F) away from the Dirac point (fig. 1.1.3 b) and increase its electrical conductivity. In n-doped graphene E_F is shifted towards the higher energies, while in p-doped it shifts towards the lower energies. This property gives rise to unique field-effect characteristics of graphene transistors. The first graphene transistor was presented by Manchester group in 2004 [2]. It was a back-gate transistor, where a 300-nm SiO_2 layer underneath the graphene served as a back-gate dielectric and a highly doped silicon substrate acted as the back-gate (Fig. 1.1.3 a).
Typical conductance vs. gate voltage (transconductance) characteristics of graphene transistors has a “V” shape (Fig. 1.1.3b) due to the zero bandgap. Gate voltage between the channel and the gate controls the type of charge carrier (electrons or holes) and carrier density. At large positive gate voltage electrons will accumulate in the channel, leading to so-called n-type channel. At large negative gate voltages, holes will accumulate in the channel (p-type channel) and current will flow due to hole conductance. These two modes of electron and hole

conductance form two branches of transconductance characteristics with the minimum current at the so called charge neutrality point (CNP), where the Fermi energy is at the Dirac point. The CNP position can be shifted by graphene doping or any charge presence on interfaces. Commonly on–off ratios reported for graphene devices are in the range 2–5 at the room temperature, which is too low for most real applications [1].

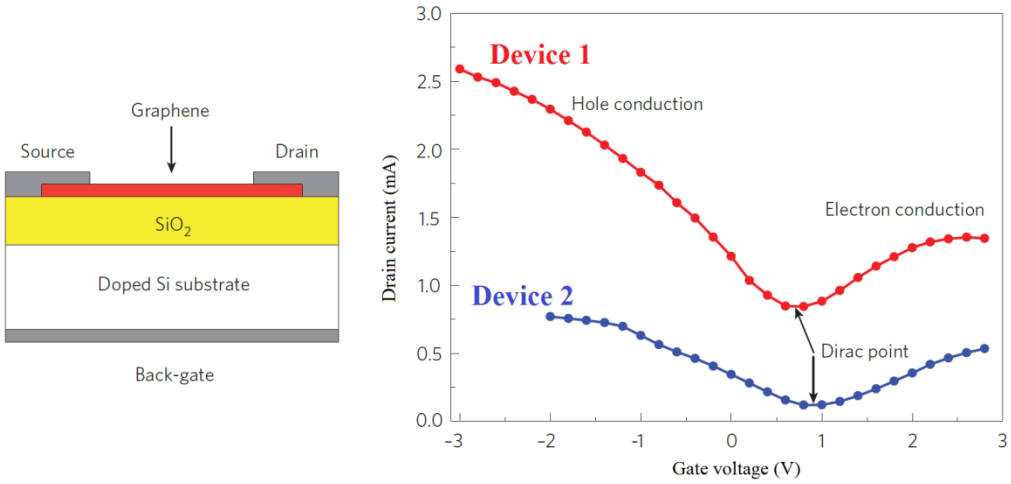

Fig. 1.1.3. Schematic of the back-gate transistor [1] with graphene as the channel and typical transfer characteristics [1, 10, 11] for real devices with graphene.

A high on/off current ratio is necessary for many electronic applications and can be achieved by opening of an energy bandgap in graphene. Recent theoretical works [12] predicted that fabrication of periodic/ quasiperiodic modulation on graphene will lead to sub-band formation. A gap can be opened by selective doping. Selective hydrogen absorption on moiré pattern of clean graphene on Ir(111) led to formation of a significant well-defined gap with the top of the observed ππ-band 450 meV below the Fermi level [13]. Opening of series of minigaps was reported in periodically rippled high quality epitaxial graphene [14].

Band gap opened in graphene nanoribbon is inversely proportional to its width [15], depends on nanoribbon crystallographic orientation
and edge passivation [16]. In graphene nanomeshes, the energy gap is sensitive to the hole edge configuration, lattice orientation and when a strong disorder occurs, energy gap scaling inversely to the nanomesh neck width [17]. A true band gap emerges from periodicity-induced confinement, but there is also transport gap, that emerges from edge and bulk disorder.

Disorder in shape, position and presence of any atomic imperfections and substrate impurities affect the electronic transport properties in graphene nanomesh [18]. Transport gap and a true band gap are difficult to distinguish experimentally.
One of the common ways to create graphene nanoribbon arrays and selectively etched meshes is block copolymer lithography. This work focuses on development of a method of fabrication of the most ordered meshes with small feature sizes, utilizing self-assembling properties of block copolymers.

1.2. Block copolymer morphologies

Block copolymers (BCP) are polymers that have in their chain two or more regions consisting of chemically distinct chain units, called blocks. Depending on the number of blocks, block copolymers are called diblocks (2 blocks), triblocks (3 blocks), tetrablocks (4 blocks) and multiblocks (5 and more blocks). Star block copolymers are block copolymers where all polymer chains are connected to a central core. The current project is focused on diblock copolymers and their ability to self-assemble in 5-50 nm periodic structures. At thermodynamic conditions of immiscibility between the blocks, chain units of different types repel each other, but cannot completely separate into two phases because they are covalently linked. By minimisation of the repulsive interaction and maximisation of attractive interaction, block-copolymers spontaneously pack into regular structures [19]. The process is called microphase separation.

Multiple parameters are utilized for the description of diblock copolymer behavior. The interaction energy between different blocks is described by the *Flory–Huggins* interaction parameter χ. χ is larger for more incompatible blocks and decreases with the increase of temperature [20]. The polymerization degree is described by N, which is the total number of chain units in the polymer. The composition of block copolymer is expressed in terms of volume fractions f of one of the blocks. In a given real sample polymer molecules have different lengths. Molecular mass distribution is described by the polydispersity index (PDI). PDI is the ratio between weight average molecular mass M_w and number average molecular mass M_n.

$$PDI = \frac{M_w}{M_n}\ ;\ M_w = \frac{\sum_i n_i M_i^2}{\sum_i n_i M_i};\ M_n = \frac{\sum_i n_i M_i}{\sum_i n_i}\ ;$$

where n_i is the number of molecules with mass M_i.

The size of the polymer chain can be characterized by radius of gyration R_g. R_g characterizes the size of the polymer chain as an average of the squared distance over all units from the mean position:

$$R_g^2 = \frac{1}{N}\sum_{k=1}^{N}(\boldsymbol{r}_k - \boldsymbol{r}_{mean})^2$$

In theoretical studies a polymeric chain is described with the bead-spring model. In this model the polymer chain is discretized into a number of beads, linked by Hookean springs. Each bead consists of many chain units. For convenience, chain units and beads have equal size for different blocks. This model is called conformationally symmetric diblock copolymer. Behavior of an infinite melt of diblock copolymer can be to a first approximation described in terms of χN and f. Microphase separation leads to formation of different morphologies depending mainly on these two parameters (fig. 1.2.1.). Equilibrium morphologies of diblock copolymer comprise body-centred cubic (BCC), hexagonally packed cylinders (HEX), lamellae (LAM) and gyroid (GYR) morphologies. If χN is below the critical value of 10.5, only disordered phase (dis) exists. Because χ is roughly inversely proportional to temperature, order in a BCP system can be destroyed by heating above a temperature called order-disorder transition (ODT) temperature. For a given χ the ODT temperature decreases with the decrease of N. Polymers with higher χ are required to achieve the smallest possible size and pitch of self-assembled structures.

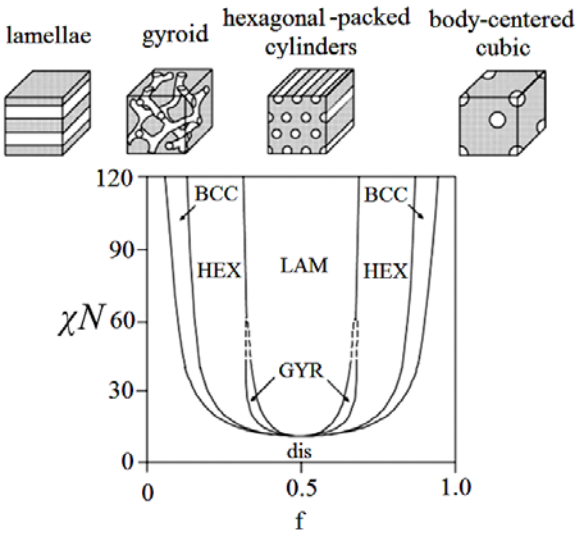

Fig. 1.2.1. Illustrations of the equilibrium morphologies and theoretical phase diagram for a conformationally symmetric diblock copolymer, calculated using self-consistent mean field theory [21].

Typically four regimes of block-copolymer interaction are distinguished: disordered, weak segregation, intermediate segregation and strong segregation [22, 23]. These regimes are the most studied for symmetric LAM example. For $\chi N \ll 1$, interaction between different types of chains is sufficiently weak and copolymer melt is disordered. If the parameter is around 10.5 ($\chi N \cong 10.5$), weak-segregation regime occurs, where profile can be well approximated by sinusoid. Intermediate regime ($50 > \chi N > 12$) has narrow interfaces between blocks. In the strong segregation regime ordered domains are essentially pure (f > 0.9999) and occupied almost exclusively by one specious.

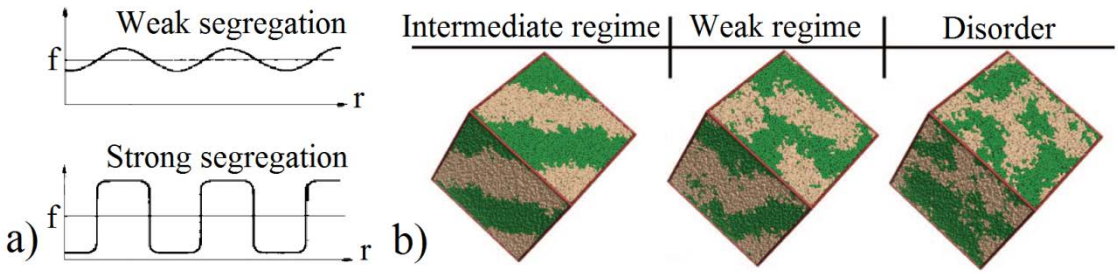

Fig. 1.2.1. Illustrations of the segregation regimes in a symmetric LAM BCP: a) block fraction profiles for weak and strong segregation regimes [22] and b) computer simulation for intermediate, weak and disorder regimes [24].

Period of microdomain structure *D* in strong segregation conditions scales as [25]:

$D \sim N^{\frac{2}{3}} \chi^{\frac{1}{6}}$

In real BCP polydispersity and symmetry of the molecular weight distribution between the blocks can affect the forming structure and lead to stabilization of the metastable morphologies as hexagonally perforated lamellae (HPL) [26] or cause two-phase coexisting regions [27]. Equilibrium phases calculated theoretically were discovered experimentally. Spontaneous microphase separation in the bulk polymer will lead to formation of multi-domain structure with random orientation. An effective and easy way to align bulk polymer melts is by directional shear flow caused by application of mechanical shear [28, 29, 30].

If BCP is confined in a thin film, many more parameters appear and the phase diagram become complex. Important parameters as film thickness and interaction with each of the two interfaces for both blocks are added. Calculations only in the case of equal interfaces and low thicknesses (below $8R_g$) give 20 different morphologies for only two parameters to vary: film thickness and ratio between blocks (Fig.1.2.2). Some of the morphologies may be quite difficult to distinguish experimentally. For example, two different $C_{\perp,}$ S_1 and SC have no sharp phase borders and smoothly transform into each other. In the diagram the perforated lamella (PL) morphology becomes stable and can be interpreted as gyroid in the thin film regime. Vertical dashed lines in fig. 1.2.2. show the borders between bulk morphologies, and they don't match the thin film phase borders. For example, BCP giving spherical morphology in the bulk can have lamella structure ($L^{\parallel}_1$) if confined in thin film, where all the material of the minor block is spent to form wetting layers at the interfaces.

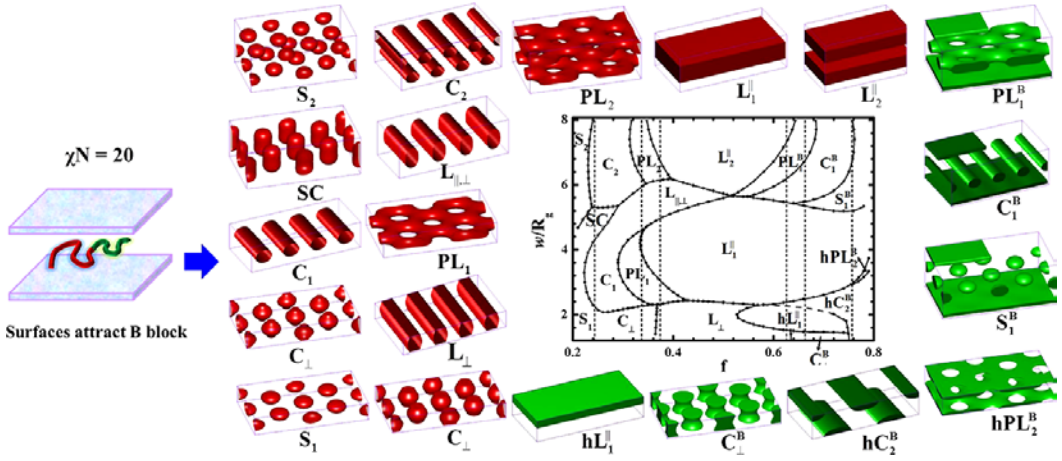

Fig. 1.2.2. Phase Diagram of diblock copolymers confined in thin films between two equivalent interfaces [31].

One more dimension in the phase diagram is opened by the changing difference of the polymer-interface interaction. A theoretical simulation of cylinder-forming diblock copolymer A-B 8/25 between two equivalent interfaces was conducted and compared with experimental results [32]. The model was built for polystyrene-block-poly(hexyl methacrylate) with 33 nm microdomain lattice spacing confined in 33 nm and 40 nm thick films. Upper and lower boundaries are equivalent, and have different interaction energies with beads of blocks A and B: $\varepsilon_{S,A}$ and $\varepsilon_{S,B}$. The parameter $\Delta\varepsilon_S=\varepsilon\varepsilon_{S,A}$ $-\varepsilon\varepsilon_{S,B}$ characterizes the difference in blocks interactions with the interfaces. If$\varepsilon\Delta\varepsilon_S = 0$, interaction energies are the same and no block have preference in wetting the interface. These conditions are called neutral. Interestingly, for $\Delta\varepsilon_S=0$ and film thickness equal to microdomain lattice spacing disordered phase is formed. A slight increase in $\Delta\varepsilon_S$ will lead to formation of well-ordered HEX array of cylinders, oriented perpendicular to the substrate ($C_\perp$). With further increase of$\varepsilon\Delta\varepsilon_S$ cylinders change their orientation to parallel with respect to the substrate ($C_\parallel$). For even larger values of the$\Delta\Delta\varepsilon_S$ perforated lamellae (PL) is formed. A similar phase diagram is obtained for thicker film.

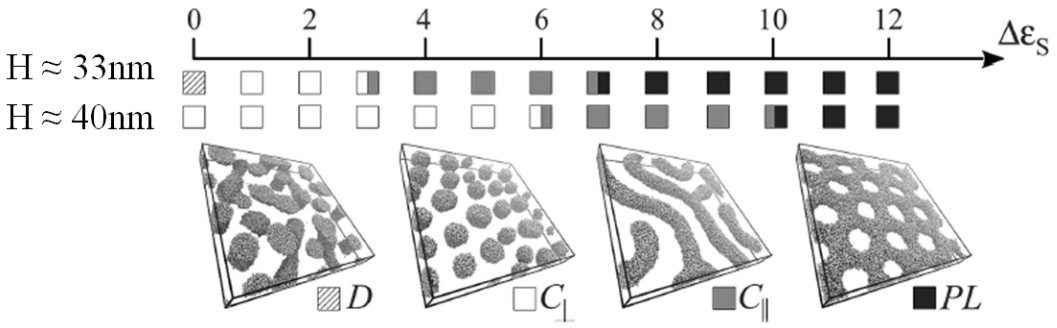

Fig.1.2.3. Modelling of equilibrium morphologies in thin films for cylinder-forming block copolymer depending on difference in blocks interactions with the interfaces.

Between non-equivalent interfaces, driving forces from each interface can form different morphologies at the top and at the bottom fringe, resulting in “hybrid morphologies” with transition zone in the middle of the film [33]. In real polymer films interfaces are rarely equivalent, typically one of the interfaces (bottom) is substrate (commonly silicon wafer), and the second (top) contacts air, top surface is free and affected by fluctuations. For example in [34], for lamellar polymer confined in supported thin films, 4 morphologies were found theoretically: full surface-parallel lamellar morphology (FL), half lamellar (HL), perpendicular lamellar ($L_\perp$) and hybrid structure (HY), which is impossible between equivalent interfaces (fig. 1.2.4). Theoretical results are in good agreement with experimental data for poly(styrene)-block-poly(lauryl methacrylate) (PS-*b*-PLMA).

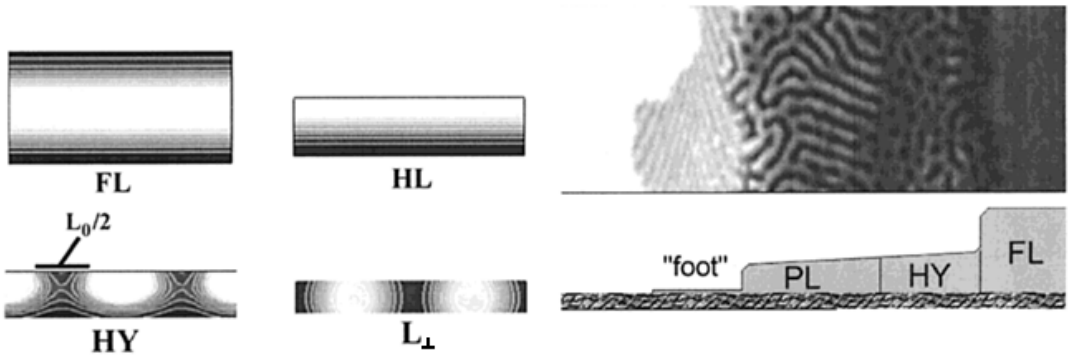

Fig.1.2.4. Example of calculated morphologies in supported thin film (left) and AFM data of PS-*b*-PLMA film with varying thickness (right). L_0 is the lamellae bulk period. FL is full lamellar morphology, HL is half lamellar, $L_\perp$ is lamellae oriented perpendicular to the substrate, HY is hybrid structure [34].

We can conclude that the morphology of BCP is mainly controlled by the following parameters:

1) Molecular mass and composition of BCP, interaction between blocks. These are determined by the choice of BCP,
2) Film thickness;
3) Energies of interaction of each block with top and bottom interfaces.

Preparation of thin films by microtomy of macroscopic BCP monoliths disables the effect of parameters (2-3), which is the basic advantage of the *ex-situ* fabrication of lithography mask.

1.3. Block-copolymer lithography

The idea to use thin films of self-organized BCPs as masks for lithography was introduced by *Mansky et al*. [35, 36], and shortly after the first pattern transfer from BCP films was demonstrated by Park et al. [37]. In this work BCP polybutadiene-*block*-polystyrene (PB-b-PS) having spherical morphology in the bulk, conformed in S_1^B (spheres between two wetting layers on interfaces) was used for creation of dense hole arrays.
Currently self-organizing properties of BCPs are widely used in lithography. $C_\perp$ and $L_\perp$ morphologies are the most attractive structures for lithography. Nanoscale domains are oriented perpendicular relative to the substrate resulting in high aspect ratio lithography masks. Commonly dry etching is not perfectly selective and high aspect ratio masks are preferred for transfer of patterns of high aspect ratio holes/channels in the substrate [38, 39]. Spheres or cylinders parallel to the substrate also provide etching contrast, but have numerous disadvantages: low aspect ratio due to film thickness limitation to single layer, multiple etching steps with different chemistry are required to etch through different blocks, variations of depth of sphere placement, leading to different sizes of holes. Obviously some BCP thin film morphologies are unsuitable for lithography. For example, lamellae oriented parallel to the substrate $L_\parallel$, produce no etching contrast. Optimization of fabrication parameters to make all polymer in the film form $L_\perp$ / $C_\perp$ and prevent formation of $L_\parallel$/ $C_\parallel$is a challenging task for BCP lithography.

Block copolymer lithography begins with the choice of the BCP. Blocks must have large etching contrast and high Flory-Huggins parameter in order to allow fabrication of smaller structures with lower edge roughness. The block used as mask should have high etch resistance.

Before the introduction of poly(styrene)-block-polydimethylsiloxane (PS-b-PDMS) [40], various PS-containing organic block copolymers were used where PS served as a mask. However, glass transition temperature of PS is 100 °C, and it has relatively low etch resistance, making it a poor lithography mask. PDMS provides larger etching contrast between the blocks, high Flory-Huggins interaction parameter and higher etch resistance. The Flory-Huggins parameter of PS-b-PDMS at room temperature is ~ 0.26 [41], which is considerably larger than that of the popular PS-b-PMMA (χ ~ 0.06) [42].

The substrate, usually a silicon wafer, is prepared to be absolutely clean and uniform, often involving cleaning with piranha solution (a mixture of sulfuric acid and hydrogen peroxide) or oxygen plasma and/or repeated rinsing with organic solvents [43]. Chemical and topographical substrate uniformity is important for homogeneity of the polymer film. Creation of structures perpendicular to the substrate requires fine tuning of the polymer-surface interaction. The way to tune interaction energy is chemical modification of the substrate by grafting of a brush layer of well-controlled composition that provides a neutral surface [44].

Then thin polymer films, with thickness in the rage of 10-300 nm, are fabricated by spin-coating [45]; BCP solution is dropped on the rotating substrate. The solution is spread as a thin film by the centrifugal force and the solvent evaporates rapidly, leaving a uniform BCP film on the wafer.

Rapid solvent evaporation during spin-coating process traps the polymer in poorly ordered non-equilibrium state. Since the mobility of the BCP in the thin film is suppressed, relaxation to the equilibrium structure can be extremely slow. To improve order in the film various annealing procedures have been invented. Thermal and solvent annealing or their combinations are the most common annealing procedures. Thermal annealing consists in heating of the BCP film above the glass-transition temperature *Tg* or melting temperature for highly crystalline polymers to overcome the energetic barrier for chain motion. At the same time thermal annealing affects interaction energy of the blocks with the top interface. By varying the annealing temperature the top interface can also become neutral as in the case of PS-b-PMMA [46]. In 2000, Krausch et al. proposed controlled swelling of BCP films in solvent vapor to promote self-assembly [47]. During solvent annealing the BCP film is placed in a closed container in the presence of solvent vapor (or mixture of solvent vapors) and solvent molecules diffuse into the BCP film, increasing the free volume between polymer chains and plasticizing

the polymer. *Tg* is decreased and chain mobility is improved, allowing a decrease of annealing temperature. Parameters of annealing to vary include solvent type [48], time [49] and evaporation mode [47]. The annealing procedure is optimized to prevent formation of mesoscale morphologies [50, 51]. Alternative ways to promote ordering of the BCP films comprise interaction with electric field [52], laser [53], microwaves [54], shear [55], or by soft moulding [56].

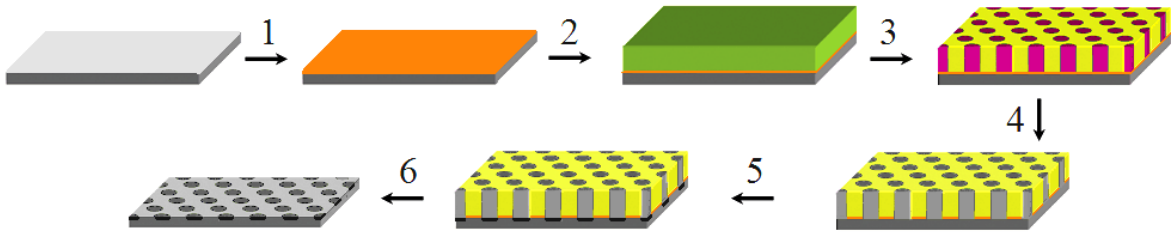

Fig. 1.3.1. Illustration of the typical process of conventional BCP lithography: (1) random brush grafting; (2) spin-coating of the BCP film; (3) thermo/solvo annealing; (4) etching of the mask; (5) etching of the underlying substrate; (6) mask removal. Image from ref. [60] was used.

During annealing phase-separated regions nucleate at random places [57] forming multi-grain structures with short-range order. For $L_{\perp}$ or C_1 (fig. 1.2.2.) multi-grain structure looks like "finger print" pattern with gradually bending lines. In order to achieve long-range in-plane order in BCP films, directed self-assembly (DSA) by graphoepitaxy [58] and chemoepitaxy [59] were developed. Graphoepitaxy is a method to direct the BCP structure by surface topography. Creation of guiding patterns can be performed by electron beam lithography [60], deep ultraviolet projection photolithography (DUV) [61], extreme ultraviolet lithography EUV [62] or conventional optical lithography [63]. Additional steps of resist spinning and disposal (frequently used resists are hydrogen silsesquioxane (HSQ) for e-beam and PMMA or other photoresists for UV lithography) are required. In relation to these types of substrate pre-patterning, the work flow for fabrication of wafer-scale pattern of parallel lines is illustrated in fig. 1.3.2. Firstly parallel channels with larger period than the period of BCP are created on the substrate by conventional photolithography. The pre-patterned substrate is then spin-coated with the BCP film. Pattern of parallel lines is obtained in the channels after annealing. The width of the channels is usually several BCP periods. At this stage the process can be finalized

by pattern transfer to the substrate, if patterning in the limited channel areas is enough for a given application. The described process is called graphoepitaxy. If patterning of the whole wafer is required, a chemical pattern will be transferred to the substrate inside the channels. Mild oxygen treatment creates a chemical nanopattern consisting of polar (bare substrate or oxygenated brush) and neutral (unetched brush) stripes. Then all topographical guiding structures and residual polymer are removed and the flat chemically patterned substrate is spin-coated with the same BCP. The chemical pattern will guide BCP orientation and the whole wafer will be covered with lines of parallel standing lamellae. This type of directed self-assembly is called chemoepitaxy. Finally the pattern is transferred to the substrate by reactive ion etching.

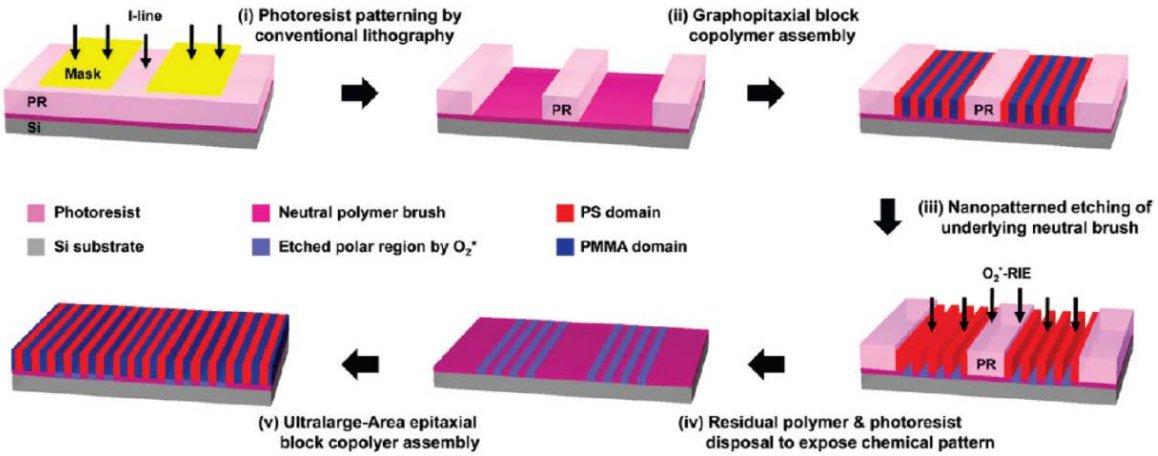

Fig. 1.3.2. Schematic workflow for chemoepitaxy [59]. (i) Guiding pattern is made by conventional lithography. (ii) BCP is spun on top of the patterned substrate. (iii) BCP pattern transferred to the underlying brush. (iv) polymer and photoresist are disposed. (v) Chemically patterned substrate spin-coated with BCP.

Pre-patterning of a substrate with parallel tranches can be utilized for guiding both lamellae and cylinders along the tranche walls [64]. By anchoring neutral brush also on the walls of the graphoepitaxy pattern, standing cylinders in parallel channels can be obtained [65]. HEX pre-patterning can be used to realize wafer-scale nanomesh with crystalline order and with period half of the period created by e-beam lithography [60], fig. 1.3.3. Pre-patterning creates dots preferentially wetting the minor block of BCP, non-patterned areas are slightly preferential for the major block. Spinning of BCP on such a substrate will guide cylinders to assemble in $C_{\perp}$ with crystalline order.

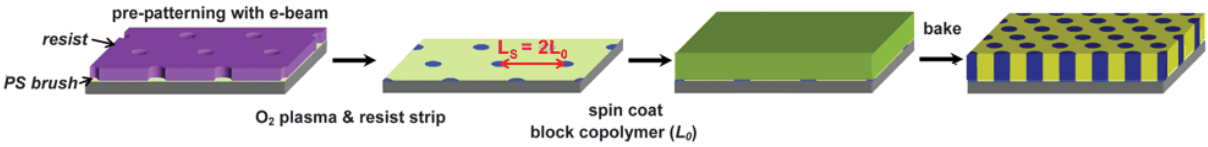

Fig. 1.3.3. Schematics workflow for density multiplication by means of chemoepitaxy [60]. Resist is pre-patterned with e-beam; Oxygen plasma is used to create chemical HEX pattern on the substrate; spin-coating with BCP with half period; annealing.

1.4. Graphene nanostructuring

Although DSA allows to exploit of the whole potential of the BCP for patterning, its application for graphene nanostructuring is problematic. Putting various resists in contact with graphene changes graphene properties (charge carrier mobility, doping) [66] and resists are very difficult to remove completely [67]. On the other hand the patterns realized without graphoepitaxy are not perfect.

First graphene nanopatterning by means of BCP lithography was made with the help of C⊥ PS-b-PMMA [68, 69]. Large areas of graphene were patterned with polycrystalline nanomesh. Graphene nanomesh with 35 nm center-to-center distance and 18 nm constriction was demonstrated in [68]. An effective energy gap of ~100 meV and on/off current ratio of ~40 at room temperature were reported. *Bai et al*. [69] have fabricated graphene manomeshes with 39 nm periodicity having neck widths of 15 nm, 10 nm, 7 nm, and with 27 nm periodicity having neck width of 9 nm, by using block copolymers with two different molecular masses and controlled overetching. An on/off current ratio exceeding 100 was measured for the device with 7 nm neck width. Unfortunately, graphene nanomeshes fabricated with PS-b-PMMMA have only a few micron domain sizes.

By using PS-b-PDMS block copolymers with larger Flory-Huggins interaction parameter and by tuning the annealing conditions, small domains can coalesce into larger domains with sizes of tens of microns with almost unidirectional orientation [70]. Lines in domain are almost unidirectional with few imperfections like dislocations and line misorientation. Possibility to lift the mask from the silicon wafer and transfer it to any other substrate allowed to fabricate dense arrays of graphene nanoribbons with 12 nm width and 35 nm period without graphoepitaxy [70].

A quasi-periodic nanomesh with ~33 nm center-to-center distance was fabricated by nanoimprint lithography [71]. Nanomeshes with neck sizes of 17, 14, 10 and 7 nm were obtained by controlled overetching. A maximum bandgap value of ~140 meV extracted from the on/off current ratio for the nanomesh with 7 nm neck width was reported. A disadvantage of the method is a notable variation in hole sizes caused by non-uniform thickness of residual level of nanoimprint resist.

Graphoepitaxy can be applied to get crystalline order, but topographic features of graphoepitaxy use valuable substrate area. Perfectly parallel graphene nanoribbons were obtained in very narrow channels [72] by using PS-b-PMMA. For channels broader than 375 nm, parallel alignment stopped working. For PS-b-PDMS [73], channel width suitable for parallel arrangement can be enlarged up to 2 μm. *Son et al*. reported fabrication of 12 nm and 9 nm wide graphene nanoribbon arrays with successfully opened bandgaps of 58 meV and 78 meV at 100 K, respectively.

E-beam writing develops parallel to BCP, but it also requires coating with resists. As an advantage it can give customized pattern, but resolution is still lower than for BCP lithography: in recent work the smallest feature sixe realized by e-beam lithography and controlled overetching in oxygen plasma was 20 nm [74].

Alternatively maskless lithography can be used for graphene nanostructuring. These methods can utilize high-energy electrons from transmission electron microscope [75] and give sub-5 nm features [76].15 nm and 7 nm feature sizes were produced by helium and neon ion beam microscopes, respectively [77, 78], while electrochemical etching with scanning probe lithography give resolution few nanometers [79, 80]. The main disadvantages of these methods are low throughput, relatively high costs and difficulties to scale-up.

1.5. Summary

Graphene nanopatterning is required for both industrial applications and scientific studies. One of the promising ways to fabricate nanopatterned graphene is to utilize self-assembling properties of block copolymers. Block copolymer morphology in a bulk is well-understood and in case of lamellae and hexagonal BCP can be easily aligned by shear. In thin films many parameters affect the block copolymer morphology and it can be challenging to get the necessary orientation of microdomains. In lithography BCP thin film are used for hexagonal nanomesh fabrication (spheres, cylinders perpendicular to the substrate) or arrays of

nanoribbons (cylinders parallel to the substrate, lamellae perpendicular to the substrate). Disorder plays a significant role in graphene electrical transport properties making it important to fabricate highly ordered nanostructures on graphene.

2. Characterization techniques

Imaging of nanomaterials is an essential part of nanoscience and nanotechnology. Human eye cannot be used to see objects and details at nanolevel. Precise measurements of film thickness (50 nm-100 nm) and investigation of structures with 10 nm feature sizes requires sophisticated up-to-date equipment. Theoretical foundation and main working principles of complex equipment relevant for the work will be discussed in this chapter.

2.1. Optical microscopy

Optical microscopes use visible light (electromagnetic waves with wavelengths between 400 and 700 nm) to get magnified images of small samples. Optical microscopes are generally used to observe micro- to millimeter scale objects. Due to diffraction of visible light, objects are distinguishable only if they are separated by more than 200 nm.

For optical imaging Nikon ECLIPSE L200 with up to 50x magnification lenses was used. The fact that the thickness of polymer films directly correlates with their color makes optical microscope a fast way to check film thickness. The effective refractive index of our nanoporous polymer calculated by from Lorentz-Lorenz relation is 1.3 [81]. If a polymer film covers the silicon wafer with only 1-2 nm thick silicon oxide layer, the color of the film is determined by the optical path difference (OPD) between light reflected from the top of the film and light reflected from the silicon. OPD can be calculated as follows:

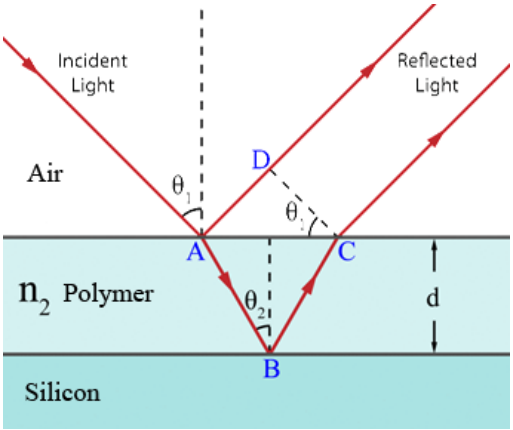

Fig. 2.1.1. Scheme of light reflection.

$$OPD = n_2AB + n_2BC - n_{air}AD, \quad (1)$$

where n_2 – refractive index of the polymer film, n_{air} is refractive index of air.

$$OPD = \frac{2n_2 d}{cos\theta_2} - n_{air} AC sin\theta_1 = \frac{2n_2 d}{cos\theta_2} - n_{air} \frac{2dsin\theta_2}{cos\theta_2} sin\theta_1 \text{ (2)}$$

According to Snell's refraction law (3)

$$n_{air} sin\theta_1 = n_2 sin\theta_2 \text{ (3)}$$

(2) can be rewritten as:

$$OPD = 2dn_2 \left(\frac{1}{cos\theta_2} - \frac{sin\theta_2}{sin\theta_1}\frac{sin\theta_2}{cos\theta_2} sin\theta_1\right) = 2dn_2 \left(\frac{1}{cos\theta_2} - \frac{sin^2\theta_2}{cos\theta_2}\right) = 2dn_2 \left(\frac{cos^2\theta_2}{cos\theta_2}\right) = 2dn_2 cos\theta_2 \text{ (4)}$$

$$OPD = 2n_2 d cos\theta_2 \text{ (5)}$$

In case of several layers, for example, if we have thick silicon oxide layer under the polymer film, we need to sum contributions from all layers:

$OPD = 2\sum_i n_i d_i cos\theta_i$, (6)

where n_i, θ_i are taken for each layer.

Assuming normal incidence of light in the optical microscope and a uniform refractive index $n(\lambda)$, (6) can be rewritten for all wavelengths:

$OPD = 2\ \sum_i n_i d_i$ (7)

The color of a thin film is usually determined by the wavelength that fulfills conditions for constructive interference at the given film thickness, i.e. when OPD equals a full number of wavelengths. In case of ultra-thin films, when OPD is below interference maxima for all wavelengths of the visible light, the color is determined by destructive interference. With increase of the film thickness from 0 nm (white light reflected) the phase shift increases faster for shorter waves. Polymer films thicker than ~20 nm start to exhibit light brown color due to suppression of blue light [82]. Our region of interest is 30-60 nm thick films and they have light brown or beige color.

2.2. Atomic Force Microscopy

For precise topography measurements an atomic force microscope (AFM) was used. In AFM [83] the sample is scanned with a sharp needle (tip radius less than 10 nm), connected to the end of a cantilever. Nanometer-precise movements of the sample are performed by a

piezoelectric scanner. The force originating from the tip-sample interaction bends the cantilever and these deformations can be detected by an optical lever detection system. A laser beam is shined at the end of the cantilever, reflected and directed to the center of a position-sensitive photodiode. When the cantilever bends, the laser spot moves on the photodiode and the signal on the sections of the photodiode changes. In this way deformation can be measured, and a feedback loop moves probe (or sample) up or down to keep a particular operating parameter constant.

AFM is ideal for measuring surface roughness and heights of small topographical features.

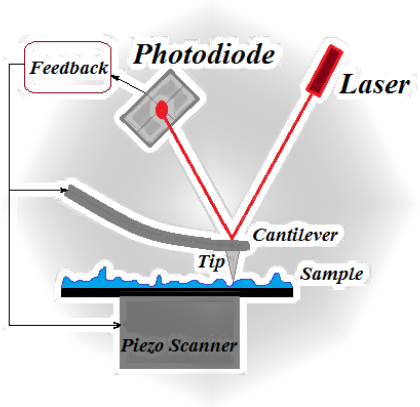

Fig.2.2.1. Schematic AFM working principle.

In the tapping mode the cantilever oscillates at a frequency close to the resonance with an amplitude of 100-200 nm. When probe approaches the surface, it is firstly attracted by Van der Waals force. This force shifts the resonance frequency and the amplitude of oscillations changes. By measuring this weak attraction a true non-contact mode can be realized. When the oscillating probe comes closer to the surface, it intermittently contacts the surface and the oscillation magnitude reduces due to energy dissipation. This mode is called intermitted or tapping. The feedback loop moves the sample up and down in order to keep the amplitude of oscillation constant.

2.3. Scanning electron microscopy

Scanning electron microscopy (SEM) analyses local interaction of an electron beam with the sample. A small spot on the sample, irradiated with electrons, becomes the source of numerous signals: secondary electrons (SE) are produced in the interaction volume, back-scattered electrons (BSE) and characteristic X-rays [84] are also generated. BSE show contrast between different atoms: heavier nuclei produce more BSE. In the project in-lens SE detector is used.

Most of SEM images are obtained using a SEM-ZEISS instrument with field emission gun. It has two secondary electron detectors: Inlens and SE2, differing in their location [85] (fig. 2.3.1 a). The in-lens detector is located inside the column and can collect more low-energy electrons. When sample is very close to the lower objective and immersed in the field of the objective lens, SEs spiral upward in the magnetic field of the objective and can be efficiently collected by the in-lens detector. The in-lens detector is good for high-resolution topographic imaging at working distances of 4 mm-10 mm. The SE2 is located inside the chamber aside from the beam path. Its collector attracts both SEs and BSEs. The SE2 detector is useful for general purpose imaging at working distances of up to 30 mm.

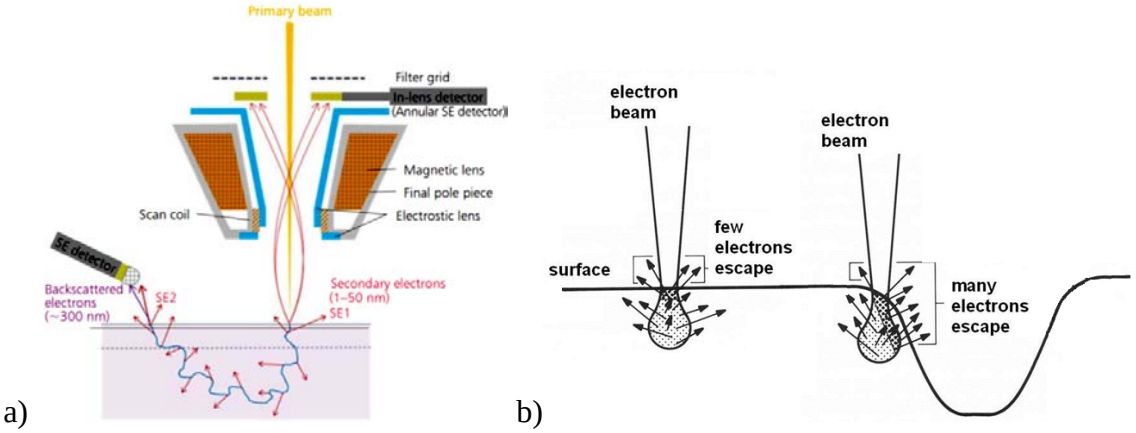

Fig. 2.3.1 a) SE2 and in-lens detector location in SEM chamber [85]. b) Schematics of SEM working principle [86].

Secondary electrons provide information on sample topography and morphology. The contrast appears due to edge bloom effect (see scheme in fig.2.3.1.b): close to edge and at the slopes more SE can escape from the sample leading to increased SE signal and image brightness.

During scanning, electrons can accumulate on the surface of the specimen. “Charging” leads to changes of the contrast in scanned areas. To prevent charging the sample can be coated with a conductive metal film (gold, platinum). The presence of pattern can be determined much faster by SEM than by AFM. Images of nanoporous polymer masks prepared in this work were of a good quality without sputter coating. For high quality SEM imaging of graphene nanomesh graphene flakes were transferred onto gold electrical contacts to allow proper grounding.

2.4. Raman microspectroscopy

Raman spectroscopy is a commonly used method to characterize graphene's quality and properties. Raman spectroscopy studies inelastic scattering of monochromatic light on the sample. Photons interact with excitations in the system (phonons, molecular vibrations, etc.) resulting in energy loss (this type of scattering is called Stokes Raman scattering) or energy gain (anti-Stokes Raman scattering). The electromagnetic radiation from the illuminated sample is collected. Inelastic scattering spectrum is very sensitive to the geometric structure and bonding within molecules. This technique is non-destructive and non-invasive if measurement conditions are chosen appropriately. In graphene, Raman spectroscopy can provide evidence on doping, edges, strain and stress, disorder, chemical functionalization, electrical mobility, thermal conductivity, electron–phonon and electron–electron interactions, magnetic field and interlayer coupling [87].

The most important for the current project is determination of the presence of nanopatterned graphene, which can be distinguished from unpatterned graphene by Raman microscopy (fig. 2.4.1. a). Graphene spectrum has several strong peaks [88], providing the following data on graphene.

• G peak (~1585 cm^{-1}). The G band corresponds to the C-C bond in-plane vibrational mode of sp^2 hybridized carbon atoms (fig. 2.4.1.b) and is found in all sp^2 carbon materials. The position and intensity of the G band are sensitive to the number of graphene layers in the sample. As the number of layers increases, the G peak intensity increases linearly and the peak shifts towards lower wavenumbers (fig. 2.4.1.b). The linewidth of G peak (~10-15 cm^{-1}) is sensitive to strain, temperature and doping. Temperature and doping also shift the position of the G peak.

• D peak (~1250-1400 cm^{-1}). The D band (also called "disorder" or "defect" band) represents a ring breathing mode from sp^2 carbon rings fig 2.4.1.d. However, the ring must be adjacent to graphene edge or defect in order for the D band to be active. Thus the intensity of the D band in some cases is directly proportional to the level of defects in the sample (fig. 2.4.1.a). In graphite and high-quality graphene it is vanishing.

• G' or 2D peak (~2500-2800 cm^{-1}) is the second order of D band, activated by a two phonon lattice vibration. Unlike the D band, proximity of a defect is not required for its activation. Single-layer graphene exhibits a single symmetric Lorenzian peak, but with increasing number of layers it splits into several overlapping modes (fig. 2.4.1.c). The intensity ratio of I_{2D}/I_G is a

common parameter for graphene characterization. For single layer high-quality graphene it is 2 or higher, with zero D peak.

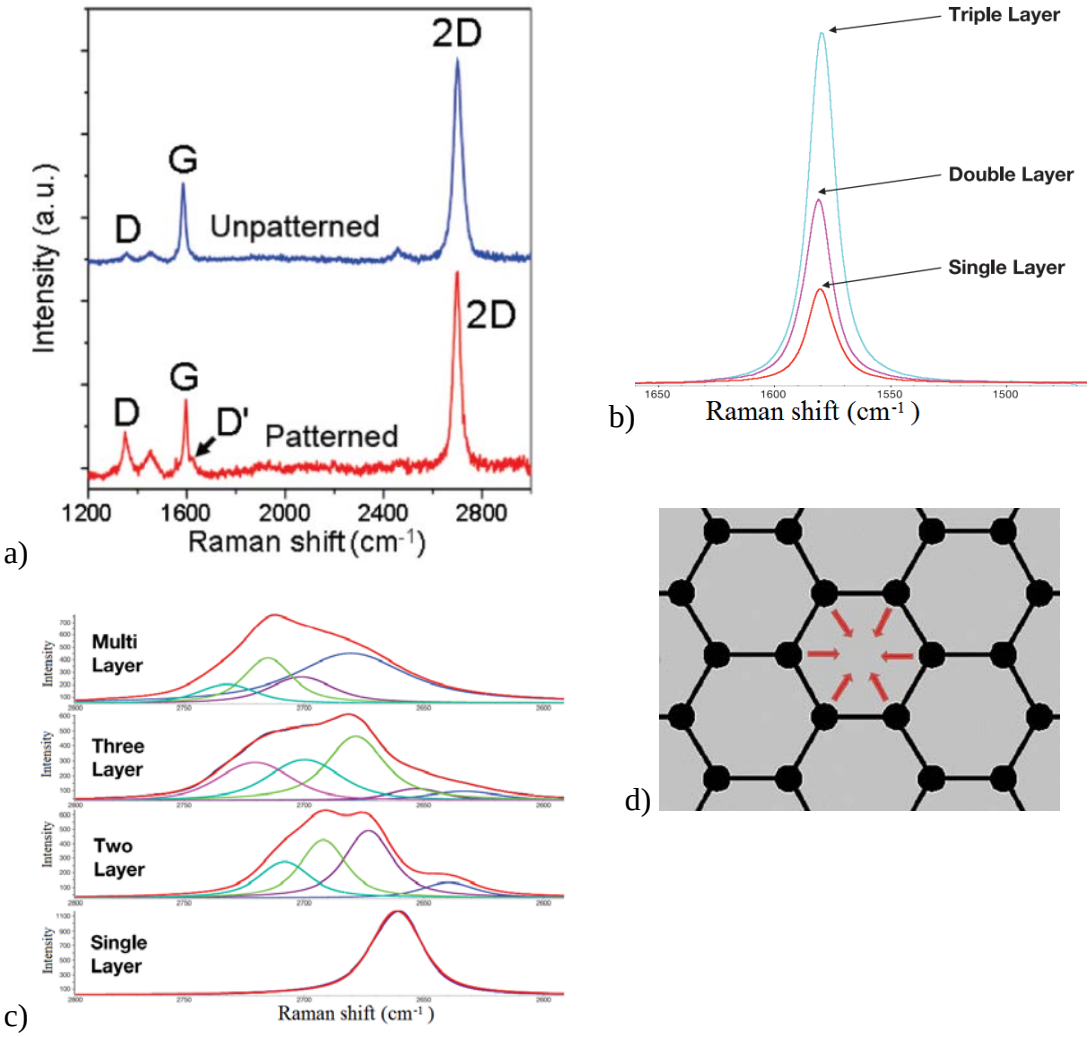

Fig. 2.4.1. a) Examples of Raman spectra on graphene. a) Raman spectra of unpatterned graphene and graphene nanomesh [89]. b) G-peak for single, double and triple graphene layer [90]; c) 2D peak for single, double, triple and multiple graphene layers [89]; d) schematics of breathing mode from sp^2 carbon rings.

3. Fabrication techniques

Approaches for nanomaterial fabrication can be divided into two groups: top-down and bottom-up. Top-down approaches concern the shaping and structuring of larger pieces by controlled removal of material, typically by means of a radiation beam (electromagnetic, electrons, ions, etc.). In bottom-up approaches smaller parts are made to assemble into larger parts, which could be molecular or atomic dimension precursors self-assembling into finely structured samples. Fabrication of nanometer-scale structures requires precise control of fabrication conditions and environment (absence of dust, contaminations, etc.), so most fabrication equipment is placed in a clean room.

3.1. Conventional mask fabrication by spin-coating

Block-copolymer lithography for graphene bandgap engineering was firstly introduced in 2010. Two articles on graphene nanomesh fabrication [68, 69] with the help of HEX poly(styrene)-block-poly(methyl methacrylate) (PS-b-PMMA) appeared nearly simultaneously.

The work flows applied in the two articles are very similar. Because graphene is not a neutral surface for PS-b-PMMA, grafting random brush PS-r-PMMA was required in order to orient cylinders perpendicular to the substrate. For this purpose graphene was covered with a thin layer of evaporated silicon oxide, since anchoring of the brush utilizes hydroxyl groups from the silicon surface. Then a multi-step etching process was performed in order to get graphene nanomesh (fig. 3.1.1).

The key step of the procedure is the creation of BCP mask with cylinders orientated perpendicular relative to the substrate. Both articles [68, 69] give precise recipes of optimized conditions. Because there was a need for nanostructured graphene in CNG, we have chosen to reproduce results of J. Bai et al. [69]. They purchased all the polymers and their procedure seemed to be more general, since they succeeded to realize perpendicular PMMA cylinder orientation for two different BCPs with periods of HEX structure of 39 and 27 nm. The hope to reproduce the results was very strong. Before repeating the whole procedure on graphene, it is important to reproduce “standing” orientation of cylinders on the silicon substrate.

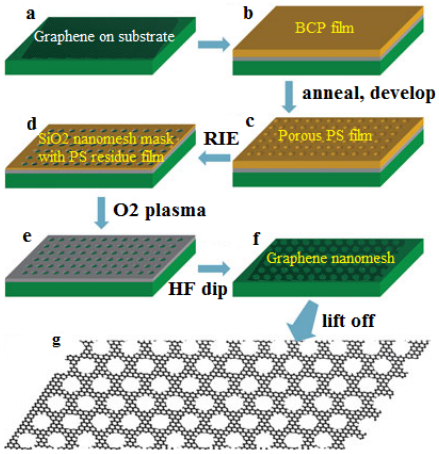

1) Pristine graphene on substrate covered with SiO_x by vapor deposition, random brush grafted and spin-coated with PS-b-PMMA;
2) Annealing and development of PMMA, leaving nanoporous PS mask;
3) Fluorine-based etch to penetrate silicon oxide layer and form silicon oxide hard mask;
4) Graphene etch with oxygen plasma;
5) Removal of the oxide mask;
6) Etch of the underlying silicon substrate to lift off graphene.

Fig. 3.1.1. Workflow for graphene nanopatterning from [69].

The aim was to reproduce the reported results as closely as possible. All polymers used in the article [69] were purchased from the Polymer-Source, Inc. Unfortunately, the small period block-copolymer giving 27 nm period and the random copolymer used in [69] were not available at Polymer-Source, Inc. That was the reason to use the PS-b-PMMA with the larger period and two different random copolymers as brushes. One of the random copolymers was purchased from Polymer-Source, Inc. and had the same composition, but higher molecular weight (14500 g/mol instead of 11000 g/mol used in [69]). Samples with this type of random brush will be labeled as PrCP. The second random copolymer was synthesized in our laboratory (LrCP). It has additional hydroxyl groups on 2-hydroxy ethyl methacrylate (HEMA) chain units to anchor to the silicon oxide.

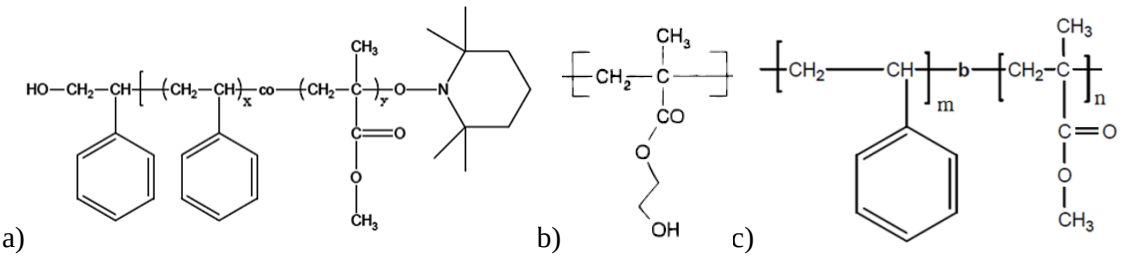

Fig. 3.1.2. Structures of used chemicals. a) Random copolymer PS-b-PMMA from Polymer-Source, Inc.; b) 2-hydroxy ethyl methacrylate (HEMA) – additional chain units in random copolymer synthesized in our laboratory; c) Block copolymer PS-b-PMMA.

In detail the utilized chemicals have following specifications (Fig. 3.1.2). From the PolymerSource was purchased random copolymer poly(styrene-co-methylmethacrylate), -hydroxyl- -tempo moiety terminated with M_n=14500 g/mol, 55mol% Styrene. Our random copolymer PS-r-PMMA-r-HEMA has weight composition HEMA = 2w%, PS= 55w%, PMMA 43w%, and M_n=16300 g/mol, PDI=1,466. The same PS-b-PMMA as in ref. [69] was purchased from polymer source, it has M_n=77000 g/mol, PDI =1,09, with weight composition PS:PMMA 55:22.

The full procedure for vertical alignment of microphases in the thin film supported by silicon substrate is as illustrated in fig. 3.1.3. The whole process took place in the clean room. At first, clean silicon wafer with a thin natural oxide layer (1-2nm) was spin-coated with 1w% solution of the random copolymer in toluene. A ~30 nm thick brown polymer film was obtained. Then the sample was put into the oven for anchoring of the polymer with hydroxyl groups to silicon oxide. Air was pumped out and the oven was heated up linearly from room temperature to 170° in 20 minutes. The sample was kept for 72 hours at 170°C in vacuum, then the oven was cooled to room temperature under nitrogen flow in 30 minutes. Afterwards the wafer was rinsed in toluene to remove unanchored polymer. Most of the film was removed and only a very thin transparent layer of random copolymer brush remained: it had thickness of 2-4 nm for LrCP and of 4-7 nm for PrCP. Wafers with the random copolymer brush were spin-coated with a solution of PS-b-PMMA in toluene. Resulting BCP films were thermally annealed at 180-225°C for 12 hours under vacuum. Annealing was expected to orient all cylinders perpendicular to the substrate, but we always observed that varying fractions of the cylinders are misaligned. PMMA in the annealed film was degraded by ultra-violet (UV) light in air. A 350 W mercury UV lamp with i-line filter (365 nm wavelength) was used for 1 minute. Degraded PMMA was washed away by rinsing in glacial acetic acid followed by intensive water rinsing. Thus nanoporous PS mask was fabricated. Then the samples were studied under SEM.

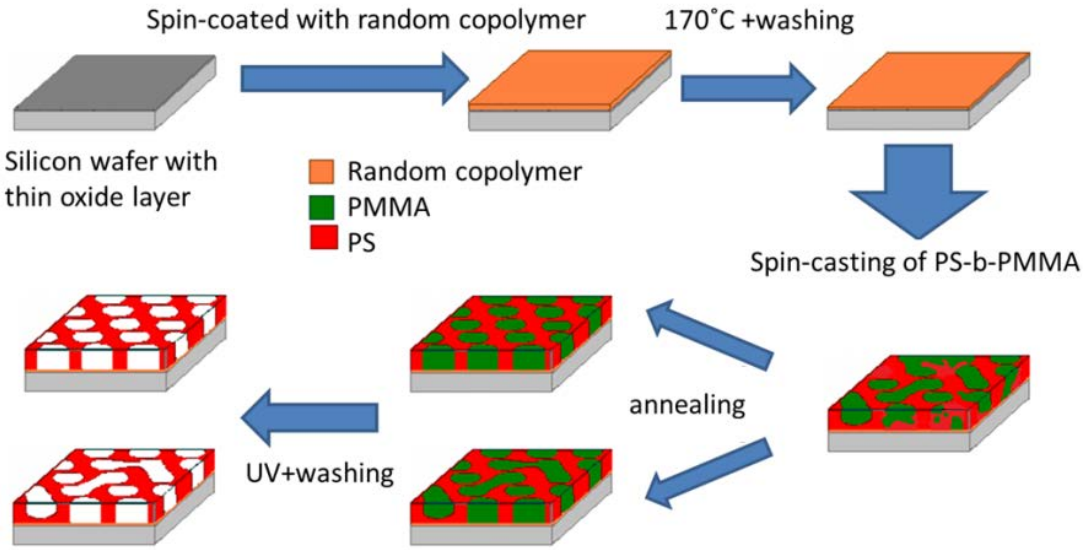

Fig. 3.1.3. Scheme of the process flow for nanoporous PS mask preparation. Steps are the following:

- Spin-coating of the clean silicon wafer with random copolymer (~30 nm thick film);
- Anchoring via hydroxyl groups to silicon oxide at 170° C for 72 hours;
- Toluene wash to remove unanchored random copolymer;
- Wafer with random brush is spin-coated with block copolymer PS-b-PMMA;
- 12 hours thermal annealing; can lead to proper or poor alignment;
- UV-irradiation, glacial acetic acid washing to remove degraded PMMA, water rinsing.
- SEM for nanostructure observation.

3.2. Microtome-based mask fabrication

The work flow of the process (fig. 3.1) indicates three main stages: preparation of aligned polymer monolith (1, 2), mask microtoming and deposition onto the substrate (3) and multi-step reactive ion etching (RIE) for pattern transfer (4, 5).

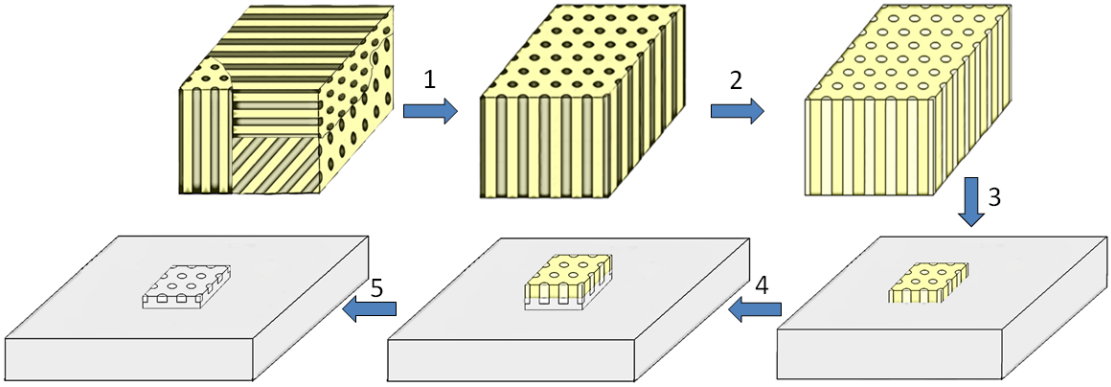

Fig. 3.2.1. Work-flow of the proposed nanolithographic process. (1) 1,2-PB-*b*-PDMS with random domain orientation is shear-aligned and cross-linked to fix the structure. (2) PDMS is selectively etched to obtain nanoporous PB (nPB). (3) nPB is microtomed at room temperature. The sections suspended in a water droplet are captured within a metallic loop and transferred onto a silicon wafer. (4) Silicon etching by RIE, which transfers the pattern to the substrate under the mask and uniformly etches the silicon outside of the mask. (5) Mask removal by oxygen plasma.

Block-copolymers 1,2-polybutadiene-*block*-polydimethylsiloxane (1,2-PB-b-PDMS) synthesized in our lab were used for the preparation of the polymer monolith. A whole library of this polymer was synthesized and characterized in previous work from our group [91]. This BCP is remarkable. The first block consisting of 1,2-PB has vinyl double bounds C=C and can be cross-linked. The PDMS block can be selectively etched from the bulk by wet chemistry, leaving a nanoporous scaffold of cross-linked 1,2-PB. In detail, the procedure for the preparation of nanoporous polymer is as follows. Block copolymer and 1% mole fraction of cross-linker relative to double bonds were co-dissolved in tetrahydrofuran (THF) and cast into a flat-bottom Petri dish; after overnight solvent evaporation under nitrogen flow, the paste-like block copolymer was squeezed between two microscope glasses equipped with 1 mm spacers and shear-aligned mechanically by hand. The glasses were moved back and forth relative to each other with 5 mm amplitude and 0.2 Hz frequency for 15 cycles. It is worth noting, that the polymer in direct contact with the glass plates does not move properly and form a skin layer with poorly aligned polymer domains. The shear-aligned samples were cross-linked for 2 hours at 140°C in nitrogen atmosphere. Afterwards quantitative etching of the PDMS block can be performed by putting the polymer monolith into tetra-*n*-butylammonium fluoride (TBAF) in

THF solution at room temperature for 48 hours. In this way PB-b-PDMS block copolymer and nanoporous 1,2-PB monoliths for HEX, GYR and LAM morphologies can be fabricated.

A microtome is a tool to slice materials into extremely thin sections with high precision of thickness. Microtoming is a common procedure to prepare samples for transmission electron microscopy. A microtome consists of a very sharp knife, made of steel, diamond or glass, and a mechanical motor. Both knife and sample are tightly fixed in their holders. The knife can be translated horizontally with nm-precision, which allows precise controlling of section thickness. Section is cut off during samples movement downwards, as illustrated in fig. 3.2.2. There are two principal modes of sectioning: dry and wet. Knifes for the wet sectioning have a groove filled with water. After cutting the slice floats on the water surface and can be captured by a special loop. During dry slicing, sections stick to the knife and are removed from the sharp edge with an eyelash and then collected.

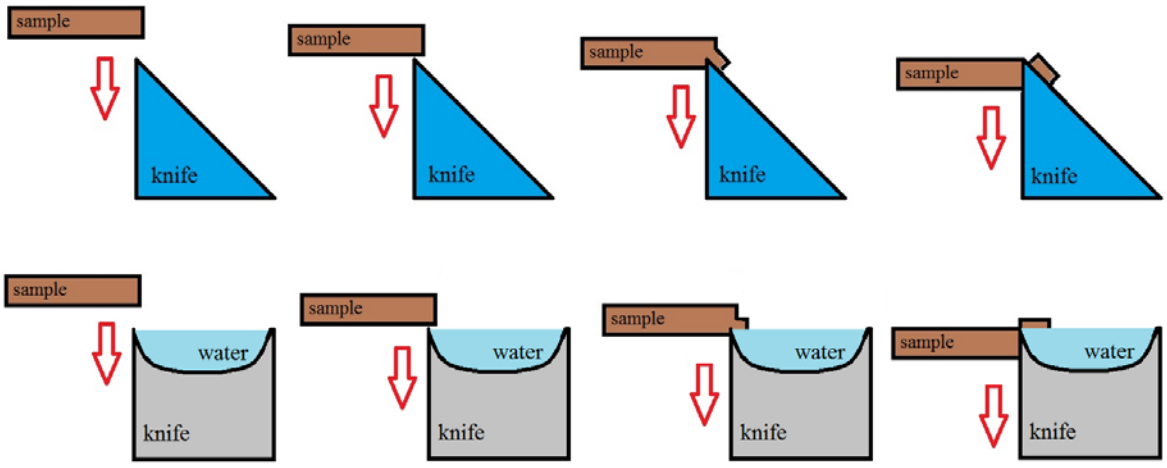

Fig. 3.2.2. Schematics of microtoming process for dry (upper row) and wet slicing.

Compression of soft samples during the cutting process can lead to formation of wavy sections. One of the ways to make the polymer samples harder is to decrease temperature. For this need cryomicrotoming was developed: both sample and knife are placed in the chamber and liquid nitrogen is pumped inside. Temperature can be decreased to -170°C.

Cryomicrotoming and standard wet slicing do not allow sufficient degree of control for the thickness and shape of the sections from polymer monoliths. Thickness could not be kept

constant during wet slicing. Thin sections were tens of microns in size. In cryomicrotoming the thin sections were nearly invisible and too small to manipulate with an eyelash. Before transfer many sections were accumulated at the knife edge. The formed agglomerate was then collected by an eyelash inside a small vial bottle. Several droplets of isopropanol (assay: ≥99.9%) were added, sections were separated by ultra-sonication and then deposited onto the silicon wafer. After solvent evaporation sections stick properly to the wafer and don't detach during further rinsing with water and isopropanol. Wafers with many flakes on top were carefully studied under a high magnification optical microscope. The thinnest flakes (brown) were found and the thicknesses of some of them were measured by AFM. Some examples of thin polymer flakes obtained by cryo microtoming with AFM height profiles are presented in fig. 3.2.3. Because of the lack of control, flakes have irregular shape and very rough surface due to compression during the cutting process. Wave-like thickness variations with ~5 nm amplitude are clearly visible for both BCP (top row) and nPB monoliths slicing. The thinnest sections obtained were 25 nm thick and less than ten microns in sizes. The largest piece was 70 nm thick and 90 μm large.

Most of the flakes were blue (~120 nm thick) and it could happen, that there were no flake thinner than 80 nm on the whole wafer. This illustrates the low degree of predictability on sample thickness achieved by traditional cryo/wet microtomy.

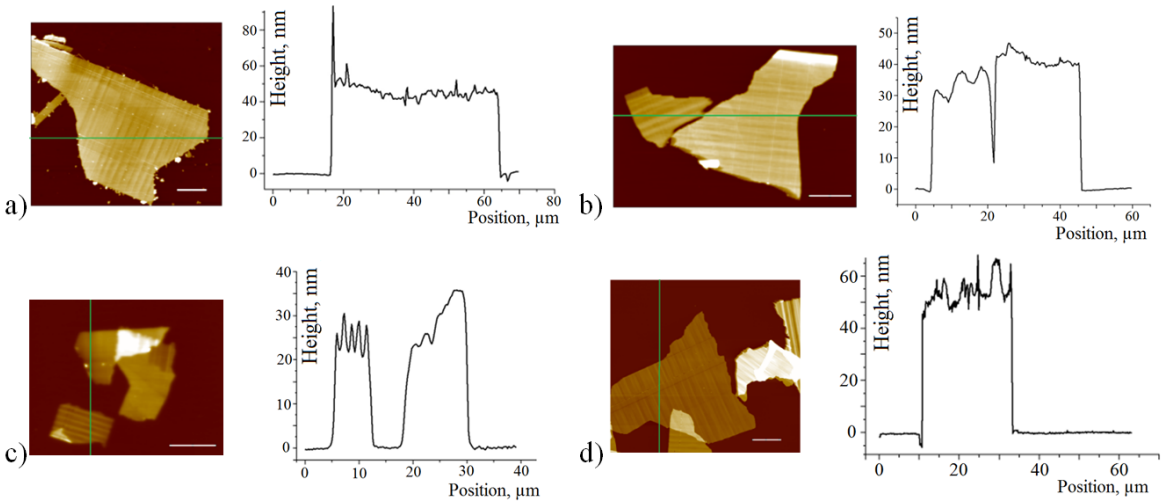

Fig. 3.2.3. AFM images of BCP flakes (a-b) and nPB flakes (c-d) obtained by cryo microtoming. AFM profiles are taken along the green lines. All scale bars are 10 µm.

Microtomed masks can bear numerous imperfections. If knife is damaged, large scratches will appear on the section surface (fig. 3.2.4 a). Smaller scratched (narrow parallel lines ~30 nm wide and 2 nm high) are left by polymer dust particles accumulated on the edge of the knife. The flake in fig. 3.2.4.b is one cut off the poorly aligned skin layer. In the SEM image 8 domains with different orientation are distinguishable on an area of ~200 µm^2.

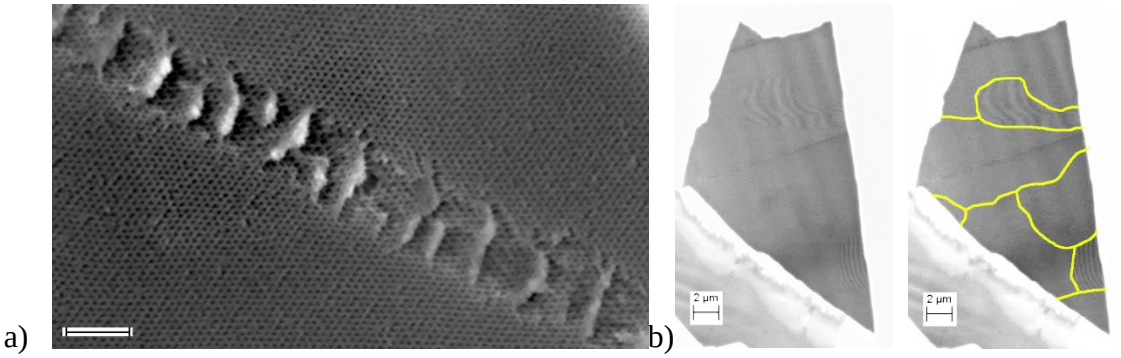

Fig. 3.2.4. SEM images of nanoporous flakes. a) nPB mask with large scratch from the knife; **b**) Small flake cut off the skin layer and the same flake with the highlighted domain borders.

The best choice for obtaining large and smooth flakes is ultra-sonic oscillating knife. It oscillates during the slicing process for minimization of the sample compression [92]. Prior to the cutting of ultra-thin sections sample trimming procedure is highly recommended. Trimming is the standard procedure to shape samples as truncated pyramid. Firstly, front fringe of the sample is trimmed with front facet of the trimming knife, then pyramidal sides are trimmed with the side facets of the knife, as illustrated in fig. 3.2.5. Lots of material is quickly removed by the special trimming knife. It is better to trim with the trimming diamond knife to prevent glass or iron particles appearance in the sample that can damage the precious oscillating diamond knife. In further experiments the misaligned parts at the sample fringes were removed by appropriate trimming with the DiATOME trimtool 45 and sections were only cut from the middle of the monolith. During the trimming procedure all edges of the sample were cut away, and the samples were shaped as truncated pyramids with the rectangular front fringe face of ~200 x 300 μm^2.

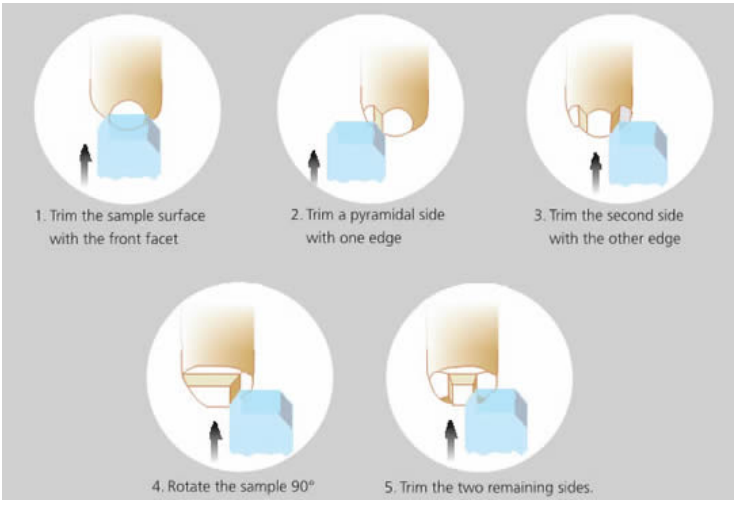

Fig. 3.2.5. Trimming procedure from DiATOME web site [93].

Samples were sectioned at the resonance frequency (~25.9 – 26.3 kHz) at amplitudes 2-6 V, feed 30-60 nm, sectioning speed 0.6 mm/s and at an angle of 6°. Sections floating in the groove of the knife filled with DI water were picked up with a home-made metal loop and deposited

directly onto the clean silicon wafer chip. Water droplet was soaked with a paper napkin. The wafer with the sections was finally rinsed with water and immersed in isopropanol before their processing in the etcher.

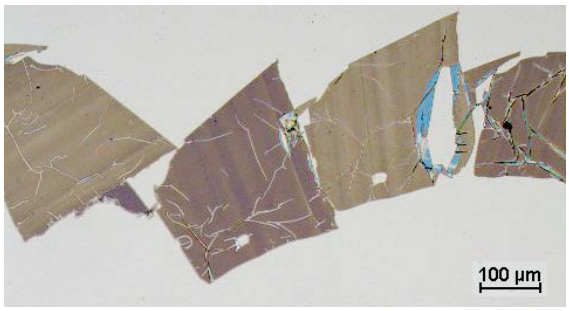

Fig. 3.2.6. Optical image of sections obtained with ultra-sonic knife deposited onto silicon wafer. 100 µm scale bar.

With the ultra-sonic knife series of full section can be cut with minor variation in thickness (fig. 3.2.6.). All flakes have the same shape. Sizes of flakes can be up to 300 µm with typical thicknesses of 50-60 nm. They are easy to find in optical and scanning electron microscopes. Sections became large enough to form wrinkles. The presence of compression can be detected by periodic changing in color saturation. External mechanical vibrations during sectioning also contribute to thickness variations. Because of these factors slicing with thicknesses under 50 nm is not fully controlled. The thinnest sections of nPB obtained by ultra-sonic microtoming were 30 nm thick and had a size of 100 x 300 μm^2.

3.3. Dry etching

For pattern transfer from both spin-cast and microtomed masks two different etchers in Danchip were used: Inductive Coupled Plasma (ICP) Metal Etcher and Reactive Ion Etcher (RIE2). In the plasma etcher material is removed by high-energy ions that attack the surface

and chemically react with it. In order to ensure stability of etcher performance, the chamber was cleaned by applying 20-30 minutes of oxygen plasma before each sample etching.

Several different recipes for silicon etching were used. The recipe for anisotropic silicon etch in RIE2 performs black silicon etch with a SF_6/O_2 mixture [94]. Applied to bare silicon surface, this etching produces needle-shaped surface structure. This recipe appeared, when it was noticed that addition of oxygen to fluorine-based plasma changes etch profile to more anisotropic. Oxygen forms protective oxide layer both on the walls and in the bottom of the etched trench. Oxygenation can be reduced by ion bombardment which is significant only at the trench bottom, where fluorine attack with concomitant etching of silicon will occur.

The scheme of the etching reactions can be written as:

$Si + xF + yO \rightarrow SiF_xO_y$ (reaction layer formation)

And depending on the O/F flux ratio, one of the two processes can prevail:

$Si + F \rightarrow SiF_4$ (etching)

$Si + 2O \rightarrow SiO_2$ (passivation)

This anisotropic silicon etching was employed for gyroid pattern transfer. The recipe has the following parameters: 80 mTorr, with O_2:SF_6 8:32 sccm, 30 W power.

The second recipe for silicon etch utilized mixture of gases $CHF_3/SF_6/O_2$ and etching in this case is more isotropic that for the black silicon recipe.

The three componets of the plasma have the serves as following functions:

1) SF_6 is chemical etchant for the substrate; SF_6 is the source of F• for the chemical etching of silicon with formation of SiF_4;
2) O_2 is passivator and blocks the etching at the sidewalls; oxygen produces O• radicals to passivate the silicon surface by formation of SiO_xF_y;
3) CHF_3 is local remover of the passivation layer at the bottom. CHF3 creates CF_x^+ ions to etch SiO_xF_y with volatile CO_xF_y production.

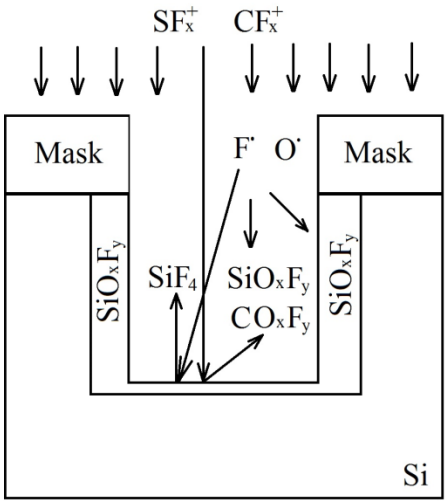

Fig. 3.3.1. Schematic drawing for silicon etch mechanism [95].

Alternatively, silicon etching could be performed on an ICP metal etcher (SF_6 : C_4F_8 70 : 35 sccm flow rate with ICP power 1200 W and RIE power 200 W at 1.9 Pa pressure), with etching rate of ~0.8 nm/s. This recipe and the previous one applied to our samles gave very similar results. In the recipe SF_6 is etchant, while C_4F_8 is a passivating component. This etching process is called Bosch process. The passivation component forms polymeric nCF_2 on the walls and in the bottom of the etched trench. During etching the film in the bottom of the trench is reacting with F• radicals. After protective film is removed the exposed silicon begins to be etched. But nCF_2 film on the side wall reacts only with fewer off-vertical ions and cannot be entirely removed. The film protects side walls at higher degree and thus anisotropic etching is realized [96].

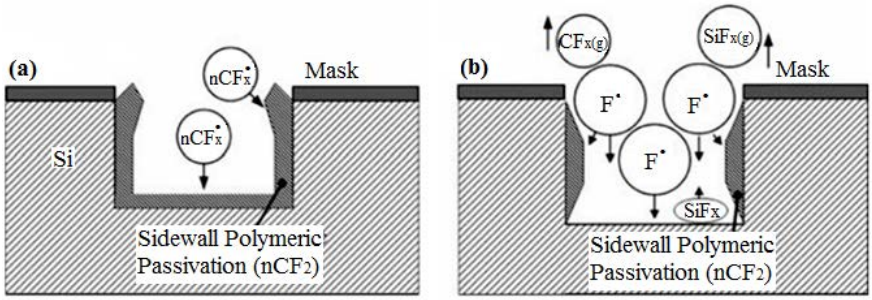

Fig. 3.3.2. Schematics of etching chemistry for Bosch prosess [97].

Recipies with Ar/O_2 mixtures were used for polymer and graphene etching. Argon addition causes inert ion bombardment of the surface, which results in enhanced anisotropic etching [98]. For mask thinning and graphene etching a strongly anisotropic recipe was used (O_2:Ar 5:45 sccm, pressure 10 mTorr, power 30 W, mask etch rate ~1 nm/s). The oxygen atom attack of a polymer can proceed by a variety of mechanisms including [99]:

(1-3) Abstraction by oxygen: oxygen radical steals hydrogen from the polymer chain.
(4) Oxygen addition: an oxygen radical attacks a double C=C bound, forming epoxy group.
(5) Dissociation by oxygen: oxygen radicals transfer their electrons to polymer and form molecular oxygen.
(6) Oxidation and (7) chain scission: oxygen attaches to the chain and breaks it. Multiple chain scissions and oxidation of organic polymer form ultimately volatile CO_2 and CO.

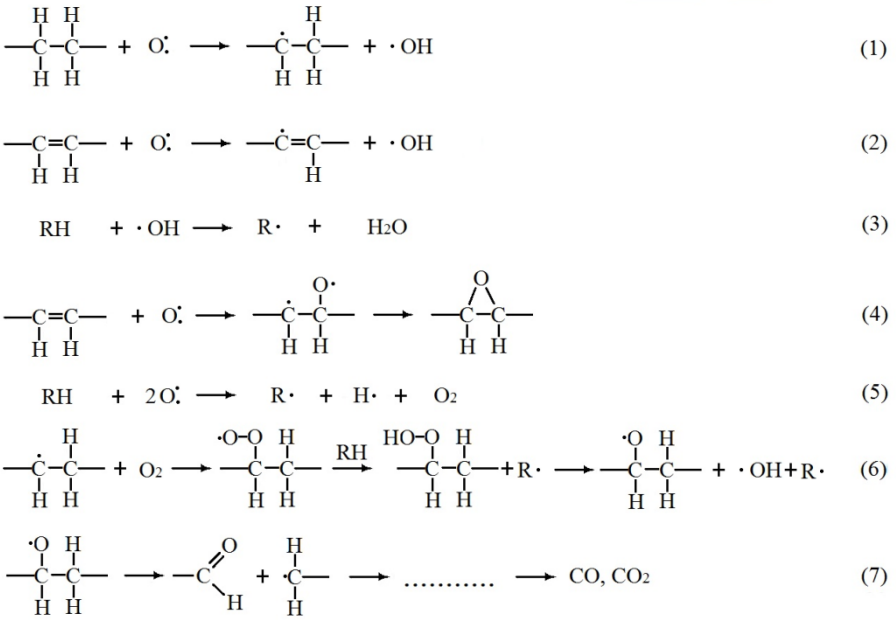

Fig. 3.3.3. Schemes of the possible reactions during oxygen plasma etching.

3.4. Wet etching for single-lamellar mask preparation

Spin-coating gives flat films, but the morphology of the BCP in a film is difficult to predict and control. The morphology of bulk BCP is known and can be effectively aligned, but *ex-situ* preparation of the polymer mask with microtome suffers from several disadvantages. Mask surface has scratches made by polymer dust accumulated on the knife edge, "wavy" thickness variations due to compression and unevenness due to external shaking during slicing. Thin layers of polymers obtained by bottom-up approach wouldn't have these imperfections. Layered structures with flat interfaces are naturally self-assembled in bulk lamellar BCP.

Bulk LAM BCP can be aligned by shear into parallel lamellae with surface roughness depending on Flory-Huggins interaction parameter. By cross-linking one of the blocks and etching another one separated lamellar can be obtained. Solid homogeneous lamellae, of course, cannot be used as masks for lithography, but in morphologies like HPL, and in some triblock copolymer morphologies (fig. 3.4.1) half of the lamellae are nanostructured. In the case of HPL morphology wet etching of the majority phase (black in fig. 3.4.1 a) will lead to formation of the perforated polymer lamellae swimming separately in the etching solution. Another option is to use triblock copolymers or star block copolymers, for example like the one obtained in [100] (fig. 3.4.1. right). Triblock copolymers self-assembled in alternating lamellae of two different polymers, one type of lamellae consists only of one type of polymer units (A) and the other lamellae of polymer (B) bearing cylinders of the third polymer (C) inside. We can align the bulk triblock copolymer and then selectively remove the A polymer lamellae, obtaining smooth layers of B polymer with cylinders of C inside as a lithographic mask for hexagonal pattering. Possible types of polymer units are: A=poly(lactic acid), B=poly(butadiene) or polystyrene and C=poly(dimethylsiloxane) or poly(methyl methacrylate).

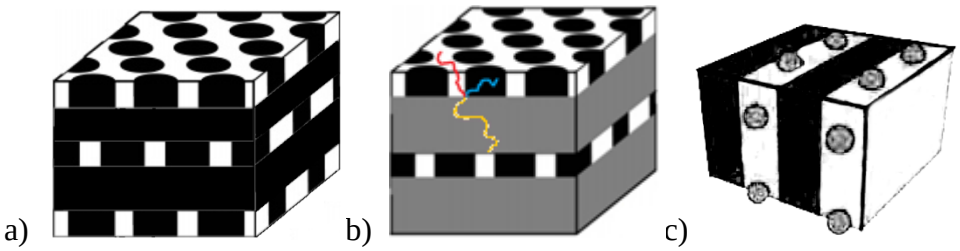

Fig. 3.4.1. Possible precursors for mask fabrication by wet etching a) HPL diblock copolymer; b) star triblock copolymer; c) linear ABC triblock copolymer.

The approach was tested by wet etching separation of single lamellae from a lamellar block copolymer 1,2-PB-b-PDMS. The block-copolymer was aligned by shear between two glasses. This made lamellae to orient parallel to the shearing plates. Polybutadiene was cross-linked and then PDMS was etched with TBAF in THF and the whole structure collapsed, but remained as one large piece. The sample was washed by mixtures of THF/ethanol with increasing percentage of ethanol to remove TBAF and the etch products. Then the sample was gently scratched parallel to the surface and dust collected into a bottle with solvent, THF or ethanol. Ultra-sonication was used for delamination and the solution became milky. Then it was dropped onto a silicon wafer and left to dry. As a result, numerous one-layer thick flakes were observed on the silicon, some are showed in fig. 3.4.2.

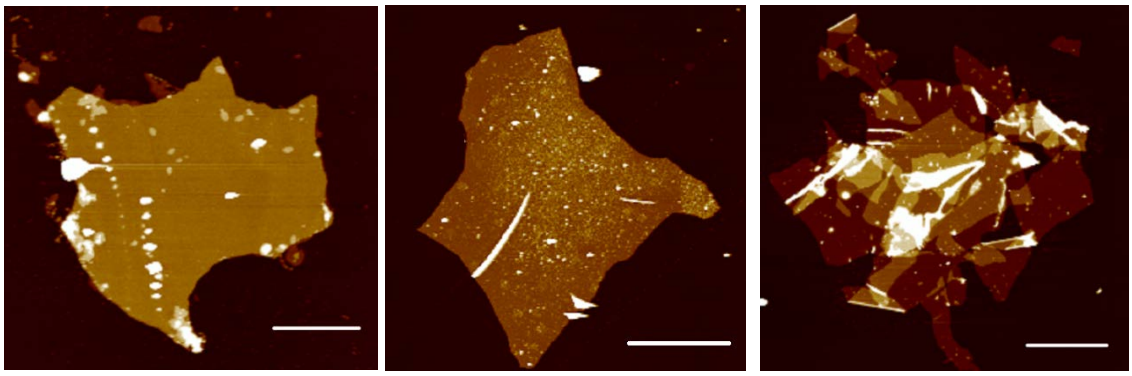

Fig. 3.4.2. AFM images of cross-linked polybutadiene flakes on silicon wafer. Left to right: one of the largest single flakes; flake with wrinkle; heap of overlapping flakes. All scale bars are 5 μm.

The thickness of flakes was measured as 17-20 nm. The largest flakes have sizes of ~15 μm. This way of mask preparation has advantaged and disadvantages compared to the microtome-based method:

1) Thinner flakes can be obtained (18 nm thin in our case);
2) Flakes have more uniform thickness without any scratches or other artifacts related to top-down fabrication;
3) Only one thickness is possible. Changing of the thickness requires new polymer synthesis;
4) Solvent dried on flakes brought contaminations;
5) Flake sizes are smaller;

6) No control of the deposition place. Flakes lie on top of each other.

4. Conventional lithography: PS-b-PMMA thin film self-assembly

The optimized recipe from ref. [69] was at first precisely repeated, but only ~60% of the cylinders in the resulting nanoporous PS mask were oriented perpendicular relative to the substrate. In order to increase the percentage of "standing" cylinders an effort was made to find the new optimum conditions. Published parameters were used as the starting point and were varied to improve the final results.

4.1. Optimization

The first optimization was made by tuning film thickness and changing the annealing temperature. According to the recipe, optimal thickness is in range 30-35 nm after annealing. Thicknesses in this range were obtained by spin-coating 0.8w% solution of PS-b-PMMA in toluene. Films were cast at six different rotational speeds in order to fine tuning thickness: 1000, 2000, 2500, 3000, 4000, 5000 rotations per minute (rpm) for 1 minute. For thickness measurement spin-cast films were gently scratched with a tweezer in order to remove film without damaging the substrate. Thickness of the film was measured by AFM profile in several places before and after annealing (see tables 4.1.1 and 4.1.2).

	Thickness of the BCP film for different annealing conditions, nm			
Speed, rpm	Non-annealed	180°C	200°C	235°C
1000	43; 44; 40; 38; 41; 42; 43; 37; 39;	43,5; 40,5; 41,5; 44,5	44; 50; 40	41; 40,5
2000	41, 35	34; 36; 32,5	36,3; 36,3; 37,6; 37,5	33.8; 32,8
2500	34, 34, 34,5	32; 33; 33,5	34; 33,5	33; 31-32,5;
3000	n/a	32,5; 31; 33,5	31,6; 36,2; 31,2	31,4; 32,6; 31
4000	35.5, 34	32,4; 31; 35	32; 31	36.8; 34,6; 37; 42
5000	34,5, 33, 35, 30, 33	35,5; 35; 37	34; 40; 32,5	36; 32,5; 34,5

Table 4.1.1. AFM thickness measurements for BCP films cast from a 0.8w% solution in toluene on LrCP

	Thickness of the BCP film for different annealing conditions, nm			
Speed, rpm	Non-annealed	180°C	200°C	235°C
1000	42,5	42,4; 45,8; 42,8	46; 42,4; 45	40,5; 37; 41
2000	38; 36,5	35; 33,5; 35,6	33,9; 35,8; 34	32,3; 29,6; 36
2500	37,4; 37,5; 29-32;	33,1; 34	33,8; 35,9	34-36,6; 33,5
3000	n/a	34,5-35,5; 35,5	34,4; 35; 34,4	37,8; 36,5
4000	37; 35	37; 32,2; 29.8;	32; 36,6; 35,5	32; 32,6
5000	41; 36,5; 37,5; 30	39; 36-37; 33-34	32-31; 33; 32,5	37-38; 33,5-34,5

Table 4.1.2. AFM thickness measurements for BCP films cast from a 0.8w% solution in toluene on PrCP

A set of annealing temperatures was tried for each thickness in order to optimize the top interface energy. 24 samples of 6 different thicknesses and 4 different annealing temperatures were prepared on two different random copolymer brushes LrCP and PrCP. SEM images of nanoporous PS mask on LrCP and PrCP are collected in the working matrices in tables 4.1.3 and 4.1.4, respectively. In the SEM images vertical holes are surrounded by a bright white rim, because more SE escape from there due to the edge blossom effect. Thus on lower magnification images regions with “standing” cylinders are white and can be distinguished from darker regions of “lying” cylinders.

On all SEM images both “standing” and “lying” cylinders are present. Annealing at 180°C, 200°C and 225°C gives similar results for all samples and masks have roughly the same percentage of “standing” cylinders. Annealing at 235°C clearly favors “lying” cylinders. For example, the vast majority of the cylinders lay parallel to the substrate to the substrate for the sample prepared on LrCP at 2000 rpm and annealed at 235°C; “standing” cylinders form small groups of 1-9 hundreds of nanometers far apart from each other.

For the thickest samples on both random brushed, i.e the samples spin-cast at 1000 rpm, annealing at the highest temperature leads to mild dewetting and formation of a mesostructured of isles on the surface (fig. 4.1.1). Isles have the same height of 17 nm. The difference in film thickness affects cylinder orientation in the film. The SEM image in table 4.1.4 for 1000 rpm, 235°C shows two of the isles. It is clearly seen, that in the centers of the isles and between them the percentage of “lying” cylinders is larger than in the vicinities of isles borders. Films became uneven in two more cases (PrCP, 5000 rpm, 235°C and PrCP, 1000 rpm, 200°C). Thicker areas consist mainly of standing cylinders, thinner areas can bear lying cylinders (PrCP, 1000 rpm, 200°C) or be unstructured (PrCP, 5000 rpm, 235°C).

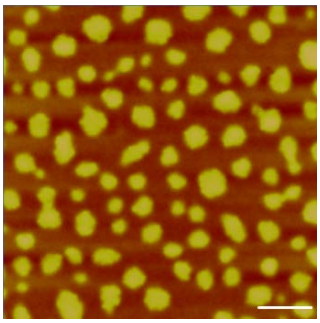

Fig. 4.1.1. Dewetting. AFM image of uneven after annealing at 235°C film. All isles are 17 nm high. Initial film thickness 40 nm. Scale bar is 5 μm.

rpm	180°C	200°C	225°C	235°C
1000	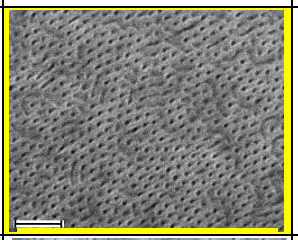	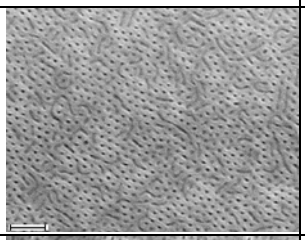	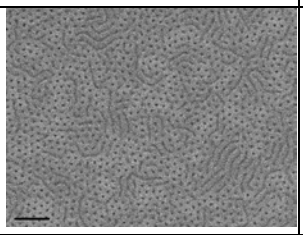	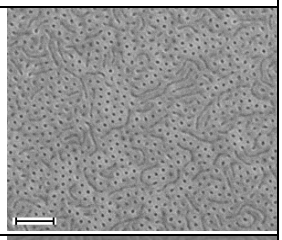
20000	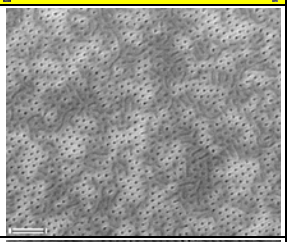	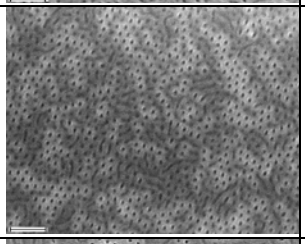	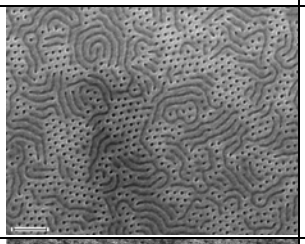	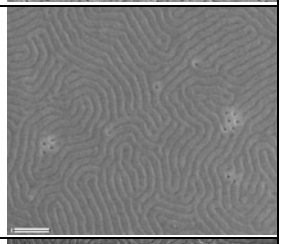
25000	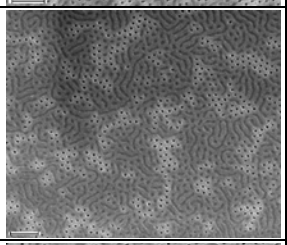	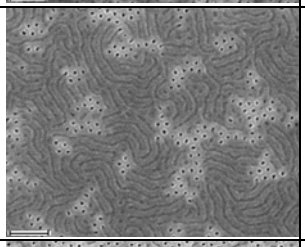	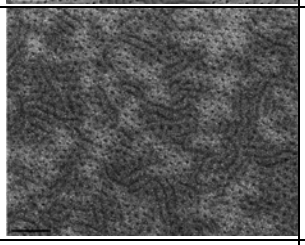	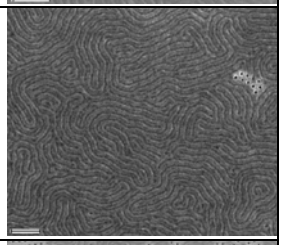
30000	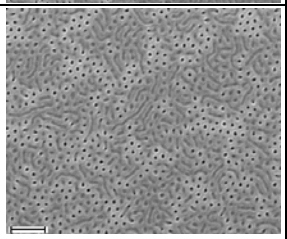	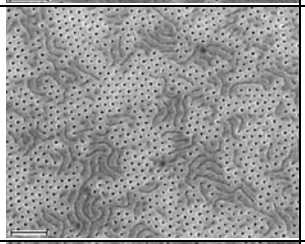		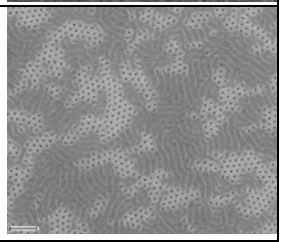
40000	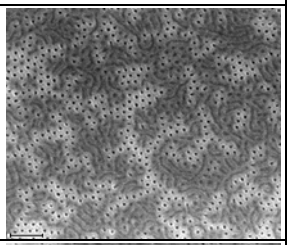	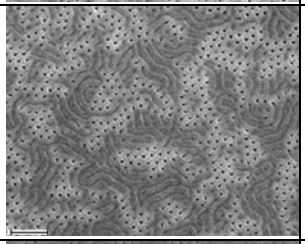	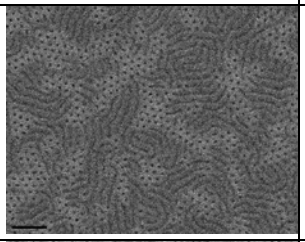	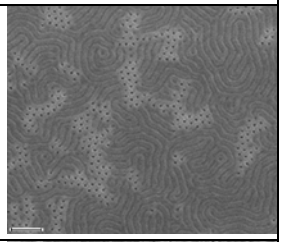
50000	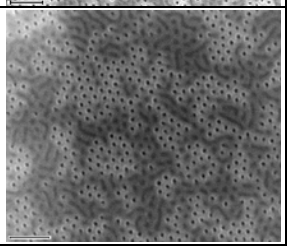	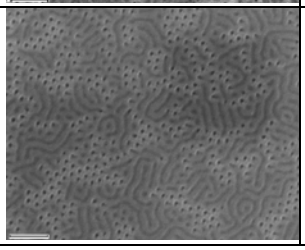	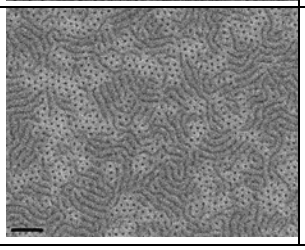	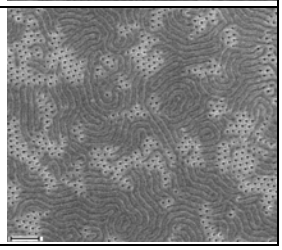

Table 4.1.3. Work matrix showing SEM images of nanoporous PS masks on LrCP for different fabrication conditions. Columns differ in annealing temperature, rows – in rotational speed at spin-casting. All scale bars are 200 nm. Best conditions marked with yellow.

rpm	180°C	200°C	225°C	235°C
10000	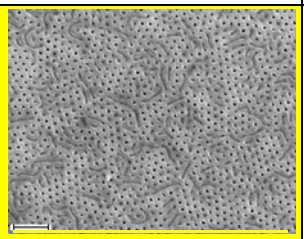	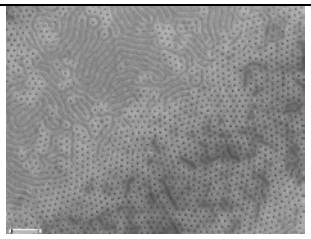	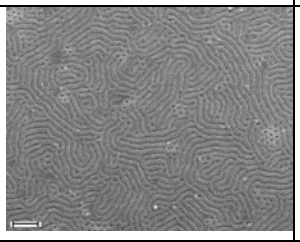	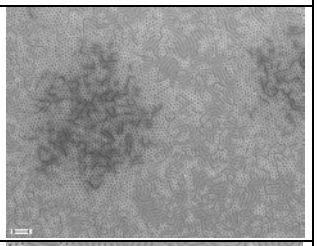
20000	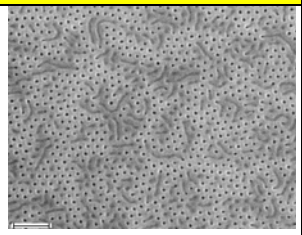	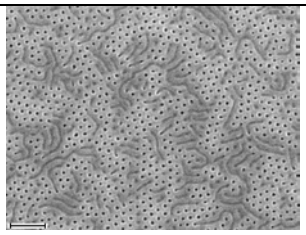	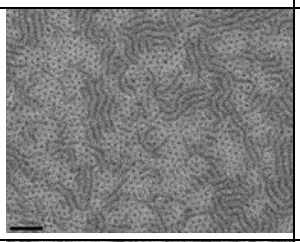	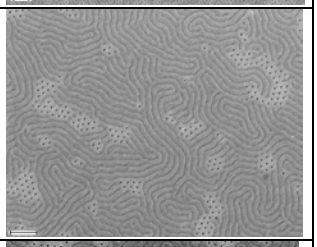
25000	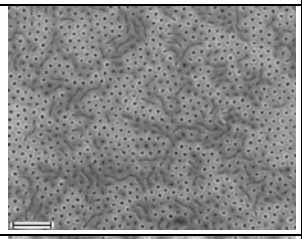	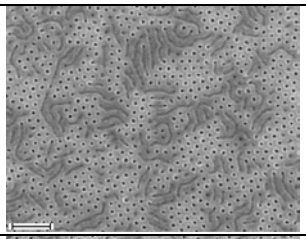	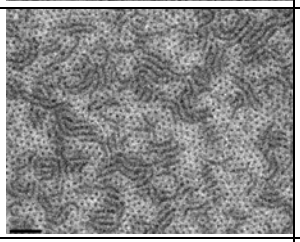	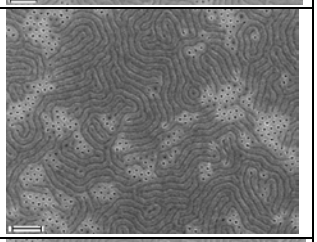
30000	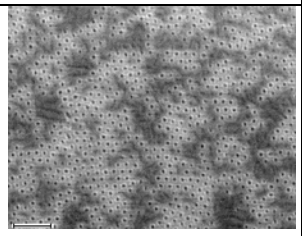	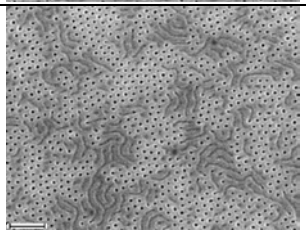		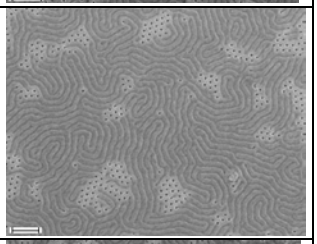
40000	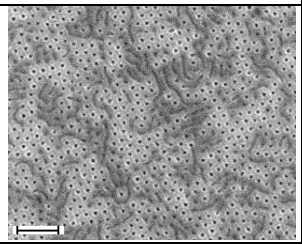	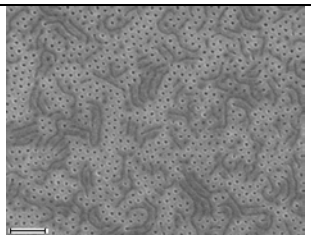	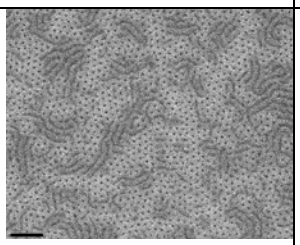	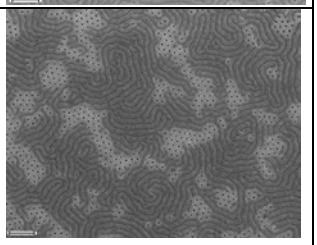
50000	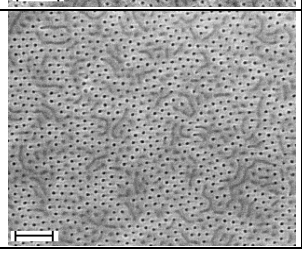	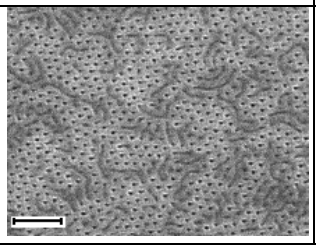	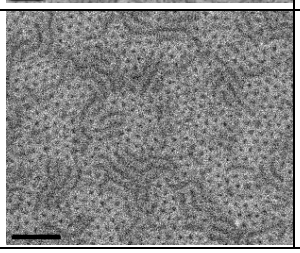	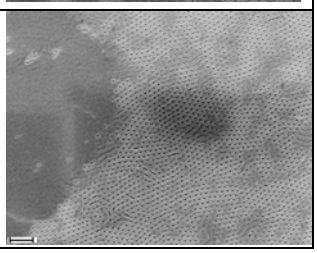

Table 4.1.4. Work matrix showing SEM images of nanoporous PS masks on PrCP for different fabrication conditions. Columns differ in annealing temperature, rows – in rotational speed at spin-casting. All scale bars are 200 nm.

Although the optimal film thickness reported in ref. [69] is 30-35 nm, in our experiments the highest percentage of standing cylinders (~70%) was obtained for the slowest rotational speed yielding the film thickest of ~40 nm. This thickness is close to 39 nm, which is center to center distance between the PMMA cylinders in the BCP. Because our results were far from these described in the article, it was decided to go investigate the effect of film thickness on the morphology. Films deposited from a 0.4 w% solution of PS-b-PMMA in toluene were 15-20 nm thick and demonstrated strong dewetting behavior (fig. 4.1.2 a). Most of the wafer was covered with the thin unstructured layer and phase-separated structure appeared only around the islands with larger thickness. Films, prepared by spin-casting of a 1.1w% solution of BCP in toluene, had thicknesses 45-50 nm. The film became uneven after annealing. It formed numerous oval holes 1-2 μm size and 10-14 nm deep. The alignment of cylinders was worse than for the films cast from the 0.8w% solution.

a) 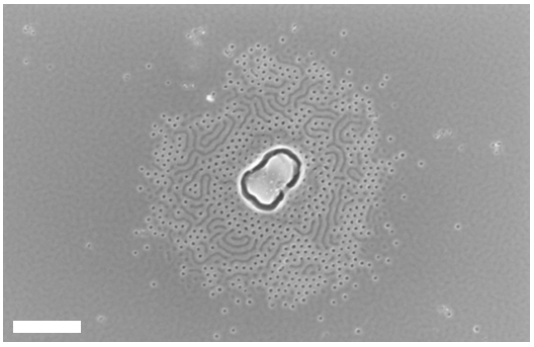 b) 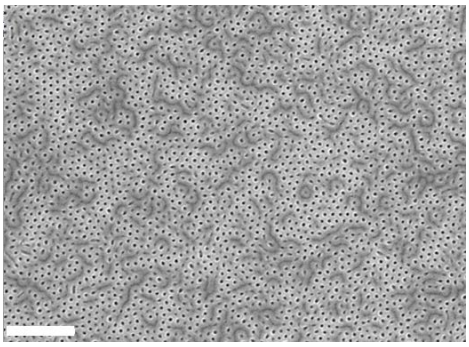

Fig. 4.1.2. SEM image of a) dewetting on film 0.4w%, casted on LrCP at 2000 rpm, annealed at 200°C. b) Microphase separation in 1.1w%, 2000 rpm, LrCP, 200°C. Both scale bars are 400 nm.

Additional cleaning to ensure chemical uniformity of the substrate prior to random brush grafting with both oxygen plasma and piranha did not improve the results.

At last we investigated the effect of composition of polymer brush on the final morphology. Two other articles, [101] and [68], report that the styrene content in the random brush should be increased in order to obtain “standing” cylinder orientation in PS-b-PMMA film. According to ref. [101], the fraction of PS should be more than 59mol% for OH-terminated PS-r-PMMA in order to orient all cylinders perpendicular to the substrate. For HEMA containing random copolymer , the fraction of PS should be more than 62mol%. This data is in agreement with ref.

[68], where the random copolymer brush had 70% of PS. For comparison, our random copolymers contained only 55mol% styrene, and this discrepancy could have been the reason for the imperfect out-of-plane cylinder orientation we had experienced in the previous experiments.

The average brush composition was tuned by adding controlled amounts of OH-terminated polystyrene (M_n = 15000) to the random copolymer solution. The brush was layer prepared by spin-coating of solutions of LrCP mixed with PS-OH in the following weight proportions: 7:2, 7:4, 7:7, and only PS-OH. The resulting molar percentages of styrene in the mixed brushes were 65%, 71%, 77% and 100%. SEM images of the obtained nanoporous PS masks prepared on the new brush mixtures are collected in table 4.1.5. The best nanoporous masks are highlighted with yellow background. The percentage of standing cylinders in these masks is ~80%, which is clearly an improvement relative to the results obtained with the brushed containing 55mol% PS.

PS mol%	0.8w%, 1500, 180°C	1.1.w%, 4000, 180°C
65	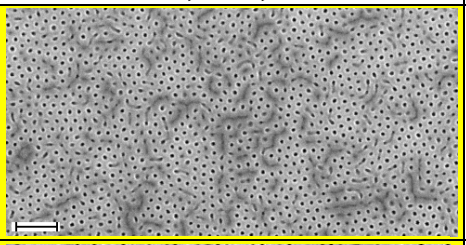	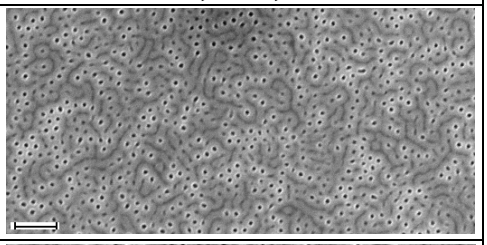
71	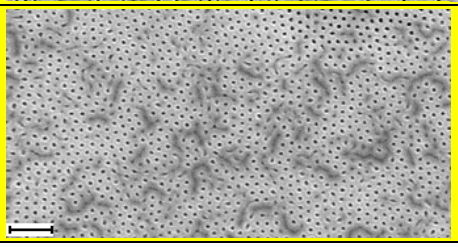	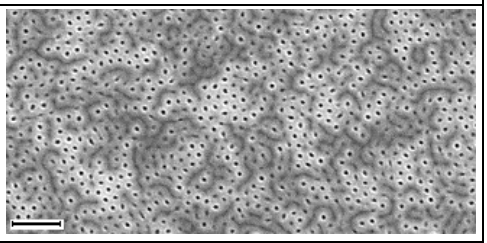
77	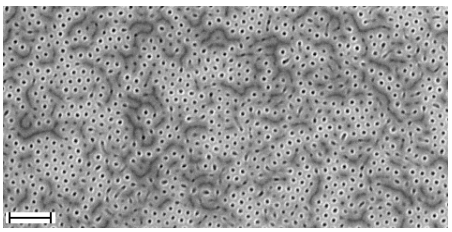	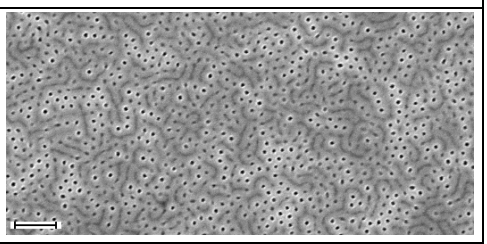
100	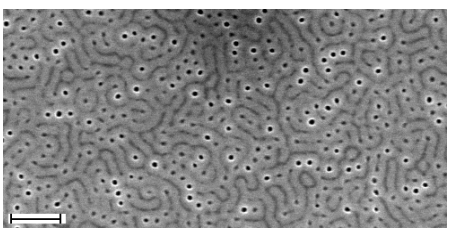	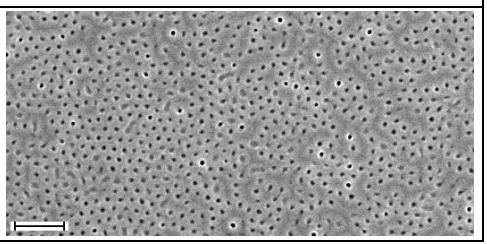

Table 4.1.5. Nanoporous PS masks obtained by self-assembly of PS-b-PMMA on brushes with increasing molar fraction of PS.

Probably wrong concentration of PS in the random brush did not allow us to orient all the cylinders perpendicular to the surface. Since optimization of PS content would require additional random copolymer synthesis, which is time consuming, it was decided to finish this activity by pattern transfer to silicon without further improvement of the mask quality.

4.2. Transfer of the pattern to silicon

Pattern was transferred in ICP Metal Etcher by applying the Bosh recipe for silicon etch. Silicon etching speed for this recipe is ~0.8 nm/s. The pores of the mask don't reach the silicon surface: there is random brush between the nanoporous PS mask and silicon, as well as possible rests of PMMA inside the pores. The pattern can be transferred by one-step silicon etching, because this recipe etches both silicon and polymer mask. Mask etching by this recipe is more isotropic and slower than that of the silicon.

Results of pattern transfer from masks with high percentage of standing cylinders (LrCP, 0.8w%, 1000 rpm, 180°C) by one-step silicon etch are shown in table 4.2.1. The first column contains time of etching, the second shows SEM images of the surface after the mask residues were completely removed by high-energy oxygen plasma cleaning. Replicas of standing cylinder appeared first after ~50 seconds of etching. This is time necessary to etch through the thinnest parts of the random brush to silicon. Holes in the silicon substrate became deeper with increased etching time and more holes appeared in the places where the residual layer was thicker. Most of the holes were transferred to the substrate after 110 seconds of etching. The 60 seconds of etching time lapse from the first appearance of transferred holes to final transfer is caused by uneven thickness of the residual polymer layer. In one-step etching the optimal pattern consisting of both holes and lines appeared after 130 seconds of etching.

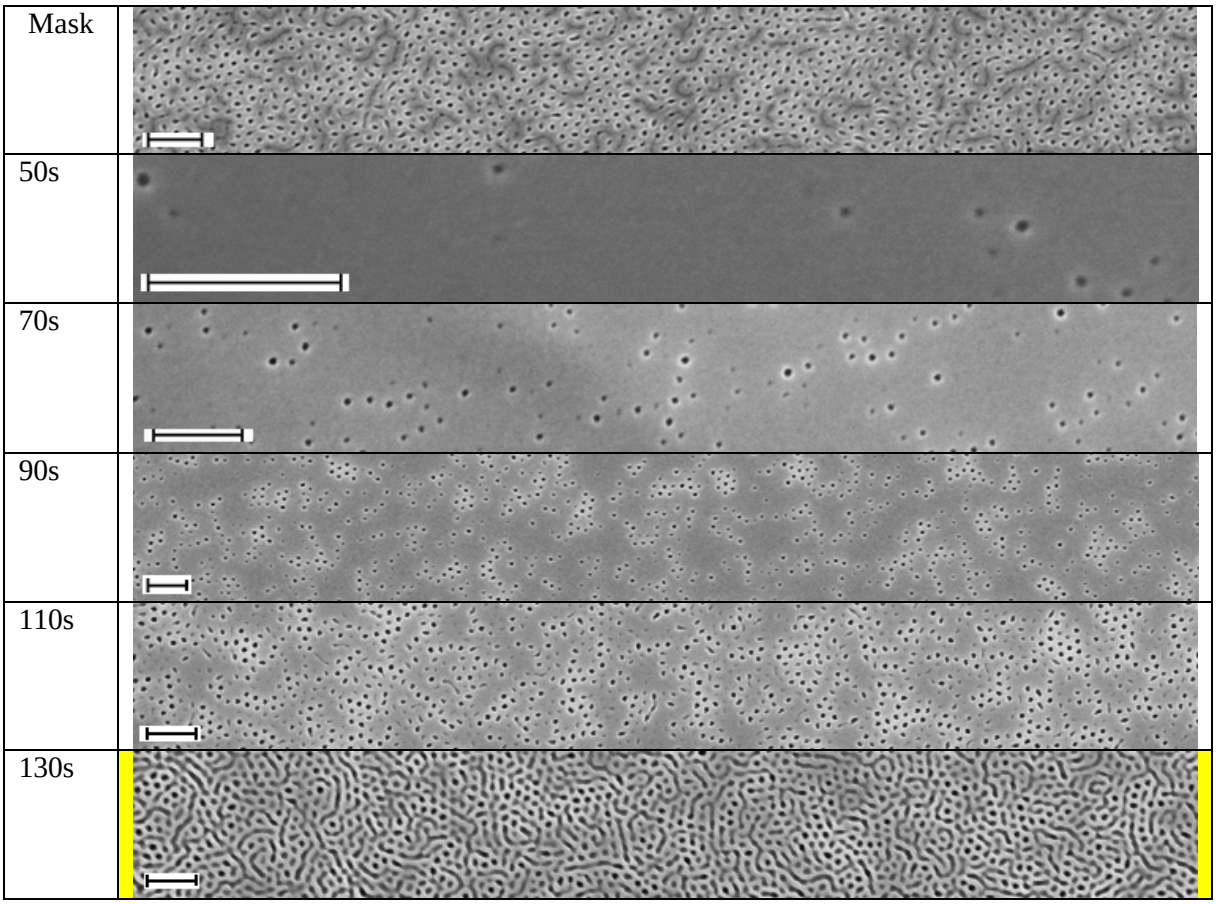

Table 4.2.1. Initial PS mask and pattern on silicon for different etching times. All scale bars are 200 nm.

Mild oxygen plasma treatment in order to etch random brush and clean pores can be performed prior to silicon etch. Oxygen plasma cleans and enlarges the pores. Since it does not etch silicon, this treatment reduces the difference in thickness of the residual layer. 10 seconds of oxygen plasma treatment improves the quality of the transferred pattern and reduces the optimal time of silicon etching by 50 seconds, as illustrated in table 4.2.2.

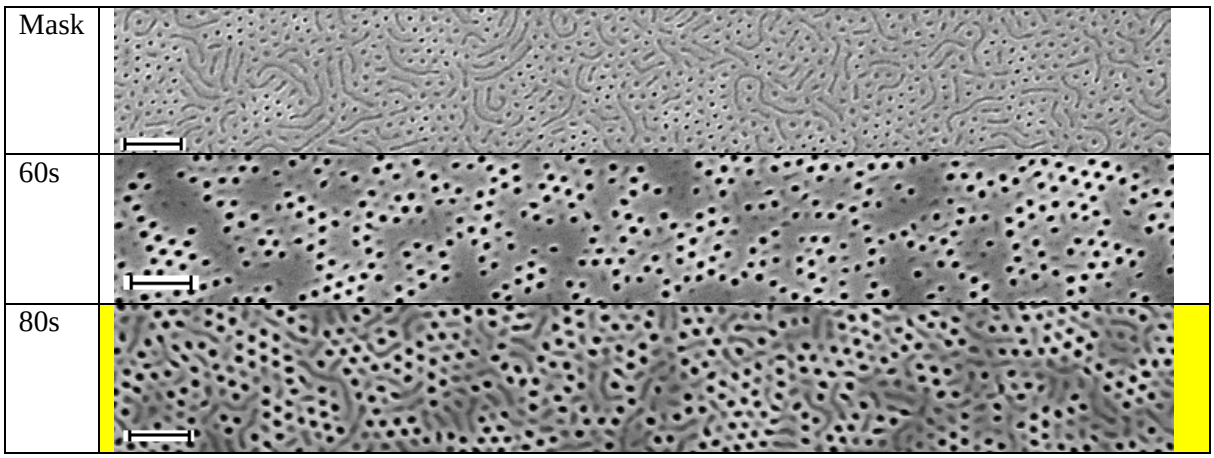

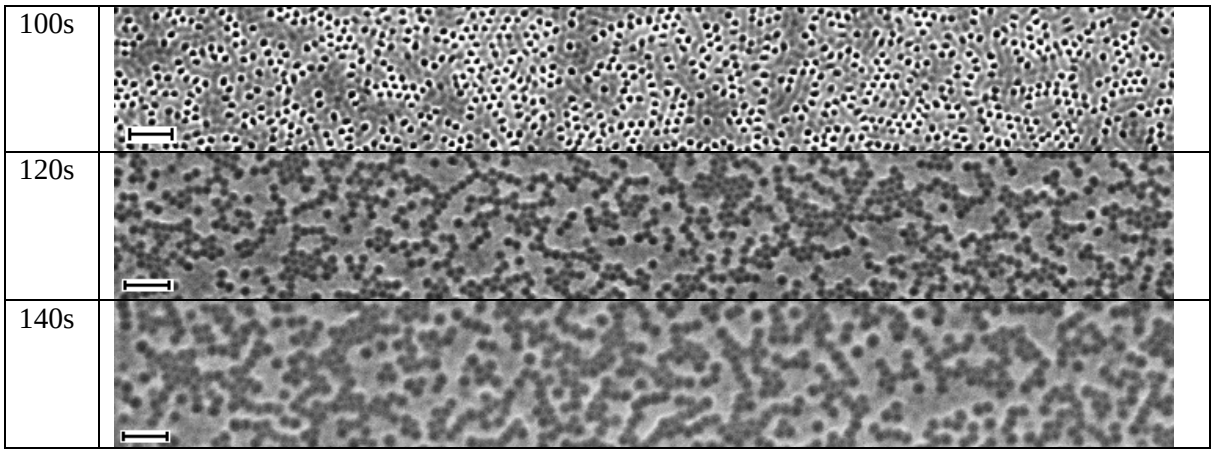

Table 4.2.2. Initial PS mask and pattern on silicon for different etching times. Prior to silicon etch 10 seconds of mild oxygen plasma etching was applied. All scale bars are 200 nm.

With reference to table 4.3.1 and table 4.3.2 we can conclude that pattern transfer to silicon evolves through the following steps with increasing etching time:

1) At short etching times no pattern is observed, plasma etches through the random brush and the remaining PMMA;
2) The first holes start to emerge under the deepest and cleanest pores;
3) The plasma etches through the thicker residual layer and more holes appear;
4) Projections of lying cylinders start to emerge;
5) Shallow patterns from “lying” cylinders are destroyed first, while the round holes expand;
6) The lines completely smoothen and the round holes merge;
7) The whole pattern smoothens.

Fig. 4.2.1 shows top-down view and a cross-section of the nanopatterned silicon at the optimal etching conditions, i.e. at 10 second of oxygen plasma treatment followed by 80s silicon etching. (top) cross-section was made (Fig. 4.2.1 bottom). The wafer was broken in two and one of the pieces was fixed in a 90° holder for SEM. Holes on the cross-section have different depths and widths. Holes transferred from lying cylinders are shallow and long in the cross-section. Holes transferred from standing cylinders are deep. If the crack crosses the center of a deep hole, its width on cross-section will be largest and equal to the hole diameter. If the crack goes off center, the hole in the cross-section will be narrower. From the SEM image the depth of holes was measured to be ~35 nm. That depth can be obtained in ~45 second of silicon etching with the speed 0.8 nm/s. That means, 35 seconds of total 80 seconds of silicon etch

were spent on etching through the mask. The total time of silicon etch could be reduced by increasing time of oxygen plasma treatment.

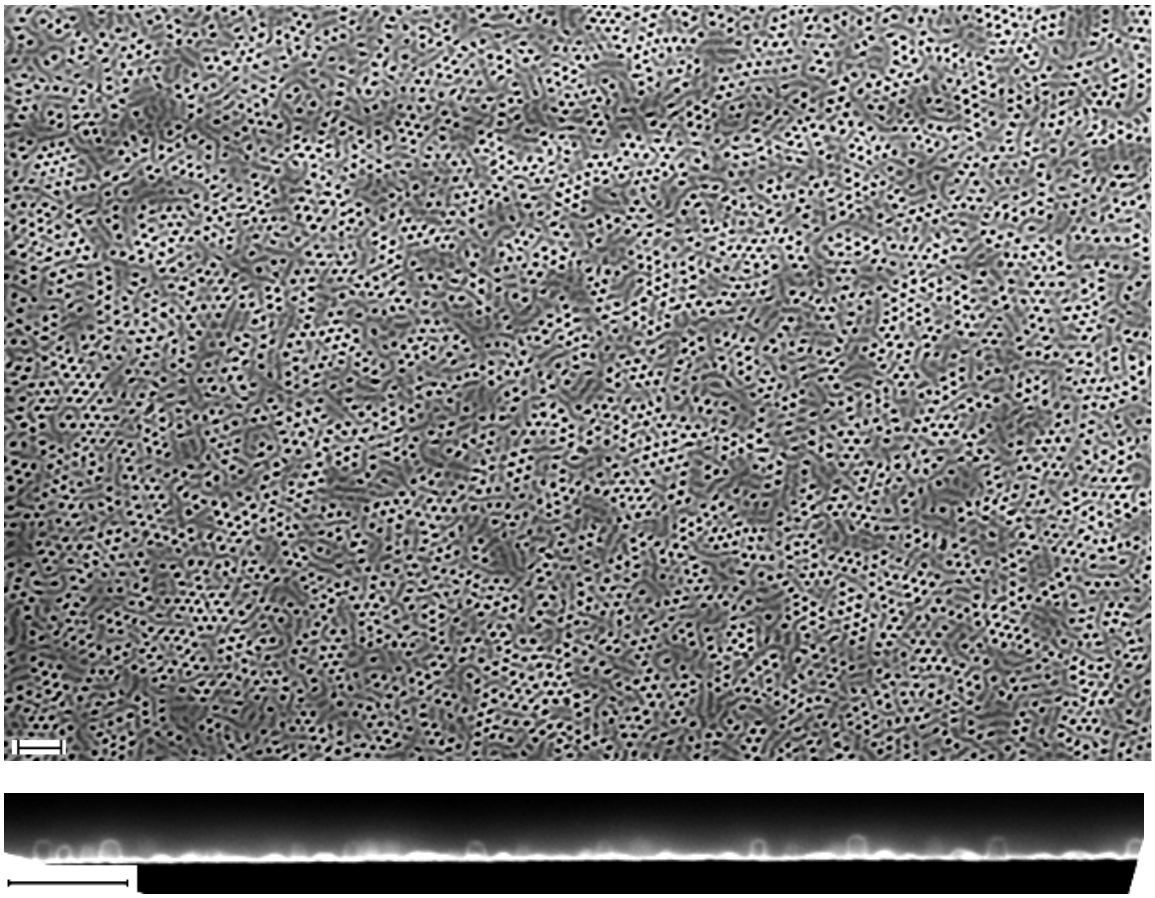

Fig. 4.2.1. SEM images of optimized pattern transfer: top-down view (top) and 90° cross-section view (bottom). Both scale bars are 200 nm. The estimated holes depth is ~35 nm.

4.3. Summary

Conventional lithography requires lots of optimization, even though the optimal conditions are known from the literature. Seemingly the procedure is not robust enough to reproduce in another laboratory by following the reported recipe. For PS-b-PMMA, the highest achieved percentage of “standing” cylinders was ~80%. Pattern transferred to the silicon consists of deep holes with an aspect ratio close to 1, formed under the standing cylinders and shallow lines, formed under the “lying” cylinders.

5. Silicon nanopatterning through *ex-situ* fabricated polymer mask

As described in the previous chapter, the conventional BCP lithography method requires fine tuning of multiple parameters even if recipe is known from literature. Therefor the fabrication of masks "*ex-situ*" from pre-aligned polymer monoliths is very attractive:

1) In the case of HEX block copolymers all cylinders can be oriented in the same direction.

2) The pattern has single-domain crystalline order on hundreds of microns scale, which is nearly impossible to achieve by conventional method without graphoepitaxy.

3) The mask is absolutely surface-independent.

4) Transfer of patterns from morphologies that don't exist in thin film (elliptical, gyroid) become possible.

However the microtome-based method for mask fabrication has drawbacks of its own:

1) The thickness may not be completely uniform due to "wavy" patterns caused by compression and steps caused by external vibration during the slicing process. Mask surface has scratches made by polymer dust accumulated on the knife edge. These non-uniformities disturb the adhesion of mask to substrate, and ultimately the quality of pattern transfer.

2) Masks form wrinkles and ripples at the deposition step, which limits the size of wholly patterned areas to ~50x50 μm^2.

3) The method is not scalable. The maximum section size recommended for ultra-sonic knife is 500 µm.

4) Complete removal of the mask can be difficult, which is also a common difficulty for spin-cast masks.

These aspects of the new method are discussed in the remaining of this chapter and in appendix 1.

5.1. Hexagonally packed cylinder morphology

Results of pattern transfer from mask cut off HEX monoliths were published in *Langmuir* (See attached article in appendix 1). Only a short summary is given in this subchapter.

Monoliths with hexagonally packed cylinder morphology (table 5.1.1. top row) can provide different masks depending on the mutual orientation of cutting plane and monolith's structure. The orientation of cutting plane can be determined by two angles: the angle relative to the cylinders axis (normal to the front fringe of cube) and the angle relative to one set of principal planes (top fringe of the cube). The values of the corresponding two angles for three different cuts are listed in the second row of the table. Nanoporous masks for lithography (4th row in table 5.1.1) were prepared at these three cutting plane orientations and etching conditions were optimized for each case. Final patterns transferred to silicon are presented in the last row of the table.

3D model	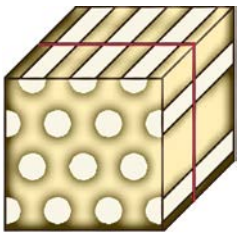	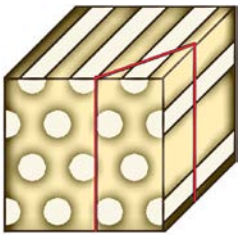	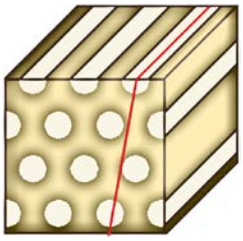
Cutting angles	90°, 90°	45°, 90°	0, 80°
50 nm thick cross-section	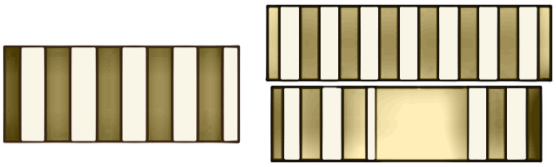		
SEM mask, 200 nm scale bars	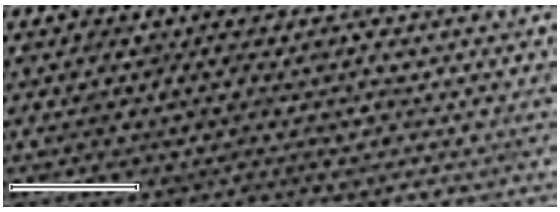	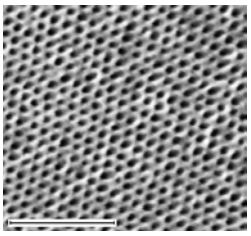	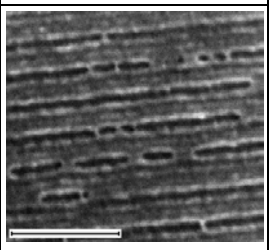
Pattern on silicon, SEM, 200 nm scale bars	HEX 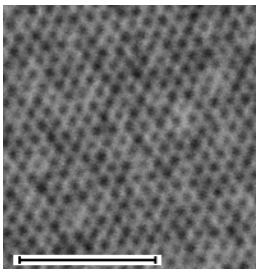 Moirè 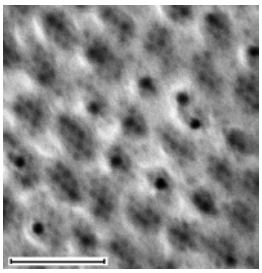	Elliptical 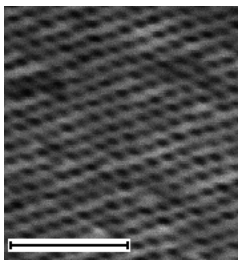	Lines 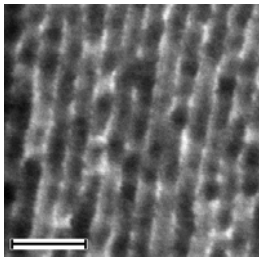

Table. 5.1.1. Summarizing table for possible patterns on silicon transferred from HEX nanoporous monolith. Red lines on the 3D models are intercepts of the cutting planes with faces of the structural cube.

Cutting perpendicular to the cylinders axis gives nanoporous masks with channels perpendicular relative to the substrate. The pattern on the mask is hexagonally packed round holes. Imperfect contact between the mask and substrate caused by mask roughness lead to strong undercut during etching. A root-mean-square (r.m.s.) roughness of 0.9 nm was measured by AFM on 2x2 μm^2 sample area (fig. 5.1.1), the same for both the nanoporous mask and the nanostructured silicon. The AFM profiles clearly show that main contribution to the roughness is made by structures with sizes larger than the period of microphase separation. Thus the pattern transferred to silicon is the overlap between the HEX pattern and a chaotic structure with characteristic length scale of ~ 100 nm. This overlap gives rise to different shades of background visible in the SEM image at the bottom-left corner of table 5.1.1.

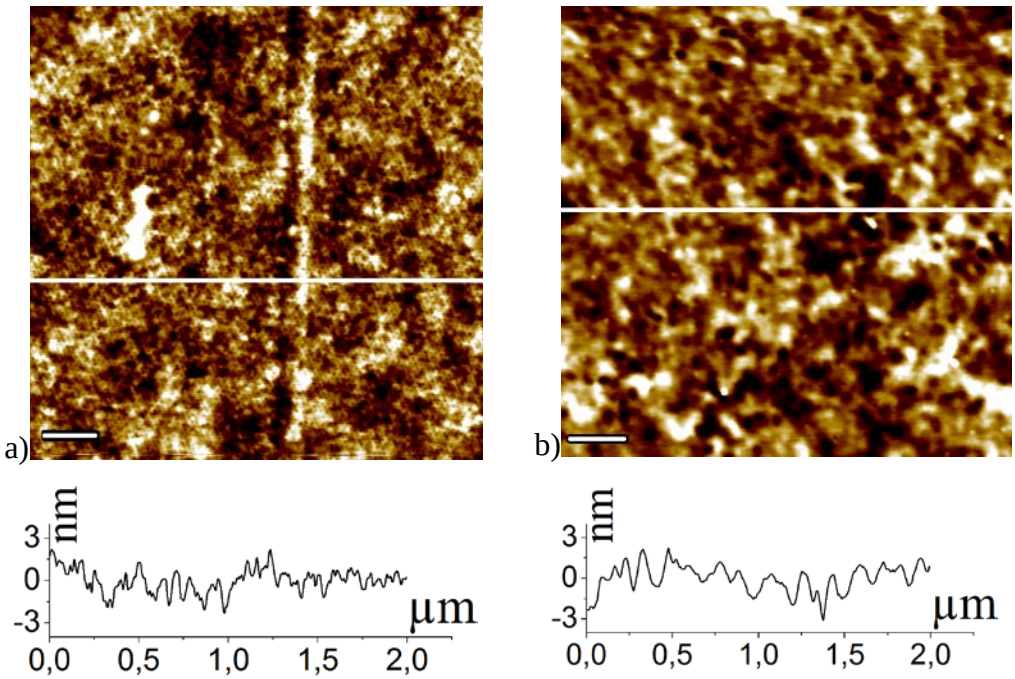

Fig. 5.1.1. AFM images of a) nanoporous mask and b) nanostructured silicon with the corresponding AFM profiles along the shown lines. 200 nm scale bars.

Optimization of black silicon etch recipe failed for transfer of HEX pattern. During the etching, holes appear in random places, rapidly become larger than the period of HEX structure and merge. Picture of the randomly placed large holes showed in the fig. 5.1.2.

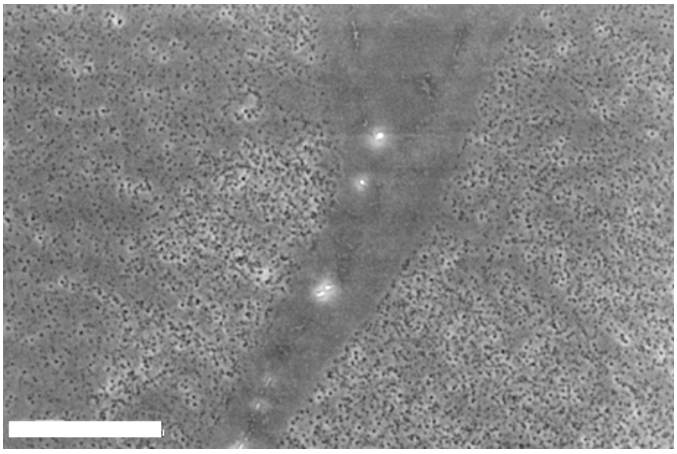

Fig. 5.1.2. Silicon surface for 20 s Ar/O_2, followed by 10 s of black silicon etching. 2 μm scale bar.

In the case of two superimposed HEX masks moiré patterns can be formed. The dual structure from such pattern is transferred to silicon as shown in the bottom row of the Tab. 5.1.1. The small HEX pattern of the ground period (period of original polymer mask) is visible inside a larger HEX moiré structure. The formation of moiré patterns requires crystalline-like order of the superimposed masks, which was rendered possible by the effectiveness of the shear-alignment. The large moiré structure period is formed by undercut etching. If there were no undercut, moiré pattern would look like groups of hexagonally arranged holes separated by the intact silicon surface, as ideally illustrated in fig. 5.1.3.

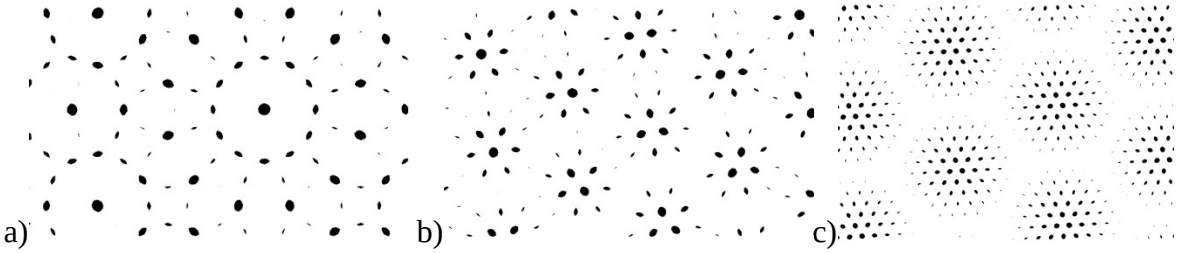

Fig. 5.1.3. Ideal moiré patterns in the case of complete absence of undercut for superimposition of two HEX lattices rotated by 30° (a), 14° (b) and 6° (c).

Other patterns were obtained by decreasing the angle of the cutting plane relative to cylinder axis. In this case pores are tilted relative to the substrate. The HEX pattern will become distorted and round pores will be stretched into ellipses in the direction determined by the angle

between the cutting plane and the top fringe of the cube (fig. 5.1.4). The pattern transferred to silicon is not only a projection of elliptical holes of the mask but depends on the whole 3D structure.

For small angle decrease change of the pattern is minor. For example, for slicing at 70° relative to the cylinder axis (20° decrease), the period stretches from 23 nm to 24,5 nm and elliptical shape of pores on the mask is not clearly seen. In order to get patterns that are clearly different from HEX, the cutting was performed at 45° relative to the cylinder axis (second column of table 5.1.1). Holes on the nanoporous mask are clearly elliptical in SEM and channels are oriented at 45° relative to the substrate. The pattern was transferred by applying twice longer silicon etching time than for the 90° cut. A slit-like pattern was transferred to the silicon substrate. The necessity to etch the mask material during pattern transfer caused a lower contrast of the transferred pattern.

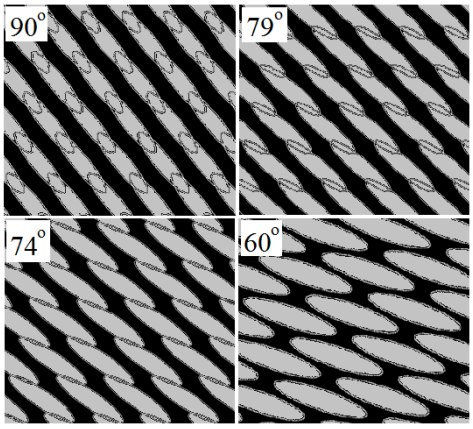

Fig. 5.1.4. Illustration of the influence of the second cutting angle (angle between the cutting plane and the cube top fringe) on the relative pore orientation in a 30 nm thick mask. The value of the first angle (i.e. the angle relative to the cylinder axis) is 45° for all the projections.

With further decrease of the cutting angle ellipses start to merge into lines. Cutting parallel to the cylinder axis gives masks with cylinders parallel to the substrate. Since the thinnest masks obtained by microtome were 30 nm thick, the mask is always multilayer (at least 1.5 layer). This decreases etching contrast even more and the transferred line pattern is very unclear.

5.2. Gyroid morphology

The gyroid polymer monolith was prepared from block copolymer BD40 with weight composition of PB:PDMS 49.5:50.5. It has lamellar morphology at room temperature, but at 110°C it transits to gyroid morphology. After the sample was heated up to 140°C and cross-linked, a multidomain structure of differently oriented grains with gyroid morphology was obtained. Pieces of gyroid polymer were etched by TBAF in THF. Nanoporous gyroid monoliths were sliced with ultra-sonic knife at room temperature. Different gyroid projections were observed in SEM after slicing (fig. 5.2.1). The most common one is knitting-pattern projection (top right). Grain sizes are in the range of 2-8 μm.

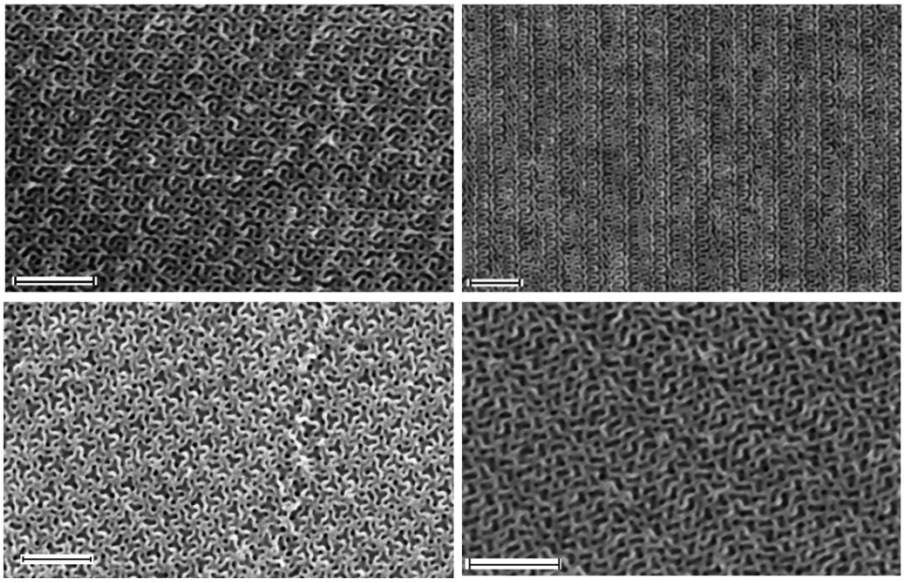

Fig. 5.2.1. Different gyroid projections in SEM. All scale bars are 200 nm.

Because grains have different orientation and channels are not perpendicular to the surface, etching through mask is required. This complicates the situation in comparison to the HEX cylindrical case, where all channels were perpendicular to the substrate and all holes were equivalent. The necessity to etch through the mask makes the process strongly thickness-dependent. Etching times, optimal for one grain, are not optimal for the other. This difference in etching time can be redused by thinning the mask with anisotropic oxygen plasma etching of the mask. A typical pattern transfer procedure includes first a “mask-thinning” step with anisotropic etching by O_2/Ar plasma, followed by anisotropic/or isotropic silicon etch and a final mask removal by long oxygen plasma cleaning. Patterns transferred to the silicon surface can be observed in SEM. Results of black silicon etching (fig. 5.2.2) clearly show difference in

the degree of nanostructuring for different grains of the same mask. Light grey areas are the most etched. They coexist with dark grey areas, where silicon was not etched at all or just some single holes were transferred to the surface.

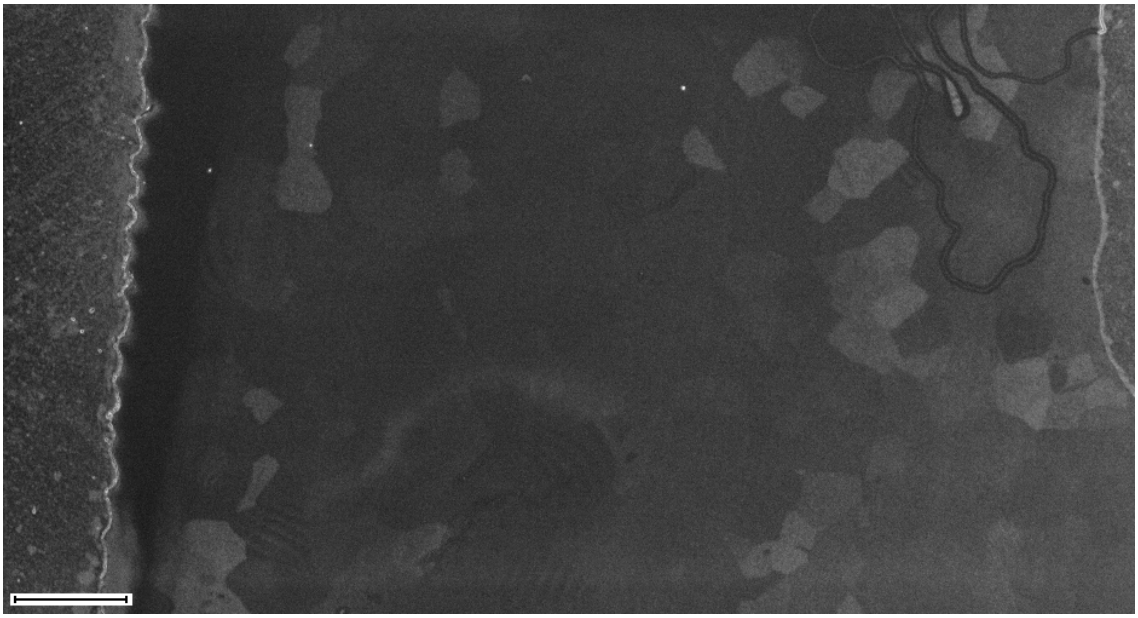

Fig. 5.2.2. Etched silicon surface after the gyroid nPB mask removal. Different shades of grey correspond to different etching degree for different grains. 10 μm scale bar. (30 s O_2/Ar + 9 s black silicon etch)

Alternatively isotropic silicon etching can be performed for pattern transfer. Figure 5.2.3 shows etched silicon surface after 32 seconds of isotropic silicon etching. At low resolution SEM all grains show large period wavy patterns. The mechanism of formation of these waves is illustrated in fig. 5.2.4. Knitting-pattern is the most common on the surface of microtomed gyroid flakes, and assuming complete random orientation of the grains, we can say that in mask cross-section knitting patterns also will be the most common. We can imagine a ~40 nm thick mask (fig. 5.2.4) where stripes of loops and wavy lines of the knitting pattern are at an angle of 6° relative to the substrate plane. In this case repeating elements in the perpendicular projection are half-micron apart from each other. These equivalent points are marked with arrows. Thus the origin of the large period of ~0.5 μm after the etching can be explained.

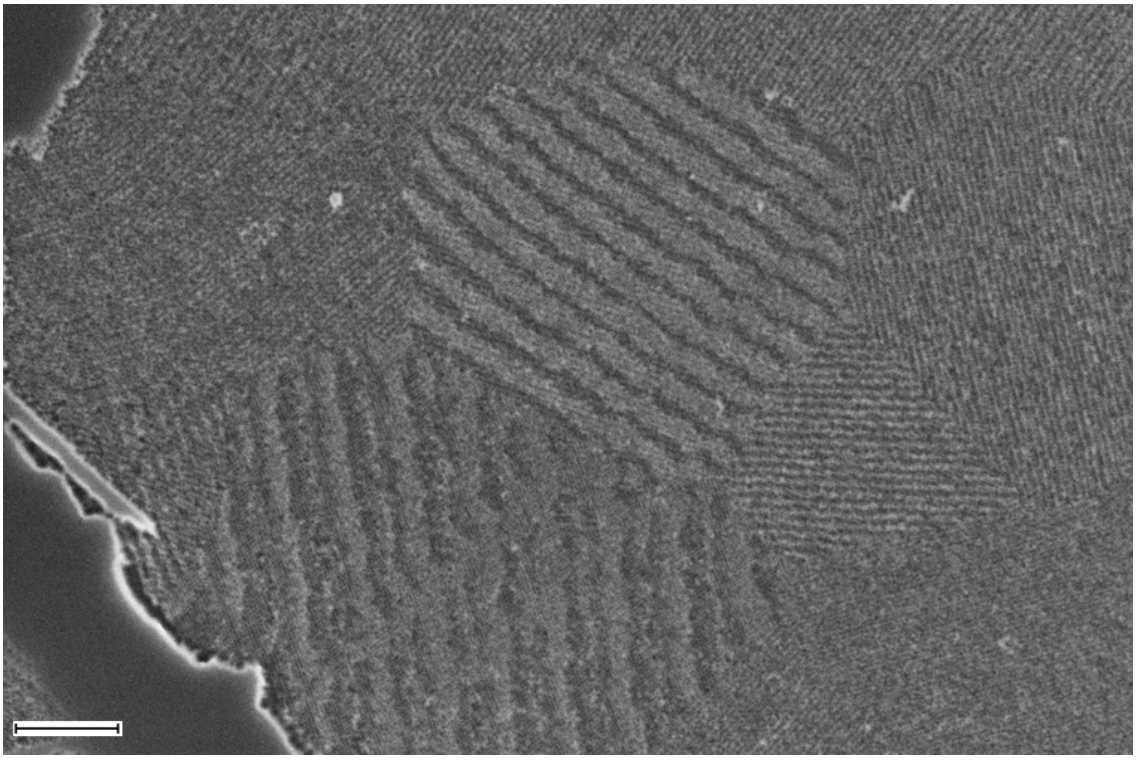

Fig. 5.2.3. Grains footprints after long isotropic etching (6 s O_2/Ar + 32 s isotropic silicon etch). 1 μm scale bar.

Fig. 5.2.4. Possible cross-section of a ~40 nm thick GYR mask. Arrows mark repeating elements, which originate the large wavy patterns in fig. 5.2.3. 200 nm scale bar.

The biggest problem with the gyroid morphology is that etching cannot be perfect even for a single small grain. Some unstable periodic patterns transferred from gyroid are shown in fig. 5.2.5. They are: straight lines of merging holes, a honeycomb structure and a wavy structure. Patterns look non uniform: holes merge in some regions and do not in others. 0.5-1 nm roughness of the mask is enough to produce this non-uniformity. Longer time black silicon etching quickly destroys the patterns. This makes these structures too difficult to capture and reproduce.

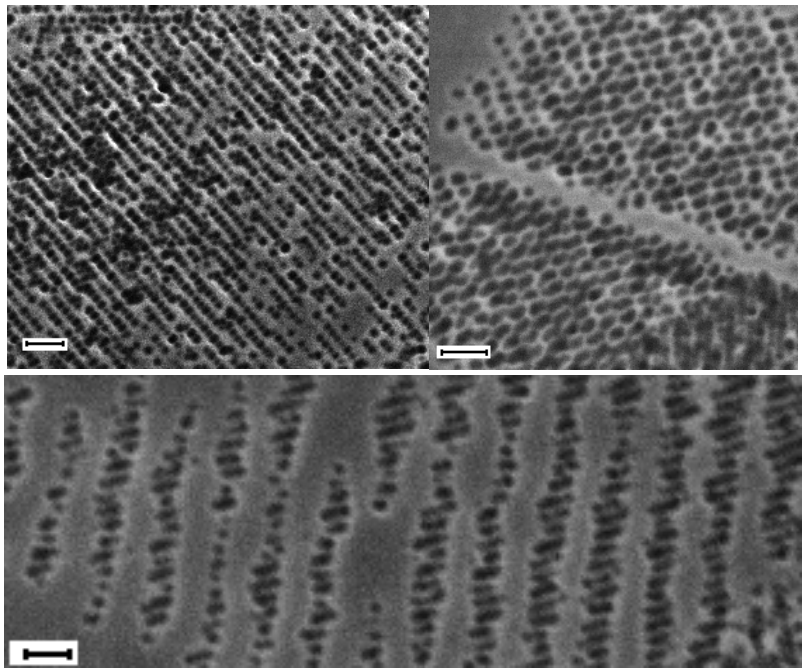

Fig. 5.2.5. Unstable patterns on silicon from a gyroid mask. Etching is difficult to optimize even for one grain: some parts are more etched than others. 200nm scale bars. (10 s O_2/Ar + 15 s black silicon etch)

SEM images of stable patterns are shown in fig. 5.2.6. For isotropic silicon etching a HEX hole pattern (36 nm period from FFT) is superimposed with a larger period of wavy pattern. Isotropic etch slowly destroys the pattern and can tolerate over-etching. Thus all holes can be transferred, since holes etched earlier do not become destroyed by over-etching. Time of over-etching affects the amplitude of the waves of the larger pattern. For black silicon etching, over-etching quickly destroys the patterns. Metastable structures were obtained on the border conditions, where some parts are slightly underetched, some are slightly overetched. The stable pattern for black silicon etching is an underetched one. The pattern is formed after a short etch through a very thin mask. In this case the structure looks chaotic, because only a fraction of the holes is transferred, but FFT reveals the presence of a hexagonal structure and of parallel lines.

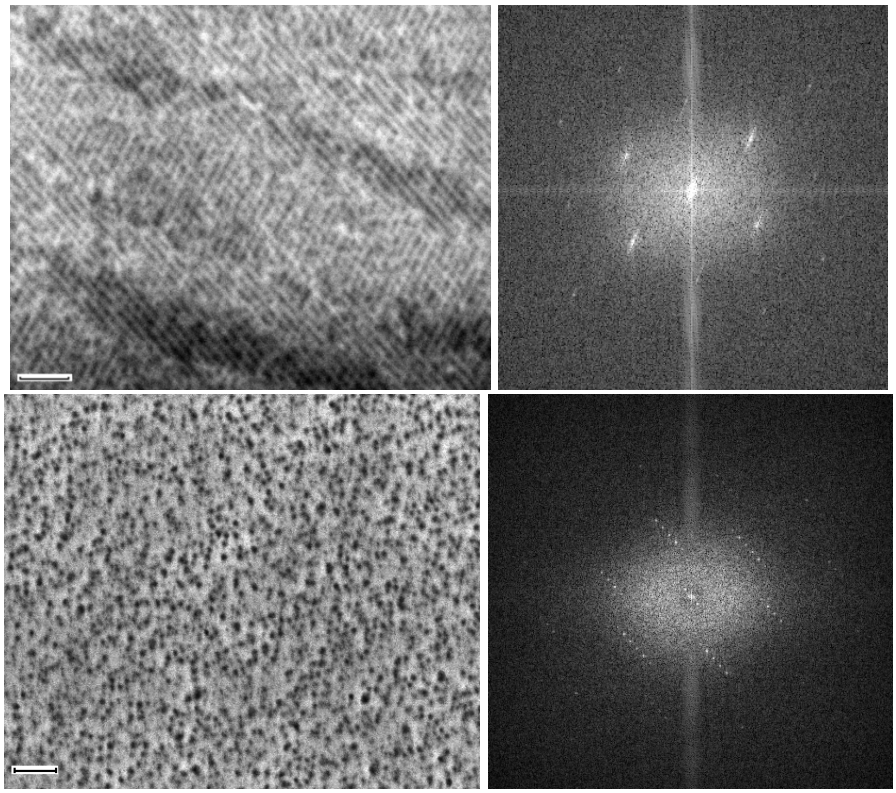

Fig. 5.2.6. Stable patterns on isotropically (top) and anisotropically (bottom) etched silicon with the respective FFT. Patterns are obtained by 6s O_2/Ar + 32 s isotropic silicon etch and 30 s O_2/Ar + 9 s black silicon etch. The presence of HEX pattern is clear from FFT for both patterns. 200 nm scale bars.

5.3. Lamellar morphology

Few experiments are performed to investigate the suitability of lamellar morphology from PB-b-PDMS for microtome mask preparation. Microtoming of lamellar block copolymers can give lined masks with tunable period. If the polymer monolith is sliced perpendicular to the lamellae planes, masks with minimal period will be obtained. By changing the cutting angle, the period of the structure can be increased. The problem with lamellar polymer is its instability after etching. The fraction of PDMS is very high and shear aligned lamellar bulk samples collapse after the PMDS etch. Possibly if the aligned domains are smaller, then the layers could be stabilized by domain borders.

Lamellar polymer BD8, with a weight ratio PB:PDMS of 51.5:48.5 and a total molecular mass of 15500 g/mol was used in the experiments. Monoliths with two different alignment degrees

were prepared: either unaligned or aligned by only one forth and back cycle of the shearing glasses. One piece from each monolith was etched by TBAF in THF for 72 hours. After etching the samples were washed with THF and ethanol in order to remove TBAF and etching products. Optical images of the unaligned sample are shown in fig. 5.3.1. The block copolymer pieces are soft and semitransparent. The etched sample shrank and became white and rigid. The thickness of the original sample measured with the calipers was ~0.95 mm, but after etching it became ~0.65 mm.

Fig. 5.3.1. Photographs of unaligned lamellar samples before and after the wet etching.

All 4 samples were microtomed. During slicing, sections of both etched and unecthed samples were unstable for thicknesses smaller than ~200 nm. Sections thinner than 200 nm disintegrated during slicing into many tiny pieces. An example of a section close to disintegrating is shown in fig. 5.3.2. This is a section of unaligned unetched sample. Small parts of the section at its edges are falling off. Disintegration happens for both etched and unetched samples. That means that at that scale non cross-linked PDMS holds the structure together only slightly better than nothing.

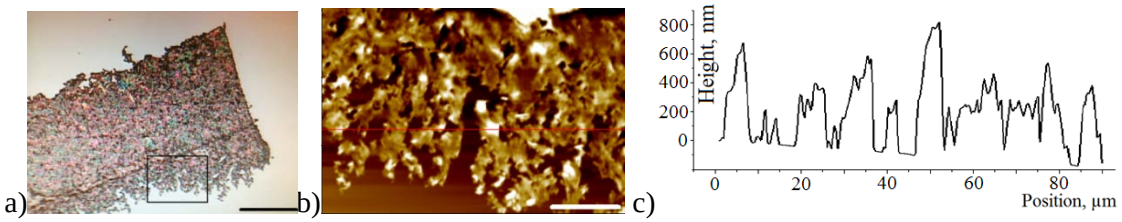

Fig. 5.3.2. a) Optical image of a lamellar unaligned and unetched BCP section. The AFM image in (b) is taken from the highlighted part in (a), topographical profile in (c) is taken along the red line. Scale bars are 100 µm for the optical image and 20 µm for the AFM image.

SEM images of small polymer pieces from etched samples are shown in fig. 5.3.3. Sizes of these pieces are few microns. Structures of collapsed lamellae, unevenly stuck together were observed (fig. 5.3.3 a). Although it was expected that domain borders could hold lamellae together, this actually did not work and small single-lamellar pieces exfoliated and lying separately on the surface (fig. 5.3.3 b). Lined nanostructure can be found in some places (fig. 5.3.3 c) shrank to period of 14 nm.

a) 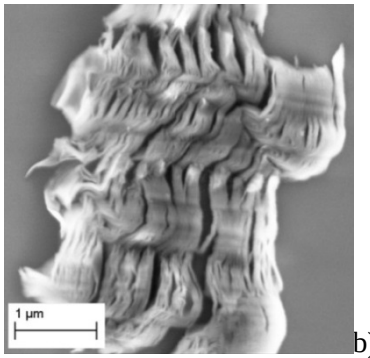

b) 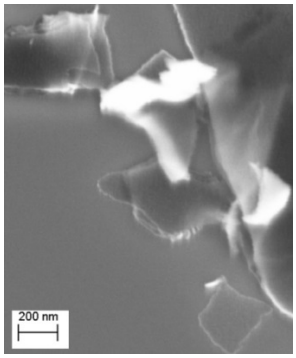

c) 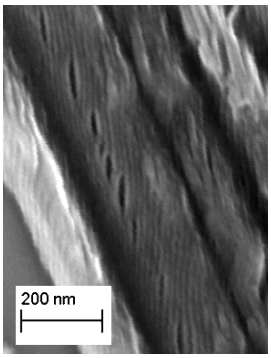

Fig. 5.3.3. SEM images of etched unaligned lamellar samples. a) Collapsed lamellae; b) separate exfoliated lamellae; c) collapsed nanostructure with a period of ~14 nm.

5.4. Summary

We have proved that pattern can be transferred to silicon substrate from microtomed masks. Polymers with hexagonal morphology in the bulk can be aligned by shear and provide masks with crystalline order on hundreds of micron scale. Masks cut off at 90° relative to the cylinder axis consist of pattern of hexagonally packed round holes. Highly ordered nanomesh was transferred from such masks to silicon. In the case of two superimposed masks moiré patterns were transferred for the first time. By cutting at 45° relative to the cylinder axis slit-like patterns were transferred to silicon. Low quality line patterns were transferred to silicon from masks cut parallel to the cylinder axis.

For polymer monoliths of gyroid morphology the typical size of grains with the same structure orientation was ~ 2 µm. It was not possible to optimize etching conditions that could allow pattern transfer from the whole gyroid mask. Low-quality hexagonal patterns were transferred to silicon.

Lithography masks cannot be prepared from lamellar polymer by microtoming. Sections thinner than 200 nm disintegrate during slicing.

6. Graphene superlattices

After the HEX pattern was successfully transferred to silicon, time come to nanostructure graphene and measure the effect of nanostructuring on graphene's electrical properties. For electrical measurements the back-gate devices were fabricated by clean deposition of stencil contacts on top of nanostructured graphene flakes.

6.1. Patterning and mask removal procedure

The procedure for the graphene nanopatterning is essentially the same as the one applied for silicon nanopatterning. The nanoporous masks were cut off the same nanoporous monolith. The main difference is in the mask removal procedure. Now mask removal by oxygen plasma is not applicable, because it would remove the mask together with the graphene. An alternative tape method was used instead: the whole sample is covered with a tape, which is pressed onto the surface and then slowly pulled off together with the polymer mask. Seemingly graphene is more strongly attached to the substrate than to the mask, and the nanostructured graphene flake remains on the substrate.

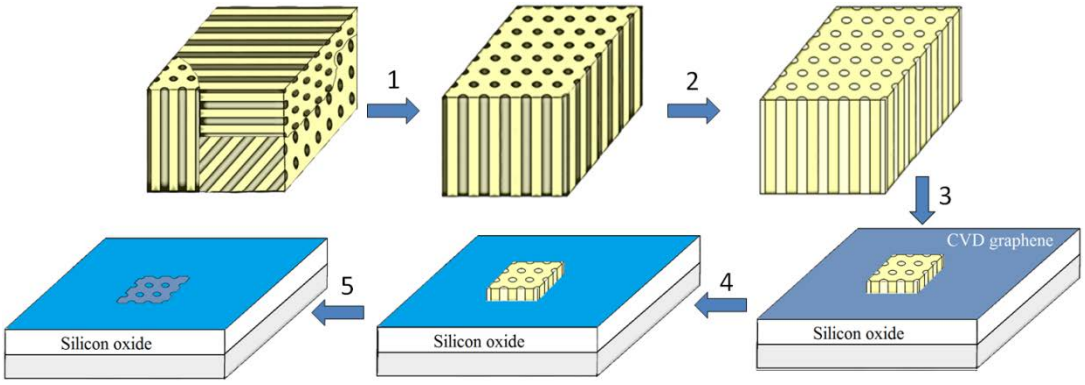

Figure 6.1.1. Work-flow of the nanolithographic process for graphene nanostructuring. (1) 1,2-PB-*b*-PDMS with random domain orientation is shear-aligned and cross-linked to fix the structure. (2) PDMS is selectively etched to get nPB. (3) The nPB monolith is microtomed at room temperature. Sections are transferred onto a wafer fully covered with CVD graphene. (4) Graphene etching by RIE, which transfers the pattern to the graphene under the mask and uniformly etches the graphene outside of the mask. (5) Mask removal by a tape.

6.2. Graphene nanomesh

The highest-quality graphene is still obtained by mechanical exfoliation. This method, also called adhesive tape method, consists of repeating peeling of small mesas of highly oriented pyrolytic graphite. The method is very time-consuming and the resulting single-layer graphene flakes are commonly only ~10-30 μm in sizes. Because addressability of microtomed masks deposition is still poor, a substrate fully covered with graphene is desirable. In this case all deposited masks will have graphene underneath. Commercial single-layer wafer-scale graphene obtained by chemical vapor deposition (CVD) was used [102]. CVD graphene films have polycrystalline structure and bilayer regions. Compared to mechanically exfoliated graphene, the mobility of charge carriers in CVD graphene is lower, impurity doping is greater and it exhibits higher asymmetry between electron and hole conduction [103].

A wafer fully covered with CVD graphene was ordered from the Spanish company Grahenea. The wafer has a 300 nm thick silicon oxide layer necessary to make graphene clearly visible on silicon [104]. The presence of oxide layer renders the silicon wafer purple-blue (fig. 6.2.1 a, b) and the color of the polymer masks is determined by the sum of OPD in the two layers: mask and oxide. Now the colors of the polymer masks pass through blue-green-yellow for thicknesses in the range of 40-100 nm, instead of beige-purple-blue for masks deposited on wafers with 2 nm oxide layer.

An optical image of polymer mask deposited on graphene is shown in fig. 6.2.1 a. The mask has an approximate size of 300x100 μm^2, within which smooth wrinkle-free regions of sizes ~50x50 μm^2 can be found. After one-step etching with highly-anisotropic oxygen/argon plasma the mask was removed by tape and graphene is clearly visible on the substrate as a dark flake with the shape of the original mask (fig 6.2.1 b). Some parts of the mask could not be stripped (green and yellow colors in fig. 6.2.1 b), and changed color because of attached tape residues. The tape also contaminated the area around the mask: the optical image shows appearance of blue patches in the bottom-left corner. At this stage graphene can be inspected by common characterization methods like SEM and AFM.

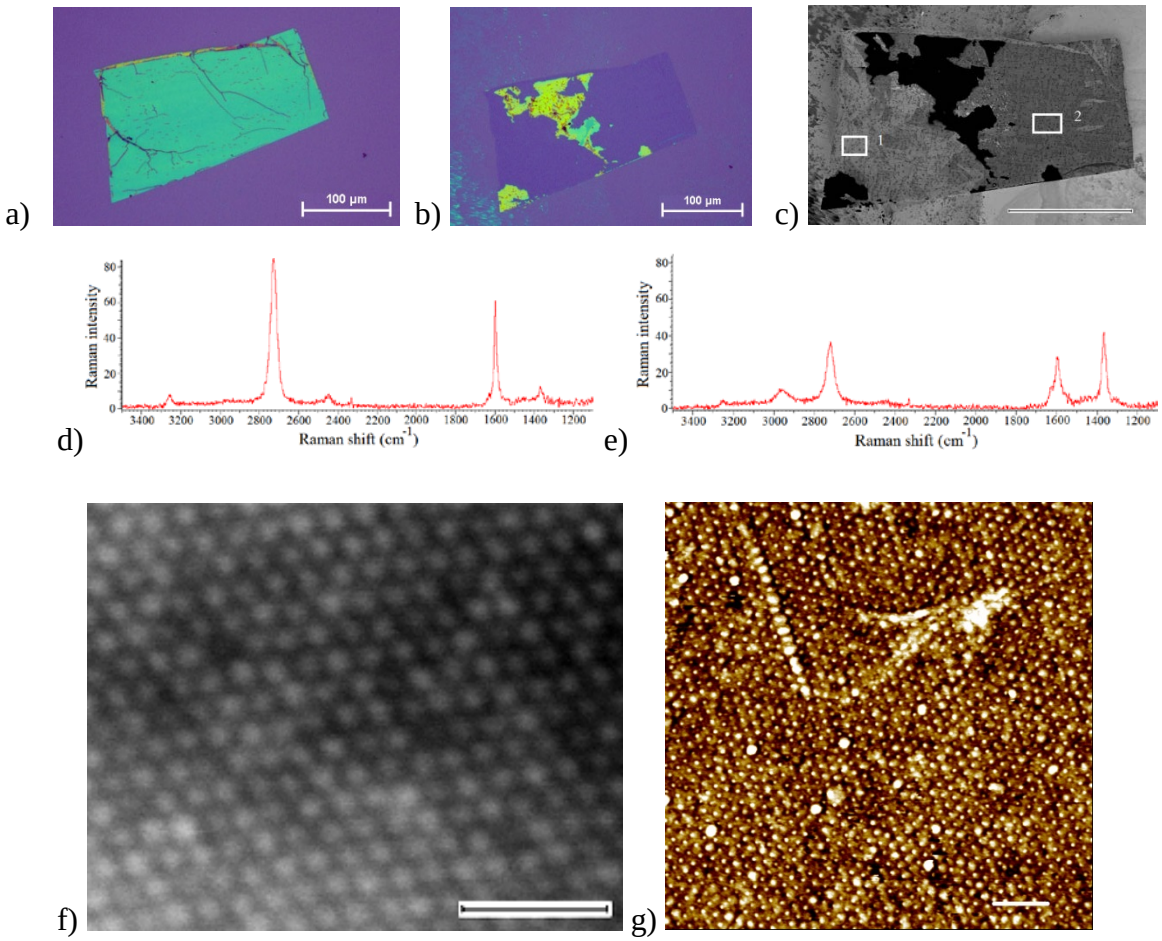

Fig. 6.2.1. Images of nPB flake on graphene. a) Optical image of nPB mask on graphene; b) optical image of graphene flake after the etching and mask removal by tape; c) SEM image of graphene flake; Scale bars 100 µm; Raman spectra in box 1 (d) and box 2 (e), f) High-resolution graphene nanomesh in SEM and g) AFM image. (f-g) have 100 nm scale bars;

The low-resolution SEM image shows (fig.6.2.1 c) a detailed map of patterning of the graphene flake. Patches of remaining polymer mask are black in SEM. The exposed graphene has two colors: light gray as in box 1, and dark grey as in box 2. Nanostructured graphene was observed by SEM in the darker graphene regions. In the lighter grey regions no nanopatterns were detected by SEM. Raman spectra of the light and dark are shown in fig. 6.2.1. (d-e) respectively. The defect D peak at ~1350 cm^{-1} is significant only for the dark areas. This finding is plausible since the light areas were covered by wrinkled portions of the mask, which hinder pattern transfer. High-resolution SEM (fig. 6.2.1. f) shows a nanomesh with period of 20 nm and all holes of equal size of ~14 nm. Imaging by AFM shown in fig. 6.2.1 g confirms the

formation of a regular hexagonal graphene nanomesh. The period of the hexagonal structure in fig. 6.2.1 f,g coincides with that of the original nanoporous mask.

A back-gated device was fabricated for electrical measurements. After sample annealing in order to remove as much of remaining contaminants as possible, stencil contacts (2/50nm Cr/Au) were deposited on top of the graphene flake (fig. 6.2.2. a). A Raman map of the patterned part of the flake (map taken in the red box and dots shown in fig. 6.2.2.a) shows an increased D peak (fig. 6.2.2. b) and a decreased 2D to G intensity ratio (fig. 6.2.2. c) due to nanopatterning. Silver paint was used to create larger contacts for graphene resistance measurements. The device conductance vs. gate bias was measured at different temperatures as shown in fig. 6.2.2 d. The temperature dependence of the resistance can show whether charge carriers in graphene are hopping between subgap impurity states or whether they are thermally excited between valence and conduction bands over the energy gap Δ. In hopping regime the temperature dependence of conductivity in 2D systems is described by [105]:

$\sigma = \sigma_0 e^{-(\frac{T_0}{T})^n}$, where

n=1 for nearest neighbor hopping;

n=1/3 for two-dimensional Mott variable range hopping;

n= ½ for Efros Shklovskii variable range hopping in the presence of Coulomb interaction between localized states;

T_0 is the activation energy of hopping.

Then

$log\,\sigma = log\,\sigma_0 - (\frac{T_0}{T})^n$;

Thermally activated electrical current in intrinsic semiconductors is described by

$\sigma = \sigma_0 e^{-\frac{\Delta}{2kT}}$

That can be transformed to:

$log\,\sigma = log\sigma_0 - \frac{\Delta}{2kT}$

If log of conductance depends linearly on (1/T), then Δ is the only fitting parameter for the slope; Δ is in such case an indication of what could be an energy gap. The results of measurements from our sample are shown in fig. 6.2.2 e. The logarithm of the conductance is linearly dependent on 1/T with a strong correlation (coefficient $R^2 = 0.996$). Therefor the nanostructured graphene can be considered as a thermally activated intrinsic semiconductor with a ~20 meV bandgap.

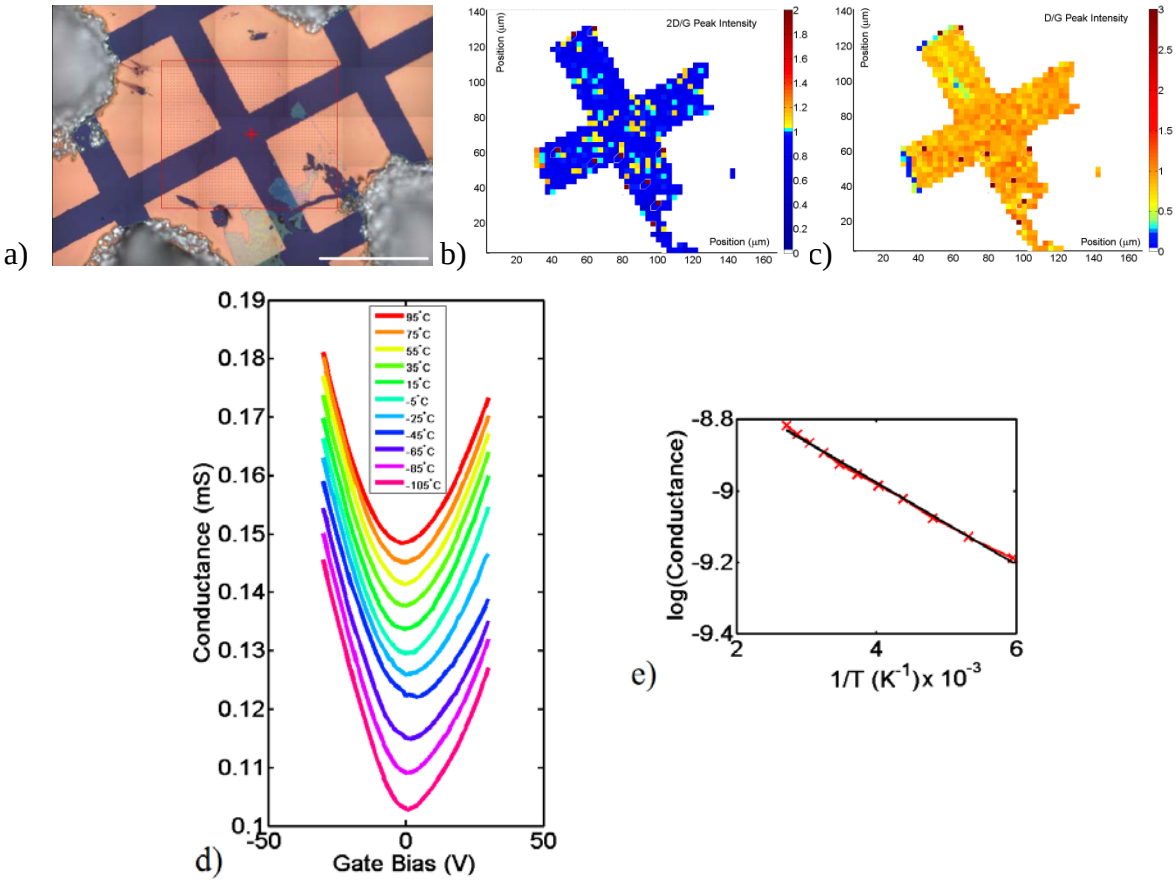

Fig. 6.2.2. a) Optical microscope image of graphene flake with stencil contacts; Red box indicates the place where Raman map was taken; (b-c) Raman map of graphene device for 2D/G and D/G intensity ratios; d) measured conductance vs. gate voltage plot at different temperatures and e) extracted bandgap. Red crosses- experimental data, black line is the 1st order linear fitting of the data.

However, the temperature-dependent conductance of nanoconstricted graphene is more complex than that of an intrinsic semiconductor. Multiple phenomena were studied both theoretically and experimentally to evaluate their influence on the electrical transport in

graphene nanoribbons and nanomeshes, comprising Anderson localization due to edge disorder [106], density inhomogeneity driven percolation transition [107] and Coulomb blockage [108]. Edge disorder causes formation of “necks” (fig. 6.2.3.), where the number of conducting channels is smaller than in the “dots”, leading to electrical isolation of dots and confinement of electrons in the dots. Similar role can be played by any imperfections on the silicon-graphene interface. Close to CNP, this disorder-induced confinement leads to formation of “puddles” of electrons or holes and the electric transport in graphene nanoribbons is dominated by a chain of disorder-induced quantum dots with cotunneling between conductance resonances at low temperatures and activated transport at higher temperatures [109].

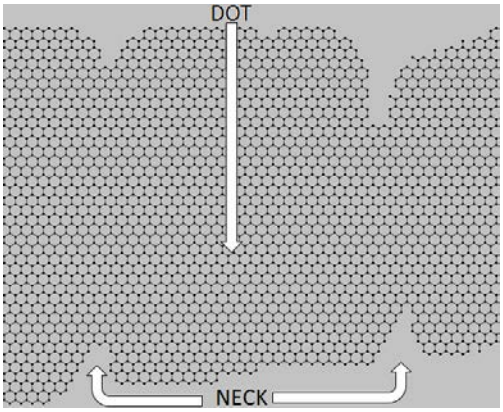

Fig. 6.2.3. Illustration of formation of dots and necks in a graphene nanoribbon due to edge disorder.

In order to understand the type of mechanisms contributing in formation of the measured 20 meV gap in our graphene nanomesh, additional meticulous experimental characterization is required.

6.3. Graphene on pillars

Another way to open bandgap, as was mentioned in the introduction, is to create strain superlattices of graphene. For this purpose CVD graphene was transferred on top of a dense array of nanopillars.

Dense arrays of pillars were prepared from the BCP microtomed sections. The same PB-b-PDMS monolith was not etched prior to slicing and sections deposited on the silicon wafer contained both blocks. Then instead of etching PMDS, a mild oxygen plasma treatment was

performed. It removes PB and oxidizes PDMS into hard PDMS-oxide. As a result, smooth polymer sections were transformed into arrays of cylinders of ox-PDMS.

Trivial Transfer Graphene (TTG) was ordered from http://acsmaterial.com. In the box (fig. 6.3.1) ca. 1x1 cm^2 square graphene piece is lying on a soft fabric support. Graphene has a thin layer of PMMA on top. With the help of tweezers and a sharp knife small pieces (~3 mm x 3 mm) can be teared off the large square.

a) 

b) 

Fig. 6.3.1. Commerscally available TTG sample. a) box; b) sample of graphene inside.

A small graphene piece covered with a PMMA layer, adhering to the knife was carefully brought in contact with a water droplet on the desired substrate, the array of nanopillars. The graphene flake was much larger than the size of individual BCP sections, so one graphene piece could cover completely several nanopillar arrays and the surrounding silicon wafer.

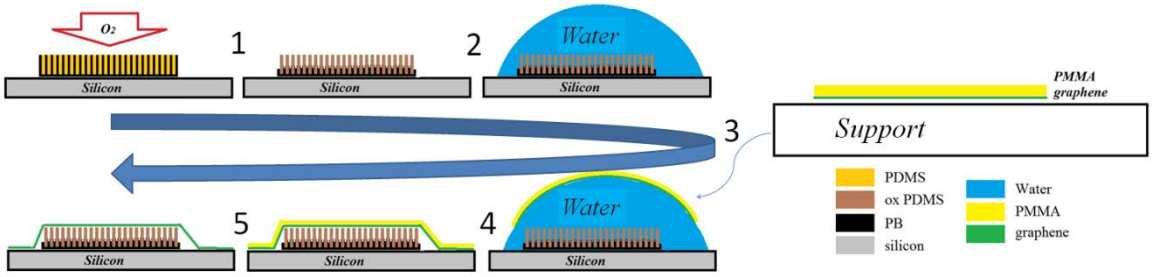

Fig. 6.3.2. Deposition of TTG on a nanopillar array: (1) Microtomed PB-b-PDMS exposed to oxygen plasma for PB etch; (2) Water droplet put on top of the sample; (3) TTG piece transferred with a pair of tweezers on top of the water droplet. (4) Water is partly soaked by a tissue paper followed by baking for 30 min at 90°C; (5) Sample is immersed in acetone, 2 times for 5 min to dissolve PMMA.

Nanopillar arrays were fabricated on top of a silicon wafer with thin (2 nm) natural oxide layer. Then TTG was deposited on top of the array completely covering it. Graphene is poorly visible

in optical microscope (fig. 6.3.3 a) and only black dots of undissolved PMMA contamination allow to recognize the part of substrate covered with graphene.

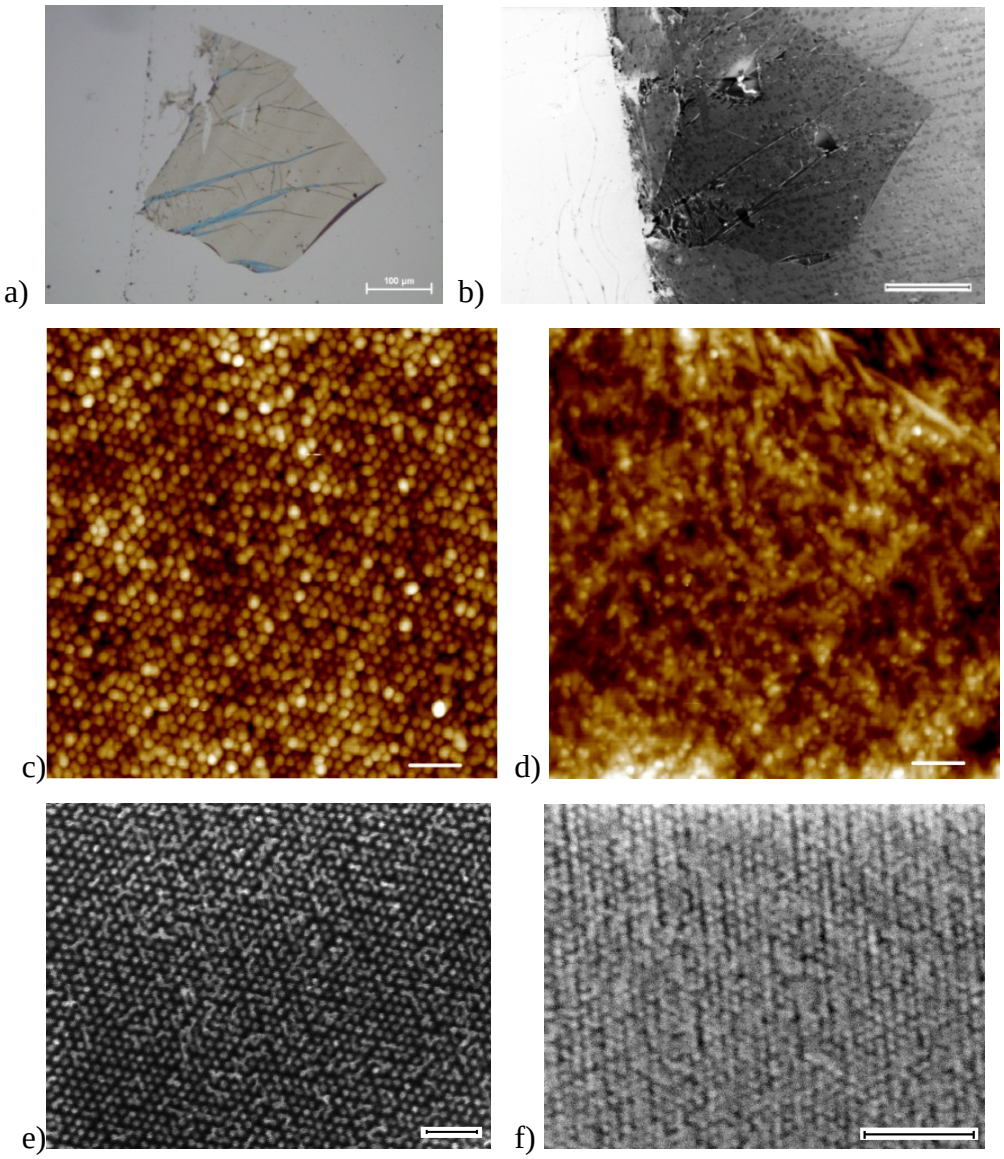

Fig. 6.3.3. a) Optical image of graphene covering BCP nanopillar array; b) SEM image of the same nanopillar array covered with graphene, (a-b) Scale bars are 100 µm; c) AFM image of the nanopillars and d) nanopillars covered with graphene; e) SEM image of nanopillars and f) nanopillars seen through graphene in SEM, (c-f) 100 nm scale bars.

In SEM (fig 6.3.3 b) the graphene sheet is clearly visible. To study how graphene is deformed by the pillars underneath both AFM (fig 6.3.3. c and d) and SEM (fig 6.3.3. e and f) measurements of the bare pillar array (c, e) and pillar array covered with graphene (d, f) were

performed. Bare nanopillars are clearly distinguishable in both AFM and SEM. After graphene deposition pillars are visible through graphene in SEM. However, the AFM topography image does not show the original pillar period. This indicates that graphene is lying mostly flat and does not confirm the nanopillar topography. In the top right corner of the AFM image small wrinkles are visible. The PMMA layer supporting graphene was very thin and flexible. During the deposition it formed multiple ripples and wrinkles, leading to ripples and wrinkles on the deposited graphene. Graphene deposited on a flat silicon surface (fig. 6.3.4) is also not flat, again forming many wrinkles; white clusters of remaining undissolved PMMA are also visible in the image.

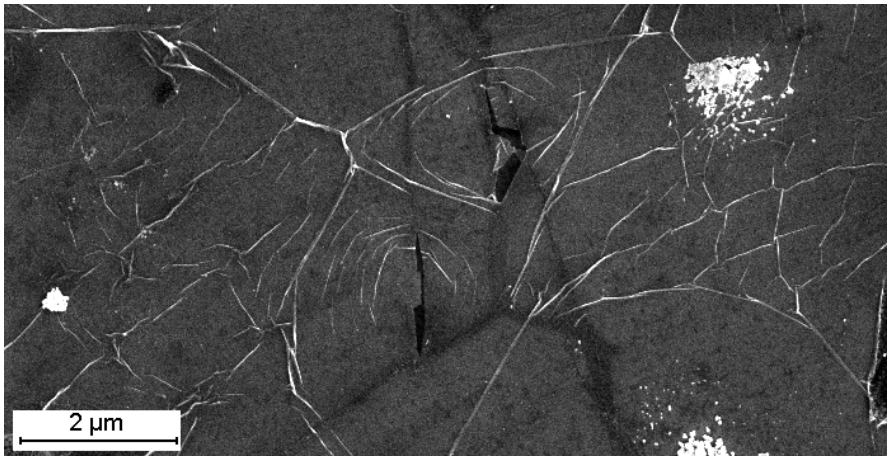

Fig. 6.3.4. SEM image of graphene on flat silicon substrate. 2µm scale bar.

The results can be compared with results from [110]. In this work *Reserbat-Plantey et al*. deposited graphene on top of silica pillar arrays with variable geometries. They have shown that if the distance between the pillars is similar to the pillars height, graphene will collapse and ripple. In this work, dense pillar arrays are covered by suspended graphene. This corresponds to our case, but the pitch of our structure is 20 times smaller and small ripples affect the resulting graphene topography more than the pillars underneath.

Deposition of TTG onto silicon increases r.m.s. roughness of the surface from 0,4 nm to 2,5 nm. The r.m.s. variation in pillars top's heights is directly linked with the r.m.s roughness of the polymer section (has value of 0,9 nm). That indicates that contribution of graphene wrinkles and ripples to the imperfect contact between TTG and pillars tops is much larger than contribution of the pillars tops position variation. Wrinkles on graphene have widths exceed 40 nm (2 periods of pillar array) and lengths of a hundreds nanometers. Graphene stiffness is also wrinkle-dependent [111] and on the scale smaller than the wrinkle size cannot be determined.

In conclusion, “Trivial Transfer Graphene” was deposited on top of prepared from PB-b-PDMS pillar arrays. Ripples and wrinkles formed during deposition make a larger contribution to graphene morphology than the interaction with the nanostructured substrate. Improvements of the graphene deposition process are required to deposit graphene flatter.

6.4. Summary

Graphene nanomesh of 20 nm period and ~14 nm size holes was successfully fabricated by one-step etching through *ex-situ* prepared nanoporous masks. The nanomesh is highly ordered and with all holes of the same size. The mask can be removed by applying an adhesive tape. Electrical measurements indicate the presence of an effective gap of 20 meV. Trivial Transfer graphene was suspended on top of nanopillar arrays, but its topography was mostly affected by wrinkles formed during deposition than by substrate underneath. Improvements of the transfer procedure are required in order to make graphene lay flatter.

7. Conclusions and outlook

During the PhD study several approaches utilizing self-organizing properties of block copolymers were tested for graphene bandgap engineering. Firstly, perspectives of mask fabrication from lamellar polymer by wet etching were studied. By this method masks with sizes up to 20 μm were proved to be possible to fabricate.

Conventional block copolymer lithography was tried for creation of a wafer-scale nanomesh on graphene. Unfortunately, the procedure reported in high-impact journal, which we followed, known from the literature was not robust enough for quick reproduction, or eventually after minor optimization. The resulting polymer mask had mixed morphology of cylinders oriented perpendicular and parallel relative to the substrate. Pattern transferred to the silicon substrate consisted of deep round holes etched under the “standing” cylinders and short shallow lines etched under the “lying” cylinders. In the best case we were able to create PS-b-PMMA mask with ~80% of standing cylinders.

The main achievement of the current PhD work is the development of a new microtome-based method for nanolithography. The concept was proved by transferring of the pattern to silicon. The main advantage of the method is high crystallinity of the pattern due to effectiveness of aligning of the bulk polymer by mechanical shear. Unidirectional orientation of cylinders with hundreds of microns domain sizes can be obtained by shearing. Numerous patterns were transferred to silicon from the masks fabricated by microtoming of porous monoliths with hexagonally packed cylinder morphology. Hexagonal pattern was transferred from masks cut off perpendicular relative to the cylinder axis. Superimposition of two masks allowed to realize the first transfer of moirè patterns to silicon. Slit-like patterns were transferred from masks obtained by cutting at 45° relative to the cylinder axis. Cutting parallel to the cylinder axis gives multilayer masks that do not provide sufficient etching contrast for clear line pattern fabrication. Etching through masks cut off nanoporous monoliths with gyroid morphology lead to formation of dual hexagonal and lined patterns on a silicon substrate. Patterns had low contrast due to the necessity to etch through the mask material. In addition, gyroid monolith consists of grains with different structure orientations, which makes it impossible to optimize etching condition for the whole mask. Monolith with lamellar morphology disintegrated during slicing and could not be used as lithography mask.

The key advantage of *ex-situ* mask fabrication is the possibility to apply the mask on any surface. *Ex-situ* fabricated hexagonal masks were successfully applied for graphene nanopatterning. The masks could be peeled off after the pattern transfer. Graphene nanomesh with 20 nm period was fabricated by simple one-step oxygen/argon plasma etching. Electrical measurements showed a 20 meV gap opening in the graphene. Block copolymer sections can be used for fabrication of dense arrays of hard oxidized PDMS nanopillars. However, the topography of graphene deposited on top of these arrays is more affected by the deposition method, rather than from the interaction with the pillar tops, and does not indicate presence of periodical strain.

Microtome mask fabrication can be improved in many aspects. Mask deposition on the substrate is poorly controlled. After the deposition masks form wrinkles, which limits the area useful for pattern transfer.

More experiments for graphene nanostructuring can be performed. Other etching recipes can be tried. By varying etching time, nanomesh neck width can be tuned. The dependence of a gap value from the neck width can be studied. Experiments can be repeated on mechanically exfoliated graphene. In order to eliminate contaminations, nanopatterning of bilayer graphene can be tried. In this case mask will be peeled off together with the top graphene layer, and single layer of extremely clean nanopatterned graphene will remain on the substrate. Microtomed based method opens up wide perspectives for nanopatterning of other 2D materials, like hexagonal boron nitride or molybdenum disulfide.

References:

1. Schwierz, F. Graphene transistors. *Nat. Nanotechnol.*, **2010**, vol. 5, 487-496.

2. Novoselov, K. S.; Geim, A. K.; Morozov, S. V.; Jiang, D.; Zhang, Y.; Dubonos, S. V.; Gregorieva, I. V.; Firsov, A. A. Electric Field Effect in Atomically Thin Carbon Films. *Science*, **2004**, Vol. 306, no. 5696, 666-669.

3. Stoller, M.D.; Park, S.; Zhu, Y.; An, J.; Ruoff, R.S. Graphene-based ultracapacitors. *Nano Letters*, **2008**, 8 (10), 34983502.

4. Lee, C.; Wei, X.; Kysar, J.W.; Hone, J. Measurement of the Elastic Properties and Intrinsic Strength of Monolayer Graphene. *Science*, **2008**, 321 (5887), 385-388.

5. Frank, I. W.; Tanenbaum, D. M.; van der Zande, A. M.; McEuen, P. L. Mechanical properties of suspended graphene sheets. *J. Vac. Sci. Technol. B*, **2007**, 25 (6), 2558-2561.

6. Bolotin, K. I.; Sikes, K. J.; Jiang, Z.; Klima, M.; Fudenberg, G.; Hone, J.; Kim, P.; Stormer, H. L. Ultrahigh electron mobility in suspended graphene. *Solid State Commun.*, **2008**, 146 (9-10), 351–355.

7. Wallace, P. R. The Band Theory of Graphite. *Phys. Rev.*, **1947**, 71, 622.

8. Bostwick, A.; Ohta, T.; Seyller T.; Horn K.; Rotenberg, E. Quasiparticle dynamics in graphene. *Nature Phys.*, **2007**, 3, 36 - 40.

9. Castro Neto, A. H.; Guinea, F.; Peres, N. M. R.; Novoselov, K. S.; Geim, A. K. The electronic properties of graphene. *Rev. Mod. Phys.*, **2009**, vol. 81, 109-162.

10. Kedzierski, J.; Pei-Lan Hsu; Healey, P.; Wyatt, P.W.; Keast, C.L.; Sprinkle, M.; Berger, C.; de Heer, Walt A. Epitaxial graphene transistors on SiC substrates. *IEEE Trans. Electron. Dev.*, **2008**, 55**,** 2078–2085.

11. Kedzierski, J.; Hsu P-L; Reina, A.; Kong, J.; Healey, P.; Wyatt, P.; Keast, C. Graphene-on-insulator transistors made using C on Ni chemical-vapor deposition. *IEEE Electron Dev. Lett.*, **2009**, 30**,** 745–747.

12. Park, C. H.; Yang, L.; Son, Y. W.; Cohen, M. L.; Louie, S. G. Anisotropic behaviours of massless Dirac fermions in graphene under periodic potentials. *Nature Phys.*, **2008**, *4* (3), 213–217.

13. Balog, R.; Jørgensen, B.; Nilsson, L.; Andersen, M.; Rienks, E.; Bianchi, M.; Fanetti, M.; Lægsgaard, E.; Baraldi, A.; Lizzit, S.; Sljivancanin, Z.; Besenbache, F.; Hammer, B.; Pedersen, T.G.; Hofmann, P.; Hornekær, L. Bandgap opening in graphene induced by patterned hydrogen adsorption. *Nat. Mater.*, **2010**, vol. 9, 315-319.

14. Vázquez de Parga, A. L. V.; Calleja, F.; Borca, B.; Passeggi, M. C. G.; Hinarejos, J. J.; Guinea, F.; Miranda, R. Periodically Rippled Graphene: Growth and Spatially Resolved Electronic Structure. *Phys. Rev. Lett.*, **2008**, 056807 (4).

15. Raza, H. Zigzag graphene nanoribbons: bandgap and midgap state modulation. *J. Phys.: Condens. Matter.*, **2011**, 23-382203, (5pp).

16. Barone, V.; Hod, O.; Scuseria G. E. Electronic Structure and Stability of Semiconducting Graphene Nanoribbons. *Nano Letters*, **2006**, 6 (12), 2748-2754.

17. Hung Nguyen, V.; Chung Nguyen, M.; Viet Nguyen H.; Dollfus, P. Disorder effects on energy bandgap and electronic transport in graphene-nanomesh-based structures. *J. Appl. Phys*., **2013**, 113, 013702.

18. Power, S. R.; Antti-Pekka Jauho. Electronic transport in disordered graphene antidot lattice devices. *Phys. Rev. B*, **2014**, 90, 115408.

19. Whitesides, G. M.; Grzybowski, B. Self-Assembly at All Scales. *Science,* **2002**, *295,* 2418-2421.

20. Strobl**,** Gert R. The Physics of Polymers Concepts for Understanding Their Structures and Behavior. *Springer,* **1996**.

21. Castelletto, V.; Hamley, I.W. Morphologies of block copolymer melts. *Curr. Opin. Solis State Mater. Sci.*, **2004**, 8, 426–438.

22. Bates, F. S.; Fredrickson, G. H. Block Copolymer Thermodynamics: Theory and ExExperiment. *Annu. Rev. Phys. Chem.*, **1990**, 41, 525-557.

23. Matsen, M. W.; Bates, F. S**.** Unifying Weak- and Strong-Segregation Block Copolymer T Theories. *Macromol.*, **1996**, 29 (4)), 1091-1098.

24. Chremos, A.; Nikoubashman, A.; Panagiotopoulos, A. Z. Flory-Huggins parameter χ, from binary mixtures of Lennard-Jones particles to block copolymer melts. *The Journal of Chem. Phys*., **2014**, 140, 054909.

25. Semenov, A. N. Contribution to the theory of microphase layering in block-copolymer melts. *Sov. Phys. JETP*, **1985**, 61 (4), 733-742.

26. Listak, J.; Jakubowski, W.; Mueller, L.; Plichta, A.; Matyjaszewski, K.; Bockstaller, M. R. Effect of Symmetry of Molecular Weight Distribution in Block Copolymers on Formation of "Metastable" Morphologies. *Macromol.,* **2008**, Vol. 41, no. 15, 5919–5927.

27. Matsen, M. W. Polydispersity-Induced Macrophase Separation in Diblock Copolymer Melts. *Phys. ReV. Lett.*, **2007**, *99* (148304), 1–4.

28. Hadziioannou, G.; Mathis, A.; Skoulios, A. Obtention de "monocristaux" de copolymères triséquencés styrène/isoprène/styrène par cisaillement plan. *Colloid & Polymer Sci*., **1979**, 257, 136-139.

29. Keller, **A.;** Pedemonte, E.; Willmouth, F. M. Macro-lattice from Segregated Amorphous Phases of a Three Block Copolymers. *Nature,* **1970,** *225***,** 538-539.

30. Tepe, T.; Schulz, M. F.; Zhao, J.; Tirrell, M.; Bates, F. S.; Mortensen, K.; Almdal, K. Variable Shear-Induced Orientation of a Diblock Copolymer Hexagonal Phase. *Macromol.,* **1995,** *28***,** 3008-3011.

31. Li, W.; Liu, M.; Qiu, F.; Shi, An-C. Phase Diagram of Diblock Copolymers Confined in Thin Films. *J. Phys. Chem. B*, **2013**, 117 (17), 5280-5288.

32. Nikoubashman, A.; Register, R. A.; Panagiotopoulos, A. Z. Self-Assembly of Cylinder-Forming Diblock Copolymer Thin Films. *Macromol.,* **2013**, 46 (16), 6651-6658.

33. Lyakhova, K. S.; Sevink, G. J. A.; Zvelindovsky, A. V.; Horvat, A.; Magerle, R. Role of dissimilar interfaces in thin films of cylinder-forming block copolymers. *J. Chem. Phys*., **2004**, 120 (2), 1127-1137.

34. Fasolka, M. J.; Benerjee, P.; Mayes, A. M.; Pickett, G.; Balazs, A. C. Morphology of Ultrathin Supported Diblock Copolymer Films: Theory and Experiment. *Macromol.,* **2000**, 33 (15), 5702-5712.

35. Mansky, P.; Chaikin, P.; Thomas, E.L. Monolayer films of diblock copolymer microdomains for nanolithographic applications. *J. Mater. Sci.*, **1995**, 30, 1987–1992.

36. Mansky, P.; Harrison, C.K.; Chaikin, P.M.; Register, R.A.; Yao N. Nanolithographic templates from diblock copolymer thin films. *Appl. Phys. Lett*., **1996**, 68 (18), 2586. (doi:10.1063/1.116192)

37. Park, M.; Harrison, C.; Chaikin, P.M.; Register, R.A.; Adamson D.H. Block copolymer lithography: periodic arrays of $\sim 10^{11}$ holes in 1 square centimeter. *Science,* **1997**, 276, 1401–1404.

38. Ferrarese, L. F.; Giammaria, T. J.; Volpe, F. G.; Lotto, F.; Seguini, G.; Pivac, B.; Laus, M.; Perego, M. High Aspect Ratio PS-b-PMMA Block Copolymer Masks for Lithographic Applications. *ACS Appl. Mater. Interfaces,* **2014**, 6 (23), 21389-21396.

39. Zajadacz, J.; Lorenz, P.; Frost, F.; Fechner, R.; Steinberg, C.; Scheer, H.-C.; Zimmer, K. Reactive ion beam etching of fused silica using vertical lamellar patterns of PS-b-PMMA diblock copolymer masks. *Microelectronic Engineering,* **2014**, 141, 289-293.

40. Yeon Sik Jung, Ross, C. A. Orientation-Controlled Self-Assembled Nanolithography Using a Polystyrene-Polydimethylsiloxane Block Copolymer. *Nano Lett*., **2007**, 7(7), 2046-2050.

41. Nose, T. Coexistence curves of polystyrene/poly(dimethylsiloxane) blends. *Polymer* **1995**, *36*, 2243-2248.

42. Bucholz, T. L.; Loo, Y. L. Phase Behavior of Near-Monodisperse Semifluorinated Diblock Copolymers by Atom Transfer Radical Polymerization. *Macromol.,* **2006**, 39 (18), 6075-6080.

43. O'Driscoll, B. M. D.; Kelly, R. A.; Shaw, M.; Mokarian-Tabari, P.; Liontos, G.; Ntetsikas, K.; Avgeropoulos, A.; Petkov, N.; Morris, M. A. Achieving structural control with thin polystyrene-*b*-polydimethylsiloxane block copolymer films: The complex relationship of interface chemistry, annealing methodology and process conditions. *Eur. Polym. J.*, **2013**, *49*, 3445-3454.

44. Mansky, P.; Liu, Y.; Huang, E.; Russell, T.P.; Hawker, C. Controlling Polymer-Surface Interactions with Random Copolymer Brushes. *Science,* **1997**, *275*, 1458.

45. Washo, B.D. Rheology and Modeling of the Spin Coating Process. Thickness of the film is determined by the concentration of the polymer in the solution and the spinning speed. *IBM 3. Develop*., 190 (**1977**).

46. Mansky, P.; Russell, T. P.; Hawker, C. J.; Mays, J.; Cook, D. C.; Satija, S. K. Interfacial Segregation in Disordered Block Copolymers: Effect of Tunable Surface Potentials. *Phys. Rev. Lett.*, **1997,** 79 (2), 237 – 240.

47. Fukunaga, K.; Elbs, H.; Magerle, R.; Krausch, G. Large-Scale Alignment of ABC Block Copolymer Microdomains via Solvent Vapor Treatment. *Macromol.,* **2000**, 33, 947-953.

48. Huang, W-H; Chen, P-Y; Tung, S-H; Effects of Annealing Solvents on the Morphology of Block Copolymer-Based Supramolecular Thin Films. *Macromol.,* **2012**, *45*, 1562-1569.
49. Lee, D. H.; Cho, H.; Yoo, S.; Park, S. Ordering evolution of block copolymer thin films upon solvent-annealing process *J. Coll. Interf. Sci.,* **2012**, *383*, 118–123.
50. Ramanathan, M.; Darling, S. B. Mesoscale morphologies in polymer thin films. *Progress in Polymer Science,* **2011**, 36, 793–812.
51. Limary, R.; Green, P. F. Hierarchical Pattern Formation in Thin Film Diblock Copolymers above the Order-Disorder Transition Temperature. *Macromol.,* **1999**, 32, 8167-8172.
52. Morkved, T.L.; Lu, M.; Urbas, A.M.; Ehrichs, E.E.; Jaeger, H.M.; Mansky, P.; Russell, T.P. Local Control of Microdomain Orientation in Diblock Copolymer Thin Films with Electric Fields. *Science,* **1996**, *273*, 931-933.
53. Singer, J.P.; Gotrik, K.W.; Lee, J.-H.; Kooi, S.E.; Ross, C.A.; Thomas, E.L. Alignment and reordering of a block copolymer by solvent-enhanced thermal laser direct write. *Polymer,* **2014**, *55*, 1875–1882.

54. Zhang, X.; Harris, K. D.; Wu, N. L. Y.; Murphy, J. N.; Buriak, J. M. Fast Assembly of Ordered Block Copolymer Nanostructures through Microwave Annealing. *ACSNano,* 2010, 4 (11), 7021–7029.

55. Angelescu, D. E.; Waller, J. H.; Adamson, D. H.; Deshpande, P.; Chou, S. Y.; Register, R. A.; Chaikin, P. M. Macroscopic Orientation of Block Copolymer Cylinders in Single-Layer Films by Shearing. *Adv. Mater*., **2004**, *16*, 1736-1740.
56. Li, L.; Yokoyama, H. Aligning single layer cylinders of block copolymer nanodomains using soft molding. *Adv. Mater*., **2005**, 17, 1432-1436.

57. Segalman, R. A.; Hexemer, A.; Kramer, E. J. Edge Effects on the Order and Freezing of a 2D Array of Block Copolymer Spheres. *Phys. Rev. Lett.,* **2003**, 91, 196101.
58. Segalman, R. A.; Yokoyama, H.; Kramer E. J. Graphoepitaxy of Spherical Domain Block Copolymer Films. *Adv. Mater*., **2001**, *13*, 1152-1155.

59. Jeong, S-J.; Moon, H-S.; Kim, B. H.; Kim, J. Y.; Yu, J.; Lee, S.; Lee, M. G.; Choi, H. Y.; Kim, S. O. Ultralarge-Area Block Copolymer Lithography Enabled by Disposable Photoresist Prepatterning. *ACS Nano*, **2010**, *4*, 5181–5186.
60. Ruiz, R.; Kang, H.; Detcheverry, F. A.; Dobisz, E.; Kercher, D. S.; Albrecht, T. R.; de Pablo, J. J.; Nealey, P. F. Density Multiplication and Improved Lithography by Directed Block Copolymer Assembly. *Science*, **2008**, 321(5891)**,** 936-939.
61. Jeong, S.-J.; Kim, Ji E.; Moon, H.-S.; Kim, B. H.; Kim, Su M.; Kim, Jin B.; Kim, S. O. Soft Graphoepitaxy of Block Copolymer Assembly with Disposable Photoresist Confinement. *Nano Letters*, **2009**, 9(6), 2300-2305.

62. Edwards, E. W.; Stoykovich, M. P.; Solak, H. H.; Nealey, P. F. Long-Range Order and Orientation of Cylinder-Forming Block Copolymers on Chemically Nanopatterned Striped Surfaces. *Macromol.*, **2006,** *39*, 3598-3607.
63. Cheng, J. Y.; Sanders, D. P.; Truong, H. D.; Harrer, S.; Friz, A.; Holmes, S.; Colburn, M.; Hinsberg W. D. Simple and Versatile Methods To Integrate Directed Self-Assembly with Optical Lithography Using a Polarity Switched Photoresist. *ACS Nano*, **2010**, 4(8), 4815–4823.
64. Park, S.-M.; Stoykovich, M. P.; Ruiz, R.; Zhang, Y.; Black, C. T.; Nealey, P. F. Directed Assembly of Lamellae-Forming Block Copolymers by Using Chemically and Topographically Patterned Substrates. *Adv. Mater.*, **2007**, 19, 607–611.

65. Xiao, S.; Yang, X.M.; Edwards, E. W.; La, Y.-H.; Nealey, P. F. Graphoepitaxy of cylinder-forming block copolymers for use as templates to pattern magnetic metal dot arrays. *Nanotechnology*, **2005**, 16, 324–329.
66. Pirkle, A.; Chan, J.; Venugopal, A.; Hinojos, D.; Magnuson, C. W.; McDonnell, S.; Colombo, L.; Vogel, E. M.; Ruoff, R. S.; Wallace, R. M. The effect of chemical residues on the physical and electrical properties of chemical vapor deposited graphene transferred to SiO2. *Appl. Phys. Lett.*, **2011**, 99, 122108.
67. Lin, Y.-C.; Lu, C.-C.; Yeh, C.-H.; Jin, C.; Suenaga, K.; Chiu, P.-W. Graphene Annealing: How Clean Can It Be? *Nano Lett.*, **2012**, 12, 414–419.
68. Kim, M.; Safron, N. S.; Han, E.; Arnold, M. S.; Gopalan, P. Fabrication and Characterization of Large-Area, Semiconducting Nanoperforated Graphene Materials. *Nano Lett.*, **2010,** 10 (4), 1125–1131.

69. Bai, J.; Zhong, X.; Jiang, S.; Huang, Yu; Duan, X. Graphene nanomesh. *Nat. Nanotechnol., **2010**, 5, 190-194.*

70. Jiao, L.; Xie, L.; Dai, H. Densely Aligned Graphene Nanoribbons at ~35 nm Pitch. *Nano Res.*, **2012**, 5(4), 292–296.

71. Liang, X.; Jung, Y.-S.; Wu, S.; Ismach, A.; Olynick, D. L.; Cabrini, S.; Bokor, J. Formation of Bandgap and Subbands in Graphene Nanomeshes with Sub-10 nm Ribbon Width Fabricated via Nanoimprint Lithography. *Nano Lett.*, **2010,** 10, 2454—2460.

72. Liu, G.; Wu, Y.; Lin, Y-M; Farmer, D. B.; Ott, J. A.; Bruley, J.; Grill, A.; Avouris, P.; Pfeiffer, D.; Balandin, A. A.; Dimitrakopoulos, C. Epitaxial Graphene Nanoribbon Array Fabrication Using BCP-Assisted Nanolithography. *ACS nano*, 2012, 6(8), 6786–6792.

73. Son, J.G.; Son, M., Moon, K.J.; Lee B.H.; Myoung, J.M.; Strano M.S.; Ham M.H.; Ross C.A. Sub-10 nm Graphene Nanoribbon Array Field-Effect Transistors Fabricated by Block Copolymer Lithography. *Adv Mater*., **2013,** 25(34), 4723-4728.

74. Liu, L.Z.; Tian, S.B.; Long, Y.Z.; Li, W.X.; Yang, H.F.; Li, J.J.; Gu, C.Z. Tunable periodic graphene antidot lattices fabricated by e-beam lithography and oxygen ion etching. *Vacuum* **2014**, 105, 21-25.

75. Fischbein, M.D.; Drndic, M. Electron beam nanosculpting of suspended graphene sheets. *Appl. Phys. Lett.*, **2008**, 93, 113107.

76. Qi, Z. J.; Rodríguez-Manzo, J. A.; Hong, S. Ju; Park, Y. W.; Stach, E. A.; Drndic, M.; Charlie Johnson, A. T. Direct electron beam patterning of sub-5nm monolayer graphene interconnects. *Proc. of SPIE,* **2013**, 8680, 86802F-1.

77. Bell, D.; Lemme, M.; Stern, L.; Williams, J.; Marcus, C. Precision cutting and patterning of graphene with helium ions**.** *Nanotechnology*, **2009**, 20, 455301.

78. Winston, D.; Manfrinato, V.R.; Nicaise, S.M.; Cheong, L.L.; Duan, H.; Ferranti, D. Neon ion beam lithography (NIBL). *Nano Lett*, **2011**, 11, 4343–4347.

79. Tapaszto, L.; Dobrik, G.; Lambin, P.; Biro, L.P. Tailoring the atomic structure of graphene nanoribbons by scanning tunnelling microscope lithography. *Nat. Nanotechnol*., 2008, 3, 397–401.

80. Giesbers, A.; Zeitler, U.; Neubeck, S.; Freitag, F.; Novoselov, K.; Maan, J. Nanolithography and manipulating of graphene using an atomic force microscope. *Solid State Commun.*, **2008**, 147, 366–369.

81. Gopalakrishnan, N.; Sagar, K. S.; Christiansen, M. B.; Vigild, M. E.; Ndoni, S.; Kristensen, A. UV patterned nanoporous solid-liquid core waveguides. *Opt. Express* **2010**, 18, 12903 12908.

82. Kitagawa, K. Thin-film thickness profile measurement by three-wavelength interference color analysis. *Applied Optics*, **2013**, 52 (10), 1998- 2007.

83. Meyer, E. Atomic Force Microscopy. *Prog. Surf. Sci.,* **1992**, 41, 3-49.

84. Suga, M.; Asahina, S.; Sakuda, Y.; Kazumori, H.; Nishiyama, H.; Nokuo, T.; Alfredsson, V.; Kjellman, T.; Stevens S.M.; Cho, H.S.; Cho, M.; Han, Lu; Che, S.; Anderson, M.W.; Schüth, F.; Deng,H.; Yaghi O.M.; Liu, Z.; Jeong, Hu Y.; Stein, A.; Sakamoto, K.; Ryoo R.; Terasaki. O. Recent progress in scanning electron microscopy for the characterization of fine structural details of nano materials. *Prog. Solid State Ch.*, **2014**, 42, 1-21.

85. Kuo, W. C. H.; Briceno, M.; Ozkaya, D. Final Analysis: Characterisation of Catalysts Using Secondary and Backscattered Electron In-lens Detectors. *Platinum Metals Rev*., **2014**, 58 (2), 106.

86. http://www.microscopy.ethz.ch/se.htm.

87. Ferrari, A. C.; Basko, D. M. Raman spectroscopy as a versatile tool for studying the properties of graphene. *Nat. Nanotechnol*., **2013**, 8, 235-246.

88. Jorio, A. Raman Spectroscopy in Graphene-Based Systems: Prototypes for Nanoscience and Nanometrology. *ISRN Nanotechnology*, Vol. **2012**, article ID 234216, 16 pages; doi:10.5402/2012/234216.

89. Sinitskii, A.; Tour, J. M. Patterning Graphene through the Self-Assembled Templates: Toward Periodic Two-Dimensional Graphene Nanostructures with Semiconductor Properties. *J. Am. Chem. Soc.*, **2010**, 132, 14730–14732.

90. Wall, M. The Raman Spectroscopy of Graphene and the Determination of Layer Thickness. Thermo Fisher Scientific, Application note 52252, www.thermoscientific.com.

91. Schulte, L.; Grydgaard, A.; Jakobsen, M. R.; Szewczykowski, P. P.; Guo, F.; Vigild, M. E.; Berg, R. H.; Ndoni, S. Nanoporous materials from stable and metastable structures of 1,2-PB-b-PDMS block copolymers. *Polymer*, **2011**, 52, 422-429.

92. Studler, D.; Gnaegi, H. Minimal compression of ultrathin sections with use of an oscillating diamond knife. *J. Microsc*. **2000**, 197, 94-100.
93. https://www.diatomeknives.com/knives/trim.aspx
94. Oehrlein, G.S.; Chan, K.K.; Jaso, M.A.; Rubloff, G.W. Surface analysis of realistic semiconductor microstructures. *J. Vac. Sci. Technol*. **1989**, A **7**, 1030-1034.
95. Jansen, H.; de Boer, M.; Legtenberg, R.; Elwenspoek, M. The black silicon method: a universal method for determining the parameter setting of a fluorine-based reactive ion etcher in deep silicon trench etching with profile control. *J. Micromech. Microeng*. **1995**, 5**,** 115-120.
96. Laermer, F.; Schilp, A. Method of anisotropically etching silicon. **1994**, German Patent DE4241045C1 and US Patent 5501893.
97. Chen, S. C.; Lin, Y. C.; Wu, J. C.; Horng, L.; Cheng, C. H. Parameter optimization for an ICP deep silicon etching system. *Microsyst. Technol*., **2007**, 13, 465–474.
98. Ledernez, L.; Olcaytug, F.; Yasuda, H.; Urban G. A modification of Paschen law for Argon. 29th ICPIG, July 12-17, 2009, Cancun, Mexico.
99. Egitto, F. D. Plasma etching and modification of organic polymers. *Pure* & *Appl. Chem.,* **1990**, 62 (9), 1699-1708.
100. Hayashida, K.; Saito, N.; Arai, S.; Takano, A.; Tanaka, N.; Matsushita Y. Hierarchical Morphologies Formed by ABC Star-Shaped Terpolymers. *Macromol.*, **2007**, 40 (10), 3695-3699.

101. Han, E.; Stuen, K. O.; La, Y-H; Nealey, P. F.; Gopalan, P. Effect of Composition of Substrate-Modifying Random Copolymers on the Orientation of symmetric and Asymmetric diblock Copolymer Domains. *Macromol.*, **2008**, 41(23), 9090-9097.

102. Zhang, Yi; Zhang, L.; Zhou, C. Review of Chemical Vapor Deposition of Graphene and Related Applications. *Accounts of Chemical Research,* **2013**, 46 (10), 2329–2339.

103. Petrone, N.; Dean, C. R.; Meric, I.; van der Zande, A. M.; Huang, P. Y.; Wang, L.; Muller, D.; Shepard, K. L.; Hone, J. Chemical Vapor Deposition-Derived Graphene with Electrical Performance of Exfoliated Graphene. *Nano Lett.*, **2012**, *12* (6), 2751–2756.

104. Blake, P.; Hill, E. W.; Castro Neto, A. H.; Novoselov, K. S.; Jiang, D.; Yang, R.; Booth, T. J.; Geim, A. K. Making graphene visible. *Appl. Phys. Lett.,***2007**, 91, 063124.

105. Shklovskii, B. I.; Efros, A. L. Electronic Properties of Doped Semiconductors. Springerr Series in Solid State Sciences; *Springer*, Berlin, 1984; Vol. 45.

106. Gunlycke, D.; Areshkin, D. A.; White, C. T. Semiconducting graphene nanostrips with edge disorder. *Appl. Phys. Lett*. **2007**, 90, 142104.

107. Adam, S.; Cho, S.; Fuhrer. M. S.; Das Sarma, S. Density inhomogeneity driven percolation metal-insulator transition and dimensional crossover in graphene nanoribbons. *Phys. Rev. Lett*.**, 2008,**101**,** 046404.

108. Sols, F.; Guinea, F.; Castro Neto, A. H. Coulomb Blockade in Graphene Nanoribbons. *Phys. Rev. Lett.*, **2007**, 99, 166803.

109. Dröscher, S.; Knowles, H.; Meir, Y.; Ensslin, K.; Ihn, T. Coulomb gap in graphene nanoribbons. *Phys. Rev. B*, **2011**, 84, 073405.

110. Reserbat-Plantey, A.; Kalita, D.; Han, Z.; Ferlazzo, L.; Autier-Laurent, S.; Komatsu, K.; Li, C.; Weil, R.; Ralko, A.; Marty, L.; Guéron, S.; Bendiab, N.; Bouchiat, H.; Bouchiat, V. Strain Superlattices and Macroscale Suspension of Graphene Induced by Corrugated Substrates. *Nano Lett.*, **2014**, 14 (9), 5044-5051.

111. Blees, M. K.; Barnard, A. W.; Rose, P. A.; Roberts, S. P.; McGill, K. L.; Huang, P. Y.; Ruyack A. R., Kevek, J. W.; Kobrin, B.; Muller D. A.; McEuen, P. L. Graphene kirigami. *Nature*, **2015**, doi:10.1038/nature14588.

Langmuir

Article

pubs.acs.org/Langmuir

Transfer of Direct and Moiré Patterns by Reactive Ion Etching Through Ex Situ Fabricated Nanoporous Polymer Masks

Violetta Shvets,*[,†,‡] Thomas Hentschel,[†,§] Lars Schulte,[†,‡] Lisa K. Tschammer,[†,‡] Alberto Cagliani,[†,‡] Peter Bøggild,[†,‡] Kristoffer Almdal,[†,‡] and Sokol Ndoni*[,†,‡]

[†]Technical University of Denmark, Dept. of Micro and Nanotechnology, Ørsteds Plads, Building 345 East, DK-2800 Kgs. Lyngby, Denmark

[‡]Center for Nanostructured Graphene (CNG), Technical University of Denmark, Ørsteds Plads, Building 345 East, DK-2800 Kgs. Lyngby, Denmark

[§]Dow Olefinverbund GmbH, D-06201 Merseburg, Germany

S *Supporting Information*

ABSTRACT: We present a conceptually simple approach to nanolithographic patterning utilizing ex situ fabricated nanoporous masks from block copolymers. The fabricated block copolymer (BC) masks show predictable morphology based on the correlation between BC composition and bulk properties, independent of substrates' surface properties. The masks are prepared by microtoming of prealigned nanoporous polymer monoliths of hexagonal morphology at controlled angles; they appear as 30−60 nm thick films of typical dimensions 100 μm × 200 μm. Masks cut perpendicular to the cylindrical axis show monocrystalline hexagonal packing of 10 nm pores with a principal period of 20 nm. We demonstrate the transfer of the hexagonal pattern onto silicon by means of reactive ion etching through the masks. In addition, patterns of elliptic and slit-like holes on silicon are obtained by utilizing masks cut at 45° relative to the cylinder axis. Finally, we demonstrate the first transfer of moiré patterns from block copolymer masks to substrate. The nanoporous masks prepared ex situ show outstanding long-range order and can be applied directly onto any flat substrate, eliminating the need for topographic and chemical surface modification, which are essential prerequisites for the conventional procedure of block copolymer directed self-assembly. The demonstrated elliptic and moiré pattern transfers prove that the proposed ex situ procedure allows us to realize nanolithographic patterns that are difficult to realize by the conventional approach alone.

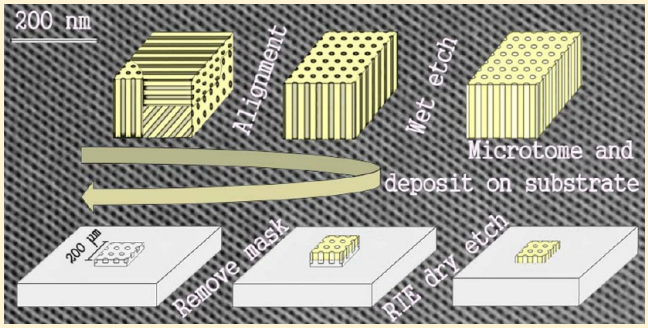

INTRODUCTION

Block copolymers consist of two or more covalently linked homopolymers. Microphase separation occurs under thermodynamic conditions of immiscibility between the blocks, and self-organized structures of different morphologies are formed depending on composition.[1,2] Self-assembled block copolymers are widely used as templates for pattern creation on various substrates,[3−5] which is directly mentioned as a possible route to next-generation chip fabrication in the International Roadmap of Semiconductor Technology.[6] For a given block copolymer the "conventional" pattern transfer procedure comprises spin-casting on pretreated substrates of 20−100 nm thin films, thermal or solvent vapor annealing of the film, and selective plasma etching for pattern transfer to the substrate. Such a procedure was, for example, applied in ref 7 for high-resolution nanopatterning of graphene. The method appeared to be quite straightforward, but in our experience the results proved to be rather challenging to reproduce. Self-assembling of block copolymer thin films is very much affected by variations of many parameters, like the interface energy between the substrate or air and the polymer blocks, film thickness and uniformity, conditions of annealing, presence of structural or chemical guides for alignment, long-range order and defect control, and so on.[8] Fine-tuning of these parameters is needed for every change of the polymer or substrate, even in the case of different batches of essentially the same block copolymer. This tuning comprises substrate preparation, such as priming/cleaning (often involving use of Piranha or oxygen plasma and/or repeated rinsing with organic solvents), chemical modification (e.g., by grafting of a brush layer of well controlled composition that provides a neutral layer for the constituting polymer blocks[9]), and annealing conditions (e.g., solvent,[10] time,[11] temperature, evaporation mode,[12] and for more special annealing forms, the type and intensity of electric field[13] or laser[14] applied); however, surface modification and annealing do not provide predictable long-range in-plane ordered

Received: October 4, 2014
Revised: April 19, 2015
Published: May 18, 2015

Scheme 1. Work Flow of the Proposed Nanolithographic Process[a]

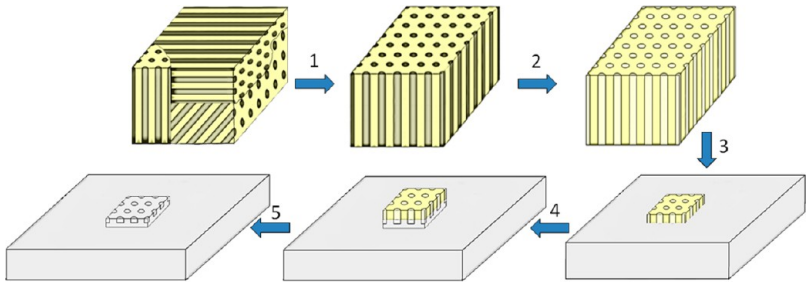

[a](1) 1,2-PB-*b*-PDMS with random domain orientation is shear-aligned and cross-linked to fix the structure. (2) PDMS is selectively etched to get nanoporous PB (nPB). (3) nPB is sliced in a microtome at room temperature. The flakes suspended in a water droplet captured within a home-made metallic loop are transferred onto a silicon wafer. (4) Silicon etching by RIE, which transfers the pattern to the substrate under the mask and uniformly etches the silicon outside of the mask. (5) Mask removal by oxygen plasma. If appropriate, step (2) may be bypassed and the etching procedure accordingly adapted.

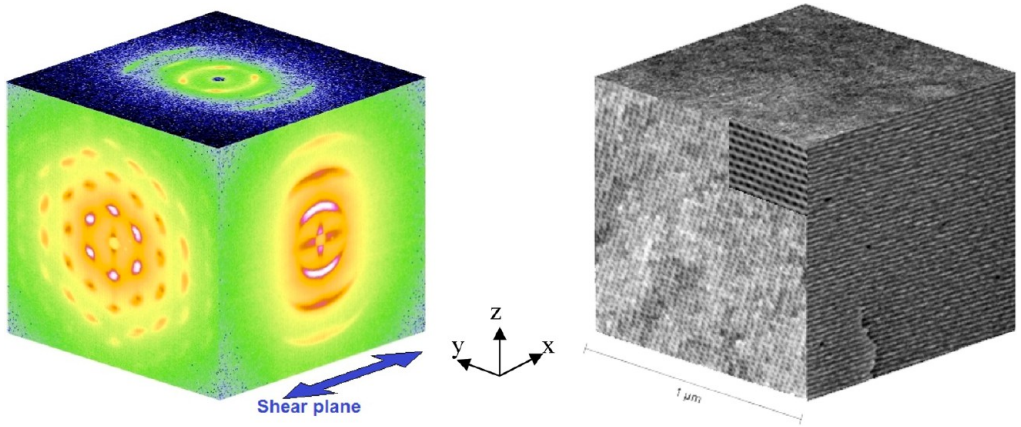

Figure 1. Composed SAXS (left) and SEM (right) images from the shear aligned nanoporous PB-*b*-PDMS block copolymer samples. The applied shear direction is along the *x* axis with shear planes parallel to the *xy* plane. There are three sets of principal planes for the HEX morphology; one of the sets is parallel to the shear planes and the other two rotated at 60 and 120° relative to the *x* axis. A magnified image is shown as inset on the top-right corner of the *yz* SEM projection.

structures. Directed self-assembly (DSA) by graphoepitaxy[15] and chemoepitaxy[16] were developed to achieve this. In both methods the substrate is preconfigured by guiding patterns, relief guiding patterns in the case of graphoepitaxy, and chemical composition guiding patterns in the case of chemoepitaxy. In-plane shear alignment of BC thin films has also been reported as a means to create long-range order of line patterns from BC of hexagonal morphology.[17]

The multilayer structures often created by the mentioned procedures may impose an increased number of etching steps. We present a conceptually simple approach to nanolithography, which renders obsolete all surface modification and polymer annealing steps mentioned above and reduces to a minimum the number of etching steps required for pattern transfer. The mask is fabricated separately from the substrate by microtomy, following a procedure inspired from sample preparation for transmission electron microscopy (TEM);[18] however, the masks we produce show uniform thickness in areas 3−5 orders of magnitude larger than typical uniform areas of TEM samples, as shown in the Results and Discussion section. Scheme 1 shows the work flow of the proposed procedure. The approach is demonstrated here by using a macroscopic sample of 1,2-polybutadiene-*b*-polydimethilsiloxane (PB-*b*-PDMS) block copolymer with cylindrical morphology[19] as a precursor material. First, the structure is aligned by shearing the polymer between two parallel plates, which gives crystalline-like order for the bulk of the polymer with principal crystallographic planes oriented parallel to the plates,[20,21] as illustrated in Figure 1. Then, the 1,2-PB microphase is cross-linked to fix the structure and the PDMS microphase is selectively degraded.[22] The obtained monolith is a rigid cross-linked polybutadiene permeated by aligned hexagonally packed cylindrical nanopores with approximate volume fraction of 30%. Subsequently, the nanoporous polymer is sliced in a microtome obtaining sheets (or flakes) 70−300 μm across with thickness in the range of 30−60 nm. The sheets are then transferred directly to the substrate, here silicon wafer, and pattering performed with reactive ion etching (RIE). After removal of the mask by a final oxygen plasma treatment,[23] isles of nanostructured silicon can be observed. Alternatively, step 2 can be bypassed and microtomy directly applied to the cross-linked BC. In the present report we will follow the workflow shown in Scheme 1.

To the best of our knowledge, this is the first report on ex situ fabrication of nanolithographic masks by microtomy of prealigned block copolymers. We found one report describing the use of an ex situ anodic aluminum oxide membrane with pore size of 80 nm and membrane thickness of 1 μm as a template for fabrication of a graphene nanomesh.[24]

DOI: 10.1021/acs.langmuir.5b00482
Langmuir 2015, 31, 6245−6252

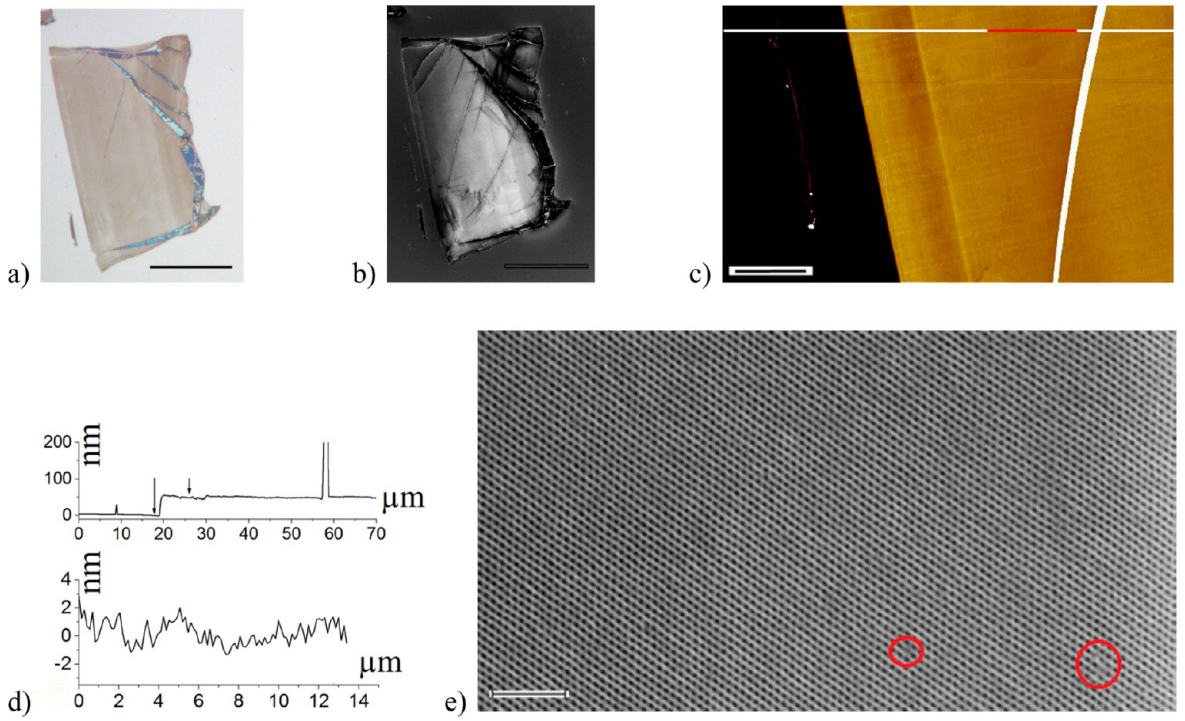

Figure 2. Images of microtomed nPB flakes on silicon. (a) Optical microscope image of 50 nm thick nanoporous flake at 20× magnification; 100 μm scale bar. (b) Low-magnification SEM image of the same nPB flake; 100 μm scale bar. (c) AFM image of the nPB flake; 10 μm scale bar. (d) Height profiles along the white and red line in panel c. (e) SEM image of the nPB flake; 200 nm scale bar. The three observed lattice defects are enclosed by the red circles; there are two defects inside the bigger circle.

EXPERIMENTAL SECTION

A 1,2-polybutadiene-*b*-polydimethilsiloxane (PB-*b*-PDMS) block copolymer of hexagonal morphology, with molecular weight of 17 800 g/mol, polydispersity index of 1.03 and mass composition of 66:34 PB:PDMS, was used as a precursor. It was prepared by sequential "living" anionic polymerization in tetrahydrofuran.[25] The block copolymer was manually shear aligned and then cross-linked.

The principal period of the microphase separated structure is 21.6 nm, as determined by small-angle X-ray scattering (SAXS), and the PDMS cylinder diameter was estimated to be 14 nm from the volume composition of the blocks. The 2D SAXS images of shear aligned sample shown in Figure 1 testify a high degree of order; the scattering on the *yz* and *xz* planes agrees with the corresponding scanning electron microscopy (SEM) images also shown in Figure 1. Scattering on the *xy* plane is significantly weaker than on the two orthogonal planes, and the profile could be partially due to misalignment of the BC close to the interface with the glass; a thin layer of polymer in contact with glass remains essentially immobile during the alignment process, giving rise to the weak scattering in the *xy* plane. This is discussed in more detail in the available Supporting Information.

Finally, the PDMS block was degraded quantitatively by treatment with tetra (*n*-butyl ammonium) fluoride (TBAF). More details of these steps can be found in refs 19 and 22 and in the Supporting Information.

Nanoporous polymer pieces were sliced with an ultrasonic oscillating diamond knife from DiATOME on a Leica EMFCS ultracut UCT microtome. Ultrasonic microtomy allows us to cut ultrathin sections with significantly reduced mechanical compression,[26] which is important for cutting of soft materials like polymers and biological samples. Details of the microtomy and sample transfer onto substrate can be found in the Supporting Information. Sections floating in the groove of the knife filled with DI water were picked up with a homemade metal loop and deposited directly onto clean silicon p-type ⟨100⟩ wafer with 2 nm native oxide layer. The sample on wafer was finally rinsed with isopropanol.

A Nikon ECLIPSE L200 microscope with 20× and 50× magnification lenses was used for optical imaging. SEM imaging was done in a high-resolution field-emission Zeiss Ultra Plus SEM with a Gemini column. The scanning electron microscopy (SEM) images were obtained at acceleration voltages of 2 to 3 keV in high vacuum without sample sputtering.

Atomic force microscopy (AFM) in tapping mode with standard noncontact tips was performed on a Park System equipment XE-150 Advanced Scanning probe microscope. Images were processed with the XEI Park System Software.

The pattern transfer was effectuated by dry etching following two procedures, depending on the instrument availability in the clean room. The conditions are described in the Supporting Information.

RESULTS AND DISCUSSION

The size of nanoporous polymer samples obtained by oscillating diamond knife was between 70 and 300 μm with a thickness in the range of 30−60 nm. Images of a polymer flake on a silicon substrate recorded by optical microscopy and low-magnification SEM are presented in Figures 2a,b, respectively. Some features are better observed in electron microscopy, others in optics. For example, film thickness directly correlates with its color in an optical microscope. The effective refractive index of our nanoporous polymer can be estimated from the Lorentz−Lorenz relation and equals 1.3,[27] so a 50 nm thick flake will have light brown color because contribution in destructive interference is larger for shorter wavelengths and blue color is suppressed.[28] During slicing the knife was fixed parallel to the long side of the flake and the sample moved in perpendicular direction. The visible stripes of slightly different color saturation parallel to the long side of the flake are most probably due to external vibrations and noise during slicing.

Accurate thickness measurements were made by AFM. The AFM image in Figure 2c is from the middle-left part of the

DOI: 10.1021/acs.langmuir.5b00482
Langmuir 2015, 31, 6245−6252

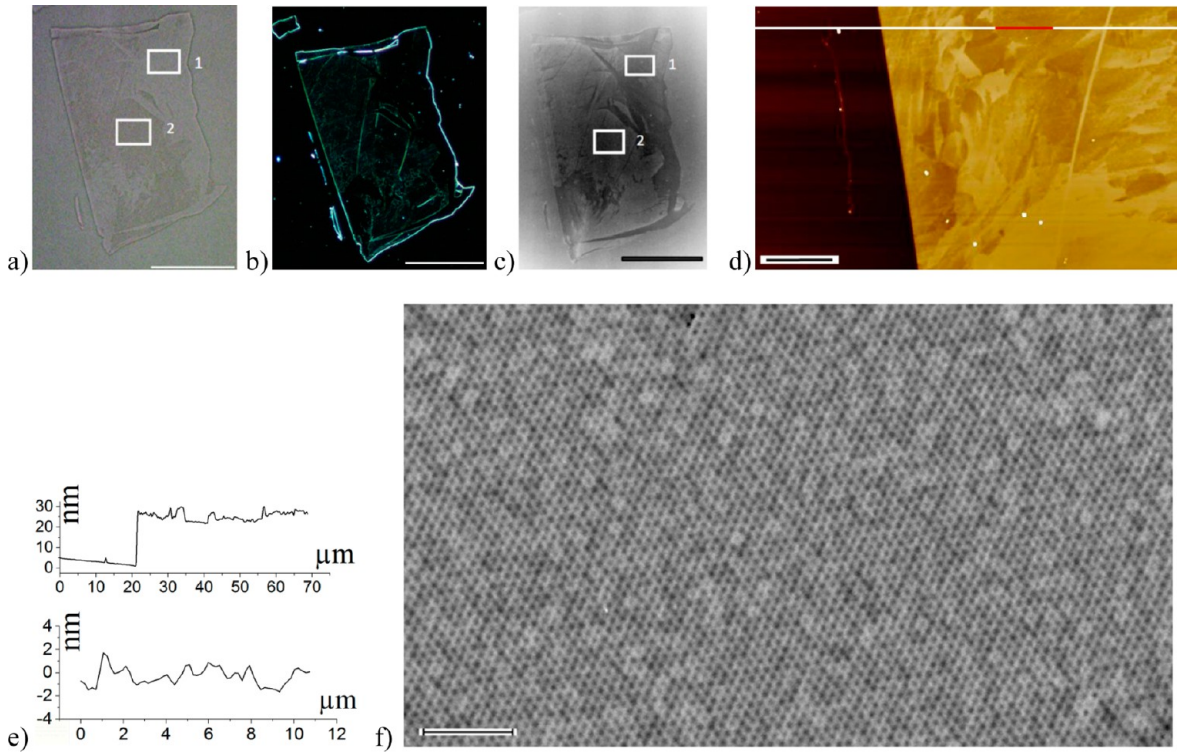

Figure 3. Silicon surface after 10 s of oxygen treatment, followed by 20 s of silicon etch and 10 min oxygen plasma cleaning. (a) Optical bright-field image of the silicon plateau that remains under the flake when surrounding silicon is etched; 100 μm scale bar. (b) Optical dark-field image of the same plateau; 100 μm scale bar. (c) Low-magnification SEM; 100 μm scale bar. (d) AFM image of the plateau; 10 μm scale bar. (e) Height profiles along the white and red segment in panel d. (f) SEM image of nanostructured silicon; 200 nm scale bar.

flake. Images were flattened taking the surface of the substrate to be horizontal. The profile along the white line in panel c yields a thickness of 49 nm as an average height difference between 4 μm sections centered at the arrows in panel d. The out-of-scale peak at 58 μm in panel d is due to the fold visible as a white stripe in panel c. The root-mean-square (r.m.s.) roughness along the dark (red online) segment is 0.9 nm, which is similar or better than typical r.m.s. roughness of spin-cast polymer thin films.[29,30]

The top-down SEM image of the nanoporous mask shown in Figure 2e reveals an exceptional degree of order. We were able to identify only three lattice defects on the 1 × 1.5 μm^2 image, as highlighted by the red circles. This type of imperfection, <1/1000 in the shown case, is probably due to polymer debris clogging few nanopores or to a small amount of unetched PDMS. Partially filled pores are expected to impede pattern transfer, and hence the number of filled pores should be kept as low as possible. The period measured on the SEM image is 20 nm, which is 7% smaller than the period of the unetched monolith; the shrinkage could be due to structure relaxation after PDMS etching. The apparent pore size is ∼10 nm.

During RIE the silicon surface outside the mask is etched down faster than under the mask so that a silicon plateau in the mask shape with nanostructures on top is formed; see Figure 3. The bright field (BF) optical image in Figure 3a shows much lower contrast than that in Figure 2a, and only edges of the plateau are properly visible; gray regions with the same color as the surrounding substrate (like in box 1) are not nanostuctured; the faint brown hue regions (box 2) coincide with nanostructured regions. Edges are easily observed in dark-field optical microscopy (Figure 3b). Nanostructured regions in low-magnification SEM (Figure 3c) appear as light gray areas (box 2). The gray areas (box 1) in Figure 3c correspond to the mask folds (compare with the dark areas in Figure 2b). All of the bright regions within the original mask area show nanopatterns with nearly the same quality as the image of Figure 3f. The hole array in Figure 3f shows the pattern transferred on silicon. The highly regular hexagonal pattern has a period of 20 nm, identical to the period of the nanoporous mask. It covers uniform areas in excess of 40 × 25 μm^2.

On the AFM image (Figure 3d) recorded at the same place as before etching, a mosaic of regions with different heights is seen. The roughness along the red segment is within ±1.5 nm, and the r.m.s. roughness is 0.9 nm, the same as for the mask. This difference in etching rates across the flake may be accounted for by imperfect contact between mask and substrate. In this picture, the mask being dropped uncontrollably from water onto the substrate could easily lead to wrinkles and other nonplanar structures that enclose different empty volumes between mask and substrate. Such voids promote lateral etching, leading to differences in the height of structured regions. Efforts to improve the controllability of the mask deposition are ongoing, with the aim of maximizing the useful mask area. The small height variations appearing in Figure 3e as a nonuniform gray background are most likely caused by mask roughness.

Patterns of different symmetry can be obtained from the same cylindrical block copolymer by varying the cutting angle relative to the cylinder axis. In this way, we can create patterns of ellipses and lines (the last by cutting parallel to the cylinder axis) instead of the circular dots obtained at a cutting angle of 90°. At cutting angles different from 90° the structural periods on the mask will increase and the hexagonal symmetry will be broken. We present now the pattern transfer through a mask

DOI: 10.1021/acs.langmuir.5b00482
Langmuir 2015, 31, 6245−6252

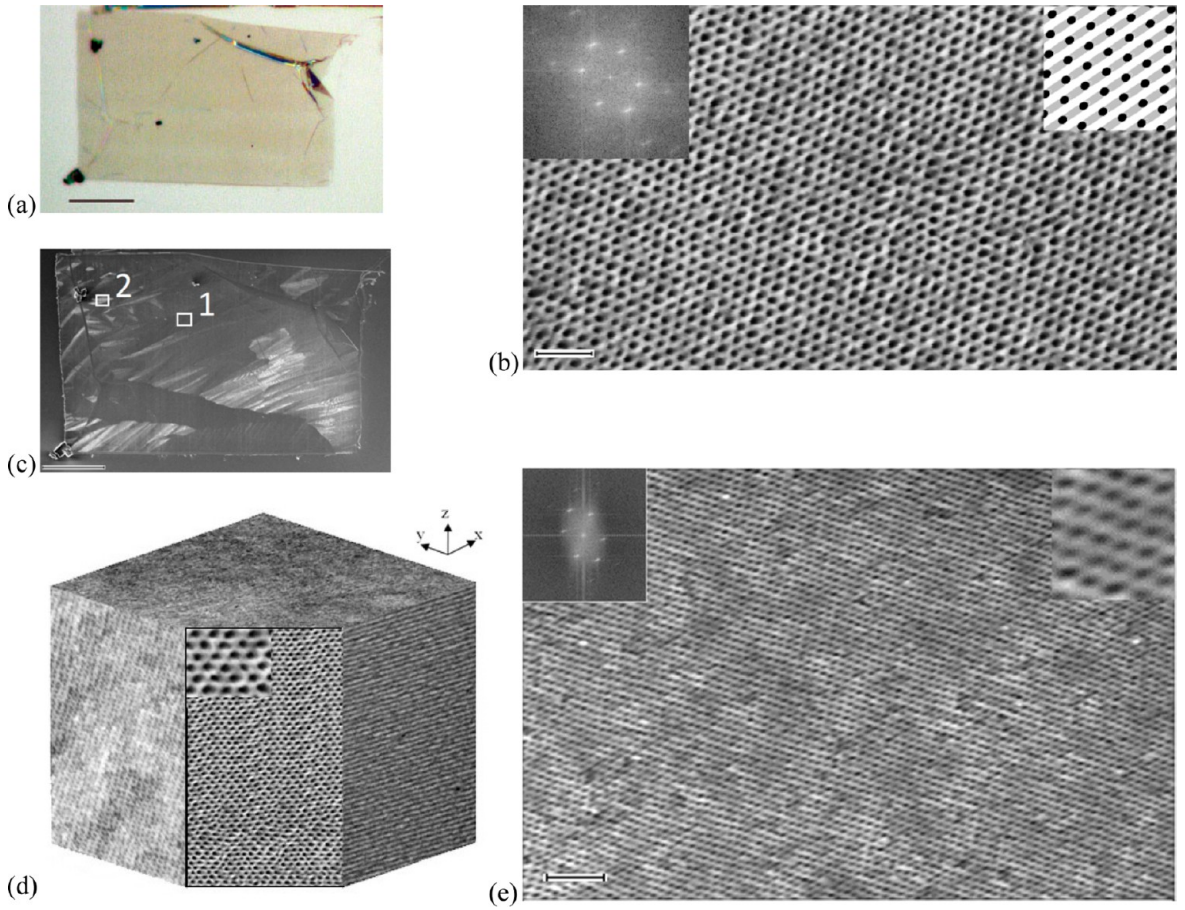

Figure 4. Mask prepared by cutting at 45° with respect to cylinder axis and respective patterns transferred onto silicon. (a) Optical image of the original 30 nm thick nanoporous flake at 50× magnification; 20 μm scale bar. (b) High-resolution SEM of the polymer mask; 200 nm scale bar. FFT of the pattern is shown in the top-left inset, while the top-right inset shows a model of the mask. (c) Overview of nanostructured plateau by SEM; 20 μm scale bar. (d) 3D rendition of the 45° mask cut adapted from the composed SEM cube of Figure 1. The cutting plane is parallel to the z axis and intersects the x and y axes at equal coordinate values. (e) High-resolution SEM image of box 1 in panel c; 200 nm scale bar. The top-left inset is a FFT of the pattern, while the top-right inset shows a magnified image of the elliptical hole pattern on silicon.

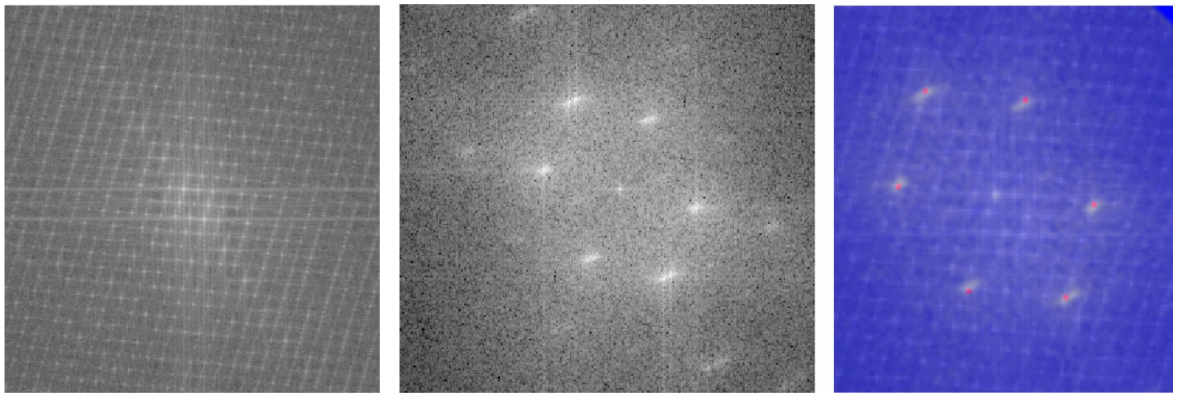

Figure 5. Comparison of the FFTs for the mask in Figure 4b with the FFT of the model shown in the top-right inset of Figure 4b. Left, FFT of the model; center, FFT of the mask's SEM image in Figure 4b; and right, superposition of the two FFTs illustrating the agreement between the two. Red dots highlight selected spots from the FFT of the model.

cut at 45° relative to the cylinder axis, as shown in Figure 4. The mask shown in Figure 4a was a 30 nm thin rectangular film of size 100 μm × 70 μm. A high-resolution top-down SEM image of the mask is shown in Figure 4b. The fast Fourier transform (FFT) of the image is shown in the top-left inset. The SEM image is compatible with the model shown in the top-right inset. The model represents the planar cut of an ideal hexagonal cylindrical porous structure at 45° relative to the cylindrical pore axis and perpendicular to one set of structure principal planes, as rendered in Figure 4d (adapted from the SEM image in Figure 1). The black spots in the model represent the elliptical cuts of the cylindrical pores. The gray areas in the model represent projections of the pore channels on the mask plane. The angles on the FFT image of the mask

DOI: 10.1021/acs.langmuir.5b00482
Langmuir 2015, 31, 6245−6252

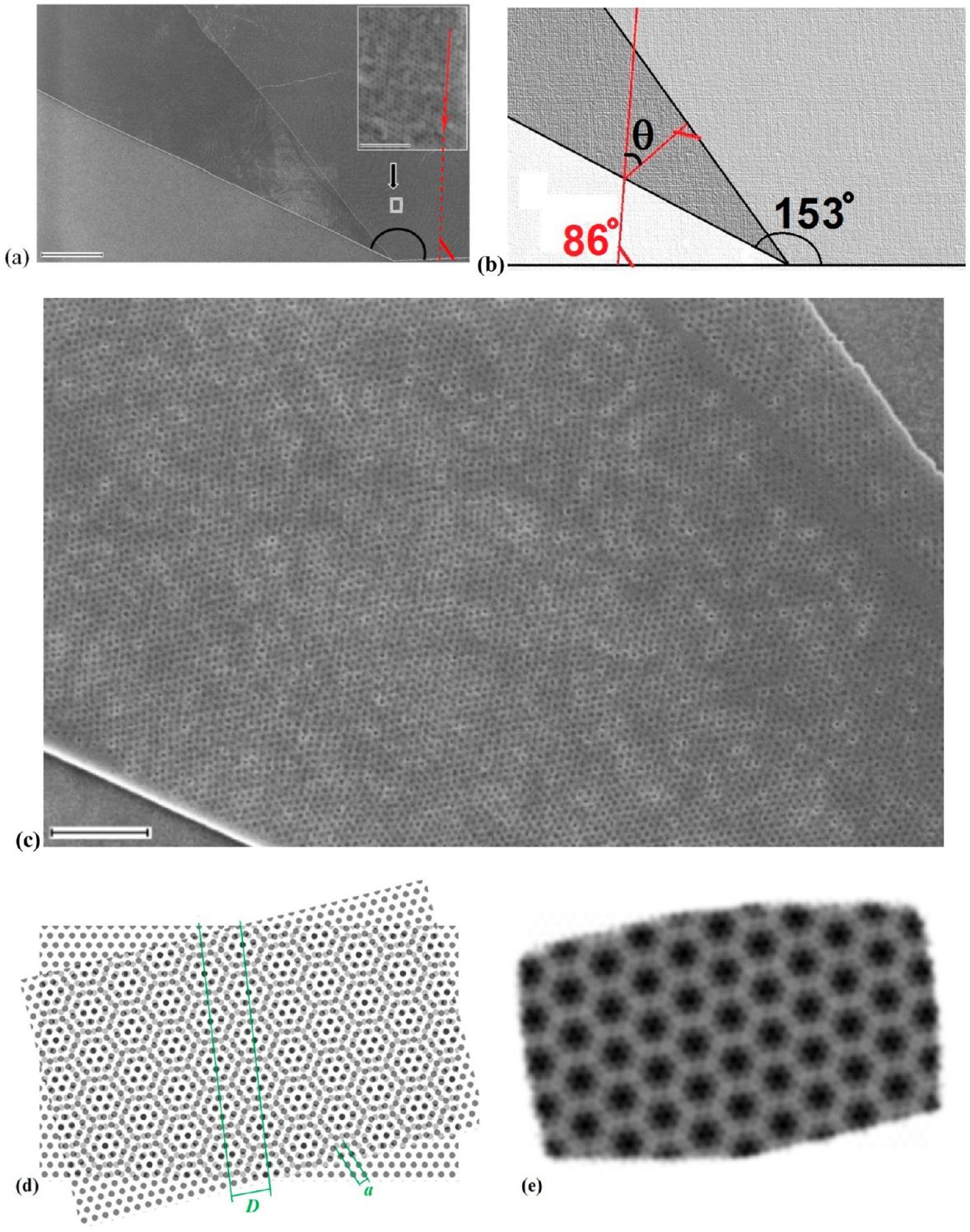

Figure 6. Moiré patterns on silicon. (a) Low-magnification SEM of the pattern transferred onto the silicon substrate at the location of a mask fold. Inset shows the ground HEX structure alignment on a magnified image of an area at the vicinity of the fold. Scale bars are 10 μm for the image and 200 nm in insertion. (b) Scheme of rotation angle calculation with known folding angle and HEX translation direction. (c) Higher magnification SEM image from panel a. The period of the hexagonal pattern formed under the mask fold is 78 nm, that is, 3.9 times the ground period; 1 μm scale bar. (d) Model illustrating the moiré patterns generated by superimposition of two hexagonal lattices rotated by 14°. The pattern is not strictly periodic with period *D*, as can be observed by variations of the intersection of the green lines defining *D* within the different moiré cells. (e) Image obtained by low-pass filtration of the image in panel d.

are in agreement (within 1 to 2°) with the respective angles for the model, as shown in Figure 5.

After etching, many nuances of gray are visible in the SEM image of the nanostructured areas, as evidenced in Figure 4c. The different shades correlate with local differences in the pitch of the nanostructures. The areas with larger local pitch appear brighter in the SEM image. An image of an undistorted pattern that replicates the mask lattice is shown in Figure 4e. The FFT

DOI: 10.1021/acs.langmuir.5b00482
Langmuir 2015, 31, 6245−6252

of the transferred pattern is similar to the FFT of the mask. The brightest areas in Figure 4c comprise patterns with a large pitch, up to half a micron, changing in size and in direction, as shown in Figure S1 of the Supporting Information. Such complex patterns probably have their origin from areas where the mask does not adhere to the substrate.

Finally, we demonstrate the first transfer onto the underlying substrate of moiré patterns created by double-layer block copolymer mask. Moiré patterns from TEM images of superimposed block copolymer thin films have been reported 7 to 8 years ago, and their possible use in nanolithography was contemplated.[31] Figure 6 shows SEM images of nanostructured silicon under a nanoporous mask area with a well-defined fold. The low-magnification SEM image in Figure 6a allows us to characterize the fold, as shown in Figure 6b. The inset in Figure 6a shows a higher magnification image of the single-layer mask in the vicinity of the fold with one set of principal directions parallel to the red arrow, which forms an angle of 86° with the mask base. $\boldsymbol{\theta}$ in Figure 6b marks the rotational angle of this direction on the top layer of the fold. It can be calculated from Figure 6b by elementary triangulation

$$\boldsymbol{\theta} = 86° + 2\cdot(180° - 153°) - (180° - 86°) = 46° \quad (1)$$

(see Figure 6 b).

A higher magnification SEM image of the moiré pattern is shown in Figure 6c. The period of the hexagonal moiré pattern is ∼78 nm, which is 3.9 times bigger than the "ground" period of the BC mask, 20 nm. According to the moirè pattern theory developed by Oster et al.,[32] the superposition of two equidistant line sets with periods a and b rotated by an angle θ leads to a moirè pattern with periodicity D

$$D = ab/(a^2 + b^2 - 2ab\cos\theta)^{0.5} \quad (2)$$

The relation is an even function of the angle θ; therefore, we may consider only positive angles. Equation 1 can also be applied to calculate first order periods of moiré patterns from hexagonal lattices, which can be imagined as constructed by two additional sets of equidistant lines rotated by 60 and 120° with respect to the first set. Given the hexagonal symmetry, eq 1 is in this case valid for angles $0 < \theta \leq 30°$; for $\theta \geq 30°$, the angle θ_{eq} plugged into eq 2 instead of θ must satisfy $0° \leq \theta_{eq} = |n\cdot 60° - \theta| \leq 30°$ (the absolute value is taken), with the appropriate choice of the integer n. $\theta_{eq} = 0°$ means that there is no finite moiré pattern. In our case, a and b are identical to the period of the ground hexagonal structure (20 nm) and D is 78 nm. The rotational angle of 46° found in eq 1 is equivalent to $\theta_{eq} = 14°$. From eq 2, a period of D = 82 nm can be calculated, which compares quite well with the measured period of 78 nm from Figure 6c. Figure 6d shows a model for the moiré pattern created by two identical hexagonal structures rotated by 14° relative to each other. After a low-pass image filtration, the pattern transforms into the blurred pattern of Figure 6e, which is reminiscent of the etched pattern in Figure 6c. Blurring simulates lateral etching.

The model moiré pattern in Figure 6d shows dual structure: the larger structure period is characterized by D. This larger structure is decorated by varying arrangements of the dots from the ground structures. We could not discern the smaller scale decoration by larger magnification SEM imaging of the moiré pattern in Figure 6c; however, we were able to discern transferred moiré patterns showing dual structures on other samples, as shown in Figure S5 of the Supporting Information. Better control on mask superimposition that would allow transfer of predictable moiré patterns onto substrates is one of the scopes of ongoing work in our group.

OUTLOOK

In conclusion, we have presented a conceptually simple method for ex situ fabrication of nanolithography masks from prealigned block copolymer samples. The formation of highly regular hexagonal patterns of 10 nm holes with a principal spacing of 20 nm on silicon substrate was demonstrated, covering areas in excess of 1000 μm^2. The formation of elliptical patterns by utilization of masks cut out of the same monolithic nanoporous precursor at an angle of 45° relative to the pore axes was also shown. Last but not least we have demonstrated the first lithographic moiré pattern transfer from double-layer hexagonal masks onto the substrate.

Our "cheese-cutting" method allows a very high degree of order in the template alongside unprecedented flexibility in the choice of surface due to the fact that the self-assembly does not depend on the properties of the surface. The template structures are predictable and immune from thermally generated defects; such defects can become a fundamental limitation for the minimum feature spacing accessible by directed self-assembly of block copolymer thin films.[33] On the negative side the presented method is unlikely to be scalable to length scales exceeding a few millimeters. This notwithstanding, the demonstrated pattern transfer renders the method applicable to many research tasks requiring nanopatterning of 10^3 to 10^5 μm^2 substrate areas and allows us to produce and investigate with relatively simple and cheap equipment unique patterns and patterning of devices in a way that could become relevant for applications in the future.

ASSOCIATED CONTENT

Supporting Information

Details of the experimental procedure and one figure showing AFM and SEM images of additional patterns transferred on silicon in the presence of our masks. The Supporting Information is available free of charge on the ACS Publications website at DOI: 10.1021/acs.langmuir.5b00482.

AUTHOR INFORMATION

Corresponding Authors

*S.N.: E-mail: sond@nanotech.dtu.dk. Tel: +45 4525 8146.
*V.S.: E-mail: vish@nanotech.dtu.dk. Tel: +45 4525 8147.

Notes

The authors declare no competing financial interest.

ACKNOWLEDGMENTS

The Danish National Research Foundation has funded the Center for Nanostructured Graphene (CNG, DNRF58). Microtoming was done at Dept. of Chem. Eng. at DTU. Dry etching and electron microscopy were done at DTU Danchip.

REFERENCES

(1) Bates, F. S. Block Copolymer Thermodynamics: Theory and Experiment. *Annu. Rev. Phys. Chem.* **1990**, *41*, 525−557.
(2) Castelletto, V.; Hamley, I. W. Morphologies of block copolymer melts. *Curr. Opin. Solid State Mater. Sci.* **2004**, *8*, 426−438.
(3) Gu, X.; Gunkel, I.; Russell, T. P. Pattern transfer using block copolymers. *Philos. Trans. R. Soc., A* **2013**, *371*, 20120306.
(4) Takenaka, M.; Hasegawa, H. Directed self-assembly of block copolymers. *Curr. Opin. Chem. Eng.* **2013**, *2*, 88−94.

DOI: 10.1021/acs.langmuir.5b00482
Langmuir 2015, 31, 6245−6252

(5) Jeong, S.-J.; Kim, J. Y.; Kim, B. H.; Moon, H.-S.; Kim, S. O. Directed self-assembly of block copolymers for next generation nanolithography. *Mater. Today* **2013**, *16*, 468−476.
(6) http://www.itrs.net/ITRS%201999-2014%20Mtgs,%20Presentations%20&%20Links/2013ITRS/2013Chapters/2013Litho_Summary.pdf.
(7) Bai, J.; Zhong, X.; Jiang, S.; Huang, Yu; Duan, X. Graphene nanomesh. *Nat. Nanotechnol.* **2010**, *5*, 190−194.
(8) O'Driscoll, B. M. D.; Kelly, R. A.; Shaw, M.; Mokarian-Tabari, P.; Liontos, G.; Ntetsikas, K.; Avgeropoulos, A.; Petkov, N.; Morris, M. A. Achieving structural control with thin polystyrene-*b*-polydimethylsiloxane block copolymer films: The complex relationship of interface chemistry, annealing methodology and process conditions. *Eur. Polym. J.* **2013**, *49*, 3445−3454.
(9) Mansky, P.; Liu, Y.; Huang, E.; Russell, T. P.; Hawker, C. Controlling Polymer-Surface Interactions with Random Copolymer Brushes. *Science* **1997**, *275*, 1458.
(10) Huang, W.-H.; Chen, P.-Y.; Tung, S.-H. Effects of Annealing Solvents on the Morphology of Block Copolymer-Based Supramolecular Thin Films. *Macromolecules* **2012**, *45*, 1562−1569.
(11) Lee, D. H.; Cho, H.; Yoo, S.; Park, S. Ordering evolution of block copolymer thin films upon solvent-annealing process. *J. Colloid Interface Sci.* **2012**, *383*, 118−123.
(12) Paradiso, S. P.; Delaney, K. T.; García-Cervera, C. J.; Ceniceros, H. D.; Fredrickson, G. H. Block Copolymer Self Assembly during Rapid Solvent Evaporation: Insights into Cylinder Growth and Stability. *ACS Macro Lett.* **2014**, *3*, 16−20.
(13) Morkved, T. L.; Lu, M.; Urbas, A. M.; Ehrichs, E. E.; Jaeger, H. M.; Mansky, P.; Russell, T. P. Local Control of Microdomain Orientation in Diblock Copolymer Thin Films with Electric Fields. *Science* **1996**, *273*, 931−933.
(14) Singer, J. P.; Gotrik, K. W.; Lee, J.-H.; Kooi, S. E.; Ross, C. A.; Thomas, E. L. Alignment and reordering of a block copolymer by solvent-enhanced thermal laser direct write. *Polymer* **2014**, *55*, 1875−1882.
(15) Sagelman, R. A.; Yokoyama, H.; Kramer, E. J. Graphoepitaxy of Spherical Domain Block Copolymer Films. *Adv. Mater.* **2001**, *13*, 1152−1155.
(16) Jeong, S.-J.; Moon, H.-S.; Kim, B. H.; Kim, J. Y.; Yu, J.; Lee, S.; Lee, M. G.; Choi, H. Y.; Kim, S. O. Ultralarge-Area Block Copolymer Lithography Enabled by Disposable Photoresist Prepatterning. *ACS Nano* **2010**, *4*, 5181−5186.
(17) Angelescu, D. E.; Waller, J. H.; Adamson, D. H.; Deshpande, P.; Chou, S. Y.; Register, R. A.; Chaikin, P. M. Macroscopic Orientation of Block Copolymer Cylinders in Single-Layer Films by Shearing. *Adv. Mater.* **2004**, *16*, 1736−1740.
(18) see *e.g.* Peinemann, K.-V.; Abetz, V.; Simon, P. F. W. Asymmetric superstructure formed in a block copolymer via phase separation. *Nat. Mater.* **2007**, *6*, 992−996.
(19) Schulte, L.; Grydgaard, A.; Jakobsen, M. R.; Szewczykowski, P. P.; Guo, F.; Vigild, M. E.; Berg, R. H.; Ndoni, S. Nanoporous materials from stable and metastable structures of 1,2-PB-*b*-PDMS block copolymers. *Polymer* **2011**, *52*, 422−429.
(20) Keller, A.; Pedemonte, E.; Willmouth, F. M. Macro-lattice from Segregated Amorphous Phases of a Three Block Copolymers. *Nature* **1970**, *225*, 538−539.
(21) Tepe, T.; Schulz, M. F.; Zhao, J.; Tirrell, M.; Bates, F. S.; Mortensen, K.; Almdal, K. Variable Shear-Induced Orientation of a Diblock Copolymer Hexagonal Phase. *Macromolecules* **1995**, *28*, 3008−3011.
(22) Guo, F.; Andreasen, J. W.; Vigild, M. E.; Ndoni, S. Influence of 1,2-PB Matrix Cross-Linking on Structure and Properties of Selectively Etched 1,2-PB-*b*-PDMS Block Copolymers. *Macromolecules* **2007**, *40*, 3669−3675.
(23) Park, M.; Harrison, C.; Chaikin, P. M.; Register, R. A.; Adamson, D. H. Block copolymer lithography: periodic arrays of $\sim 10^{11}$ holes in 1 square centimeter. *Science* **1997**, *276* (5315), 1401−1404.
(24) Zeng, Z.; Huang, X.; Yin, Z.; Li, H.; Chen, Y.; Li, H.; Zhang, Q.; Ma, J.; Boey, F.; Zhang, H. Fabrication of Graphene Nanomesh by Using an Anodic Aluminum Oxide Membrane as a Template. *Adv. Mater.* **2012**, *24*, 4138−4142.
(25) Ndoni, S.; Papadakis, C. M.; Bates, F. S.; Almdal, K. Laboratory-scale setup for anionic polymerization under inert atmosphere. *Rev. Sci. Instrum.* **1995**, *66*, 1090−1095.
(26) Studler, D.; Gnaegi, H. Minimal compression of ultrathin sections with use of an oscillating diamond knife. *J. Microsc.* **2000**, *197*, 94−100.
(27) Gopalakrishnan, N.; Sagar, K. S.; Christiansen, M. B.; Vigild, M. E.; Ndoni, S.; Kristensen, A. UV patterned nanoporous solid-liquid core waveguides. *Opt. Express* **2010**, *18*, 12903−12908.
(28) Kitagawa, K. Thin-film thickness profile measurement by three-wavelength interference color analysis. *Appl. Opt.* **2013**, *52*, 1998−2007.
(29) Knoll, A.; Magerle, R.; Krausch, G. Phase behavior in thin films of cylinder-forming ABA block copolymers: Experiments. *J. Chem. Phys.* **2004**, *120*, 1105−1116.
(30) Strawhecker, K. E.; Kumar, S. K.; Douglas, J. F.; Karim, A. The Critical Role of Solvent Evaporation on the Roughness of Spin-Cast Polymer Films. *Macromolecules* **2001**, *34*, 4667−4672.
(31) Luchnikov, V.; Kondyurin, A.; Formanek, P.; Lichte, H.; Stamm, M. Moirè Patterns in superimposed Nanoporous Thin Films Derived from Block-Copolymer Assemblies. *Nano Lett.* **2007**, *7*, 3628−3632.
(32) Oster, G.; Wasserman, M.; Zwerling, C. Theoretical Interpretation of Moirè Patterns. *J. Opt. Soc. Am.* **1964**, *54*, 169−175.
(33) Mishra, V.; Fredrickson, G. H.; Kramer, E. J. Effect of Film Thickness and Domain Spacing on Defect Densities in Directed Self-Assembly of Cylindrical Morphology Block Copolymers. *ACS Nano* **2012**, *6*, 2629−2641.

DOI: 10.1021/acs.langmuir.5b00482
Langmuir 2015, 31, 6245−6252

Supporting Information for the manuscript:

Transfer of direct and moiré patterns by reactive ion etching through ex-situ fabricated nanoporous polymer masks

Violetta Shvets, Thomas Hentschel, Lars Schulte, Lisa K. Tschammer, Alberto Cagliani, Peter Bøggild, Kristoffer Almdal and Sokol Ndoni*.*

*Authors to whom correspondence should be addressed. E-Mail: sond@nanotech.dtu.dk, vish@nanotech.dtu.dk; Tel.: +45 4525 8146, +45 4525 8147.

Details on the experimental conditions

Preparation of the nanoporous monolith. Block copolymer and 1% mole fraction of cross-linker relative to double bonds were co-dissolved in THF and cast into a flat-bottom Petri dish; after solvent evaporation under nitrogen flow, the paste-like block copolymer was squeezed between two microscope glasses equipped with 1 mm spacers and shear-aligned mechanically by hand. The glasses were moved back and forth relative to each other with 5 mm amplitude and 0.2 Hz frequency for 15 cycles. The shear-aligned samples were cross-linked for 2 hours at 140° C under nitrogen atmosphere. Quantitative etching of the PDMS block was then performed by TBAF in THF at room temperature for 48 hours.

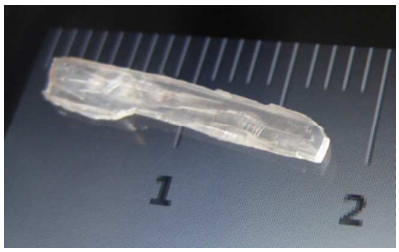

Figure S1. Photo of the nPB monolith. Ruler shows length in cm.

Microtoming. After proper trimming samples were sectioned at the resonance frequency (26.2 kHz) with amplitudes 3-6 V, feed 30-50 nm, sectioning speed 0.6 mm/s and at an angle of 6°.

Estimated size of the full section of the monolith is 1mm x 1mm. Shearing provides mechanical energy to the system and removes all local extremes responsible for domain borders. However the polymer melt close to the interface with the glass plates moves with a smaller amplitude and alignment is not as

effective there. A SEM image of a flake microtomed from the interface region with glass is shown in Figure S2.

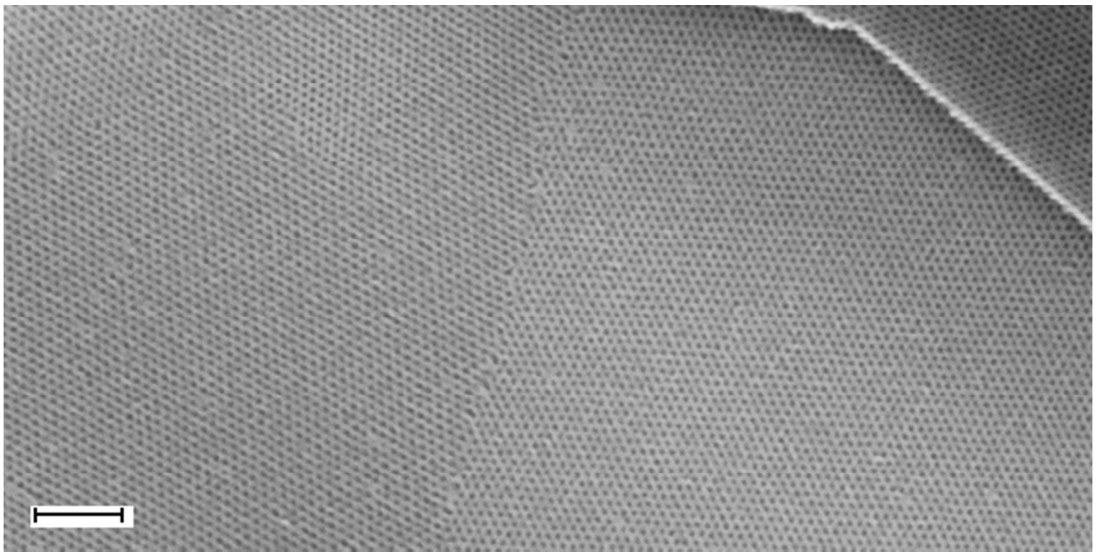

Figure S2. SEM of nanoporous flake from the interface with the glass. At least three domains with different orientations are distinguished. 200 nm scale bar.

The varying alignment of the domains in fig. S2 is most probably the source of the SAXS pattern observed in the xy plane in Fig. 1, as will be explained shortly. Figure S3 shows the 2D (first row) and integrated 1D scattering profiles (second row) observed at the three Cartesian projections highlighted in the third row. All the Bragg planes of the hexagonal structure shown at the bottom of fig. S3 are active small angle scatterers at the yz projection (comprising the equivalent Bragg planes obtained by 60º and 120º rotation relative to the shown ones). The expected scattering peaks listed in Table S1 are all observed in the 2D and 1D yz scattering profiles. The horizontal set of principal Bragg planes are the only expected active SAXS scattering planes at the xz projection, which is also confirmed by the 2D and 1D xz profiles. The only Bragg planes ideally expected to be active at the xy projection would be the vertical set of $d(11)$ planes shown at the bottom image. Therefore the ideal xy scattering should show peaks exclusively at $q = n\ 3^{½}\ q^*$, with n an integer (n = 1, 2, 3 …). However we observe additional scattering peaks at $q = q^*$ and $q = 7^{½}\ q^*$, which we interpret as due to misalignments, such as the ones observed at the glass interfaces (fig. S2). It has to be noticed that the scattering intensity of the main peak q^* on the xy plane is 200-400 times weaker than the

corresponding intensities in the yz and xz planes, which is in line with a small fraction of the material being misaligned.

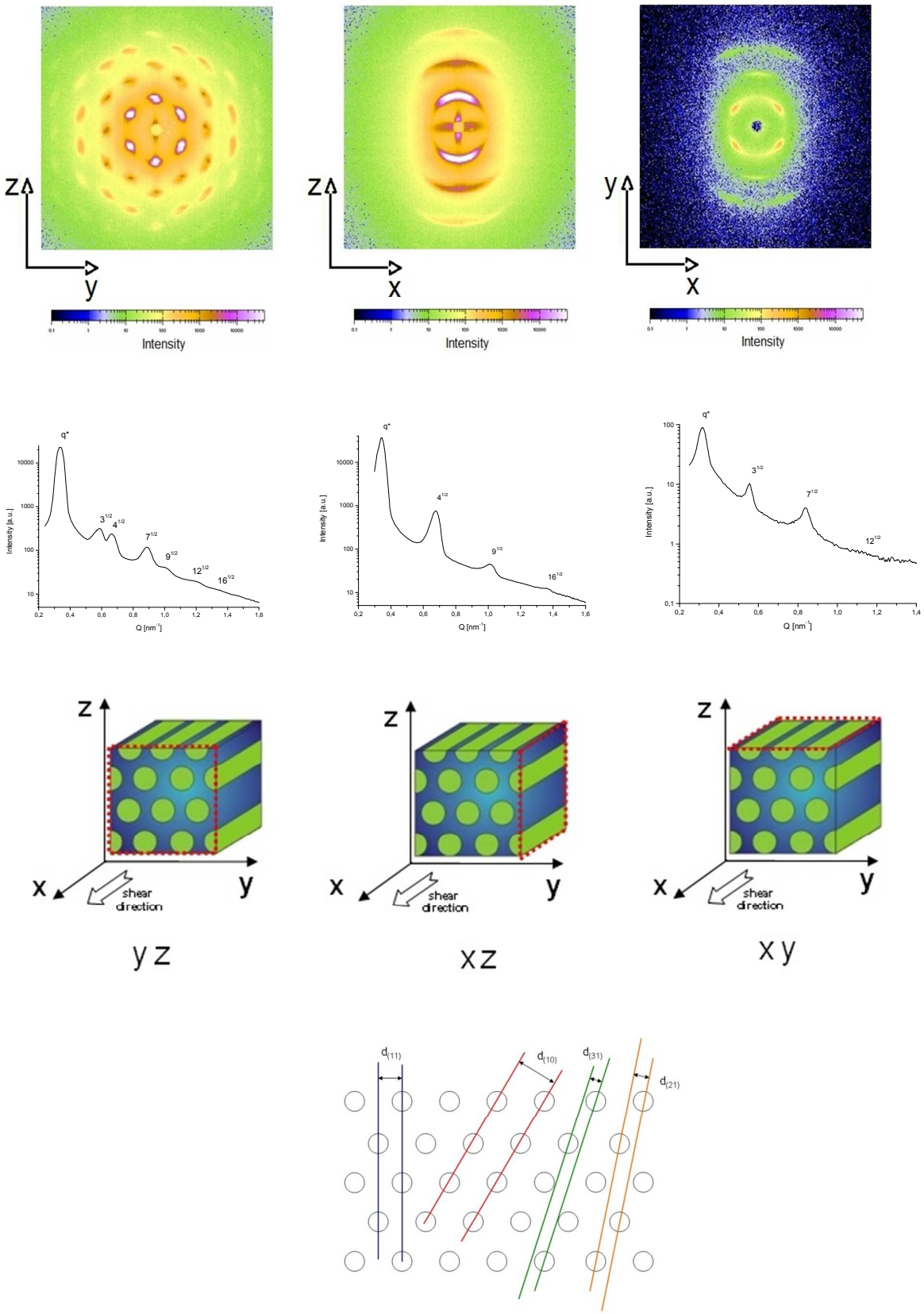

Figure S3. SAXS data of the shear-aligned nanoporous 1,2-PB samples. First row: 2D scattering patterns at the three main projections, as highlighted in the ideal alignment case in the third row. Second row: Radially integrated SAXS profiles from the respective 2D scattering profiles. Fourth row: Schematic representation of the Bragg planes for a hexagonal structure, corresponding to the yz projection above.

Table S1. Characteristic Bragg planes in a hexagonal structure

Plane	**(10)**	**(11)**	**2*(10)**	**(21)**	**3*(10)**	**2*(11) = (31)**	**4*(10)**
Ratio	$d_{(10)}/d_{(10)}$	$d_{(11)}/d_{(10)}$	$d_{(10)}/2*d_{(10)}$	$d_{(21)}/d_{(10)}$	$d_{(10)}/3*d_{(10)}$	$d_{(11)}/2*d_{(10)}$	$d_{(10)}/4*d_{(10)}$
Relative spacing	**1**	$\mathbf{3}^{-1/2} = 1/\sqrt{3}$	$\mathbf{4}^{-1/2}$	$\mathbf{7}^{-1/2}$	$\mathbf{9}^{-1/2}$	$1/(2*\sqrt{3}) = \mathbf{12}^{-1/2}$	$\mathbf{16}^{-1/2}$

The misaligned parts were removed by appropriate trimming and masks were cut only from the middle section of the monolith; all edges of the sample were cut away obtaining samples shaped as truncated rectangular pyramids with the front face of dimensions ~200 µm x 300 µm. Sections were picked up with a home-made loop. A water droplet with the polymer slices kept on the surface by surface tension is lifted by the loop out of the reservoir of the microtome knife, and deposited onto the silicon wafer. Standard workflows for trimming procedure and for picking up floating sections with the loop can be found in more detail on the DiATOME web-site: https://www.diatomeknives.com/knives/trim.aspx (trimming), http://www.diatome.ch/en/products/pdf/perfectloop_flyer_ENG.pdf (picking up).

Pattern transfer. The first procedure of Reactive Ion Etching (RIE) was realized in three steps. At first flakes were treated by highly anisotropic etching with oxygen-argon plasma for 10 s (O_2:Ar 5 : 45 sccm, pressure 10 mTorr, power 30 W, mask etch rate ~1 nm/s) for cleaning of the pores and surface from possible contaminants. The second step was a 20 s isotropic silicon etching for pattern transfer (CHF_3 : SF_6 : O_2 8 : 30 : 30 sccm, pressure 36 mTorr, power 20 W, speed of silicon etch ~1 nm/s). Finally the mask was removed by 10 min oxygen plasma cleaning (O_2 : N_2 98 : 20 sccm, pressure 300 mTorr, power 100 W). Moirè patterns were observed on longer silicon etching times: 30 s and 40 s. Alternatively, the pattern transfer was performed by silicon etching for 80 s with a rate of 0.8 - 1.0 nm/s on an Inductive Coupled Plasma metal etcher (SF_6 : C_4F_8 70 : 35 sccm flow rate with ICP power 1200 W and RIE power 200 W at 1.9 Pa pressure).

Patterns of lines and slit-like features on silicon corresponding to locations close to mask folds

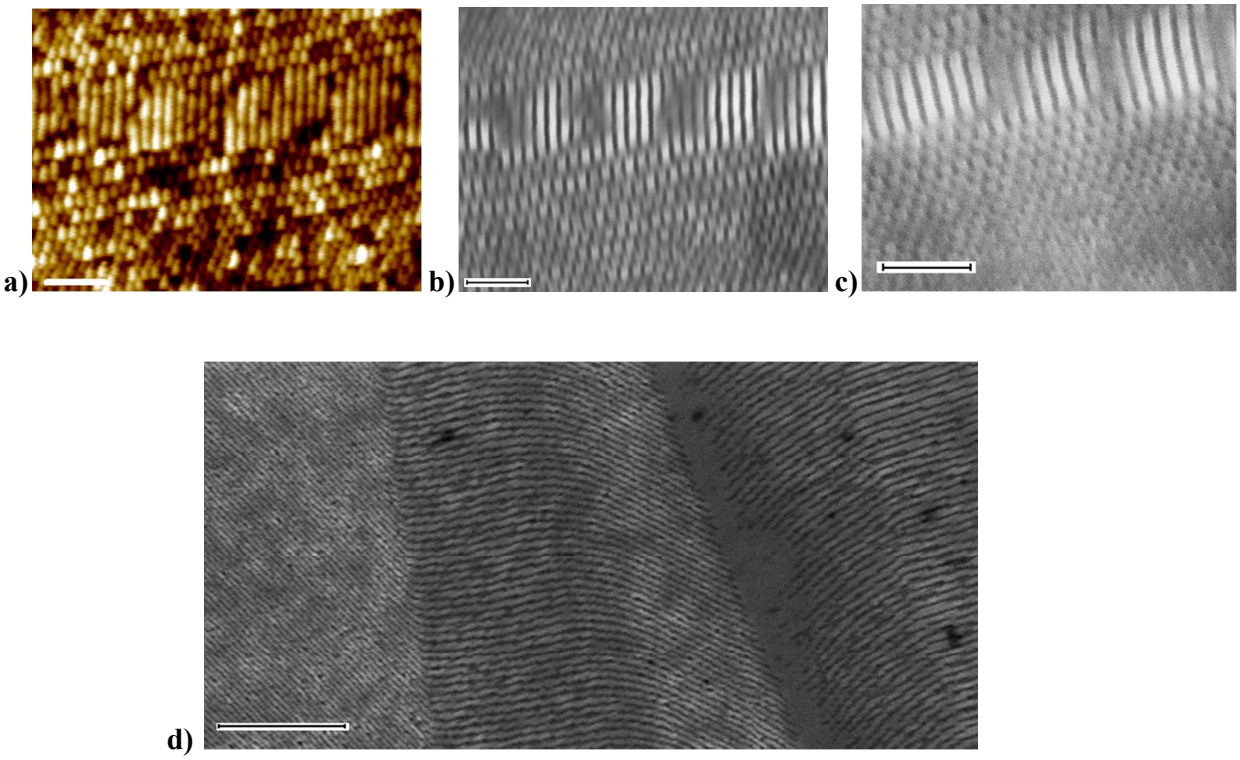

Figure S4. (a-c) slit pattern: the same location imaged by AFM, top-down SEM and SEM of sample tilted at 47°; scale bars are 200 nm. (d) SEM image taken close to a fold; 1 μm scale bar.

Line patterns:

Pattern can be transferred even from the mask cut parallel to the cylinder axis, but necessity to etch long way through the mask makes pattern less uniform and controlled than in 45° case.

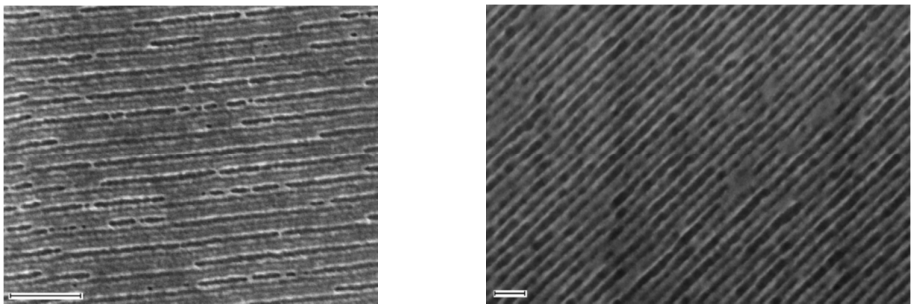

Figure S5. Polymer mask cut parallel to cylinder axis and pattern transferred to silicon, 200 nm scale bars.

Moiré patterns.

Dual structure of moiré patterns with ground period inside larger moiré structure can be observed for large period structures. At longer etching time (40s) the inner fine pattern was destroyed, while

it was retained at 30s etching. Some holes are deeper due to better coincidence of the top and bottom holes. Moire patterns are a bit squid probably because of the top flake slopping.

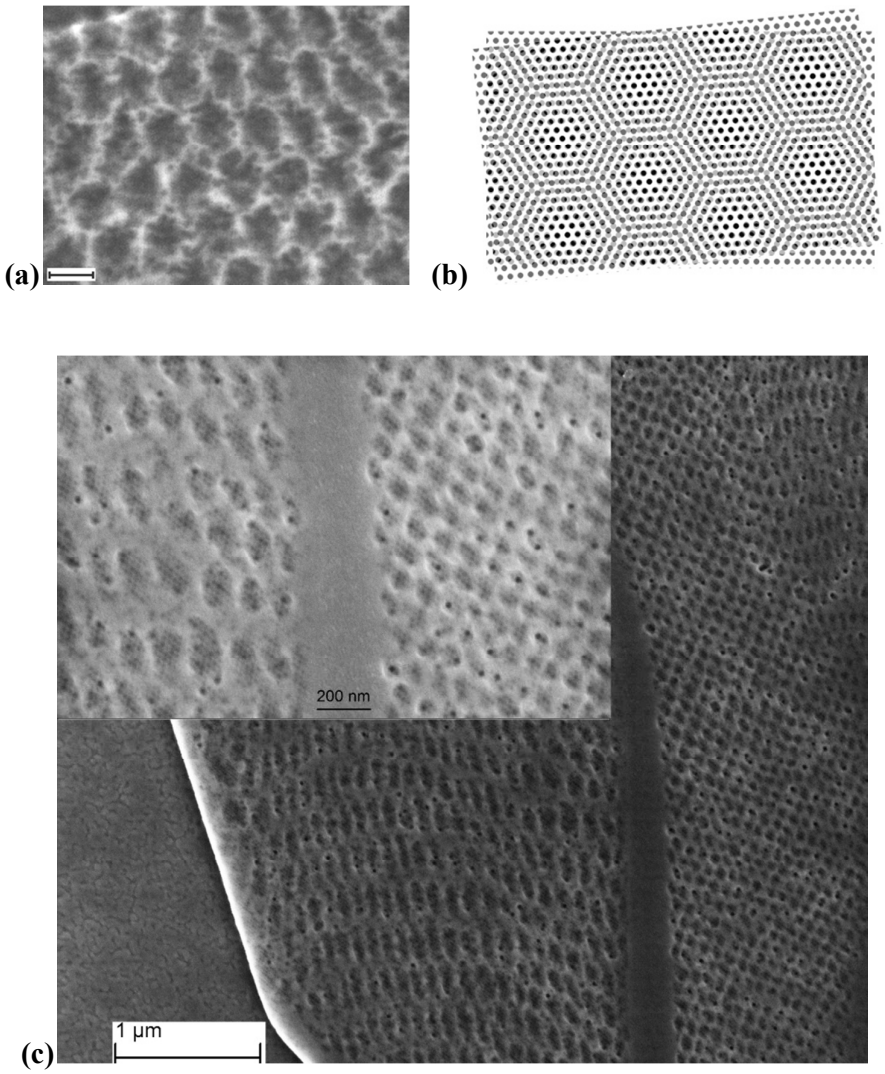

Figure S6. SEM images of moirè patterns on silicon showing dual structures. ***(a)***: 40 s etch; 200 nm scale bar. ***(b)***: Model reproducing the moiré period of the image in (a), by a roatation angle of 6º. ***(c)***: 30 s etch; the inset is a higher magnification. Dual scale patterns of different moiré spacings can be observed on the two sides of the vertical unpatterned stripe.

Appendix 2. Draft of an article on graphene. To be submitted.

Graphene patterning through ex-situ fabricated nanoporous mask.

Violetta Shvets[1,2], David Mackenzie[1,2], Lene Gammelgaard[1,2], Lars Schulte[1,2], Peter Bøggild[1,2], Kristoffer Almdal[1,2], Sokol Ndoni[1,2].

1) Technical University of Denmark, Dept. of Micro and Nanotechnology, Ørsteds Plads, Building 345 East, DK-2800 Kgs. Lyngby, Denmark;
2) Center for Nanostructured Graphene (CNG), Technical University of Denmark, Ørsteds Plads, Building 345 East, DK-2800 Kgs. Lyngby, Denmark;

Abstract.

In current work graphene nanomesh is fabricated by a novel lithography method. Lithography mask is fabricated *ex-situ* by microtoming of the pre-aligned nanoporous polymer monolith. For the monolith fabrication, block copolymer 1,2-polybutadiene-*b*-polydimethylsiloxane (PB-*b*-PDMS) with cylindrical morphology is aligned by shear, then 1,2-PB matrix is cross-linked and PDMS etched. Resulting nanoporous polymer monolith is sliced in a microtome perpendicular relative to the cylinders axis. Porous masks with hexagonally arranged holes are transferred directly on top of a chemical vapor deposition (CVD) graphene. Simple one-step etching led to fabrication of a hexagonal graphene nanomesh with a crystalline order and period 20 nm on 50x50 μm^2 scale. Masks are removed with the help of a tape. Graphene back gate device is fabricated by deposition of the metal contacts directly on top of the nanostructured graphene. Dependency of the *off* conductance from temperature indicates presence of ~20 meV gap.

Introduction.

Graphene is a single layer of the 3D graphitic crystal, an atomically thin 2D material, consisting of carbon atoms that forming a honeycomb structure. Its electronic properties include room temperature Hall effect, ballistic transport, high charge carrier mobility (200 000 cm^3/v^2, [1]) and huge sustainable currents (9108 A/cm^2). It is the best known electrical and thermal conductor [2]. Graphene is very light material with huge surface area: 2630 m^2/g [3], the strongest ever measured [4], with exceptional ability to retain its initial size after mechanical strain [5]. All these exceptional

properties made it very promising for the future post-silicon electronics [6]. But despite having all these exceptional properties, graphene application in field-effect transistors is limited due to zero bandgap.

One of the ways to open a gap and increase on/off current ratio is creation of periodic modulation on graphene [7]. Successful gap formation in graphene by patterned hydrogen adsorption [8] and by periodical rippling [9] was reported. Band gap opening in graphene is inversely proportional to the nanoribbon width/nanomesh neck [10, 11], sensitive to edge configuration, crystallographic orientation of graphene nanoribbon/mesh, edge passivation, and significant only for dimensions close to current resolution limits of lithography. Various lithography methods are utilized for formation of periodic nanoribbon arrays and nanomeshes in graphene with their advantages and disadvantages.

Lithography methods employing mask put various resists in contact with graphene and change graphene properties (charge carrier mobility, doping) [12]. Resists have to be removed completely [13] without destroying nanostructured graphene. Dense highly-ordered arrays of graphene nanoribbons can be obtained by using self-organizing properties of block copolymers. Dense graphene nanoribbon arrays of almost unidirectional orientation with few dislocations at tens microns sizes and 35 nm pitch were obtained by using of poly(styrene)-block-polydimethylsiloxane [14]. Perfectly parallel graphene nanoribbons were obtained by directed self-assembly [15], but in this method topographic features of graphoepitaxy use valuable substrate area restricting one of the nanoribbon dimensions to the 2 μm. *Son et al*. [15] reported fabrication of 12 nm and 9 nm wide graphene nanoribbon arrays with successfully opened bandgaps of 58 meV and 78 meV at 100K, respectively.

Nanomesh structures fabricated on graphene so far suffer from polycrystallinity [16, 17] and different size of the holes [18]. By using poly(styrene)-block-poly(methyl methacrylate) self-assembling properties in thin films, polycrystalline graphene nanomeshes with different dimensions were fabricated. Fabrication of graphene nanomesh has 35 nm center-to-center distance and 18 nm constriction was demonstrated in [16]. An effective energy gap of ~100 meV and on/off current ratio of ~40 at room temperature were reported. *Bai et al*. [17] have fabricated graphene manomeshes with 39 nm periodicity having neck widths of 15 nm, 10 nm, 7 nm and with 27 nm periodicity having a neck width of 9 nm, by using block copolymers with two different molecular masses and controlled overetching. An on/off current ratio exceeding 100 was measured for the

device with 7 nm neck width. Unfortunately, domain sizes in PS-b-PMMMA film are only a few microns large. A quasi-periodic nanomesh for 33 nm center-to center distance was fabricated by nanoimprinting lithography [18] with up to 140 meV bangap opening for the smallest 7 nm wide neck, but non-uniform thickness of residual level of nanoimprint resists cause a noticeable variation in the hole size.

E-beam lithography develops parallel to BCP, but it also requires coating with resists. As advantage it can give customized pattern, but resolution is still lower than for BCP: in recent work the smallest feature size realized by e-beam lithography and controlled overetching in oxygen plasma was 20 nm [19].

Alternatively maskless lithography can be used for graphene nanostructuring. These methods can utilize high-energy electrons from transmission electron microscope [20] and give sub-5nm features [21]. 15 nm and 7 nm feature sizes were produced by helium and neon ion beam microscopes, respectively [22, 23], while electrochemical etching with scanning probe lithography give resolution of few nanometers [24, 25]. The main disadvantages of these methods are low throughput, relatively high costs and difficulties in scale-up.

Here we report new method suitable for graphene nanomesh fabrication on scale of hundreds of microns with period 20 nm and 14 nm hole size. Our nanomesh does not suffer from polycrystallinity and holes have low disorder in hole size.

Results and discussion.

The procedure for graphene nanopatterning is essentially the same as the one applied for silicon nanopatterning in our previous work [26]. Figure 1 shows schematically the work flow applied. 1,2-polybutadiene-*block*-polydimethylsiloxane (PB-b-PDMS) block copolymer melt containing the small quantity of cross-linker was first aligned by shear. The bulk morphology of block copolymer consists of hexagonally packed cylinders of PDMS (minority phase) in a PB matrix. Then PB was thermally cross-linked resulting in rigid glassy monolith. The block copolymer monolith was rendered nanoporous by wet etching of PDMS in tetrabutylammonium fluoride. Masks for lithography were cut off the resulting nanoporous piece by ultra-sonic oscillating microtome perpendicular relative to the cylinder axis. 50-70 nm thick sections were deposited directly on wafer fully covered with CVD graphene. Reactive ion etching with oxygen/argon plasma completely

removes all graphene outside the mask and at the same time nanostructures nanostructures the graphene covered by mask. Then mask can be almost completely removed by applying tape. Seemingly graphene is more strongly attached to the substrate than to the mask, and remains on the wafer. At this stage it can be inspected by common characterization methods like SEM and AFM.

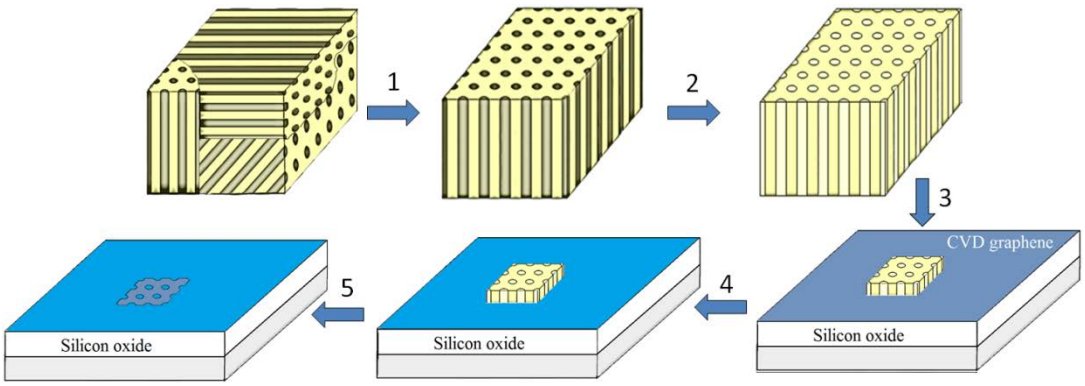

Figure 1. Work-flow of the nanolithographic process for graphene nanopatterning. (1) 1,2-PB-*b*-PDMS with random domain orientation is shear-aligned and cross-linked to fix the structure. (2) PDMS is selectively etched to get nPB. (3) nPB monolith is sliced in a microtome at room temperature. Sections transferred onto a wafer fully covered with CVD graphene. (4) Graphene etching by RIE, which transfers the pattern to the graphene under the mask and uniformly etches the graphene outside of the mask. (5) Mask removal by a tape.

An optical image of polymer mask deposited on graphene is shown in fig. 2a. The mask has an approximate size of 300x100 μm^2, within which smooth wrinkle-free regions of sizes of ~50x50 μm^2 can be found. In the insertion SEM image of the nanostructure of the nanoporous mask is shown. After etching the mask was removed by tape, and graphene is clearly visible on the substrate as a dark flake with the shape of the original mask (fig. 2 b). Some parts of the mask could not be stripped (green and yellow colors in fig. 2 b), and changed color because of attached glue from the tape. The tape also contaminated the area around the mask: the optical image shows appearance of blue patches in the bottom-left corner. The low-resolution SEM image shows (fig. 2 c) a detailed map of patterning of the graphene flake. Patches of remaining polymer mask are black in SEM. The exposed graphene has two colors: light gray as in box 1, and dark grey as in box 2. Nanostructured graphene was observed by SEM in the darker graphene regions. In the lighter grey regions no

nanopatterns were detected by SEM. Raman spectra of the light and dark are shown in fig.2.d,e, respectively. The defect D peak at ~1350 cm^{-1} is significant only for the dark areas. This finding is plausible since the light areas were covered by wrinkled portions of the mask, which hinder pattern transfer. High-resolution SEM (fig. 2 f) shows a nanomesh with period of 20 nm and with all holes of equal size ~14nm. Imaging by AFM shown in fig. 2g confirms the formation of a regular hexagonal graphene nanomesh. The period of the hexagonal structure in fig. 2 (f) and (g) coincides with that of the original nanoporous mask (fig. 2 a, insertion).

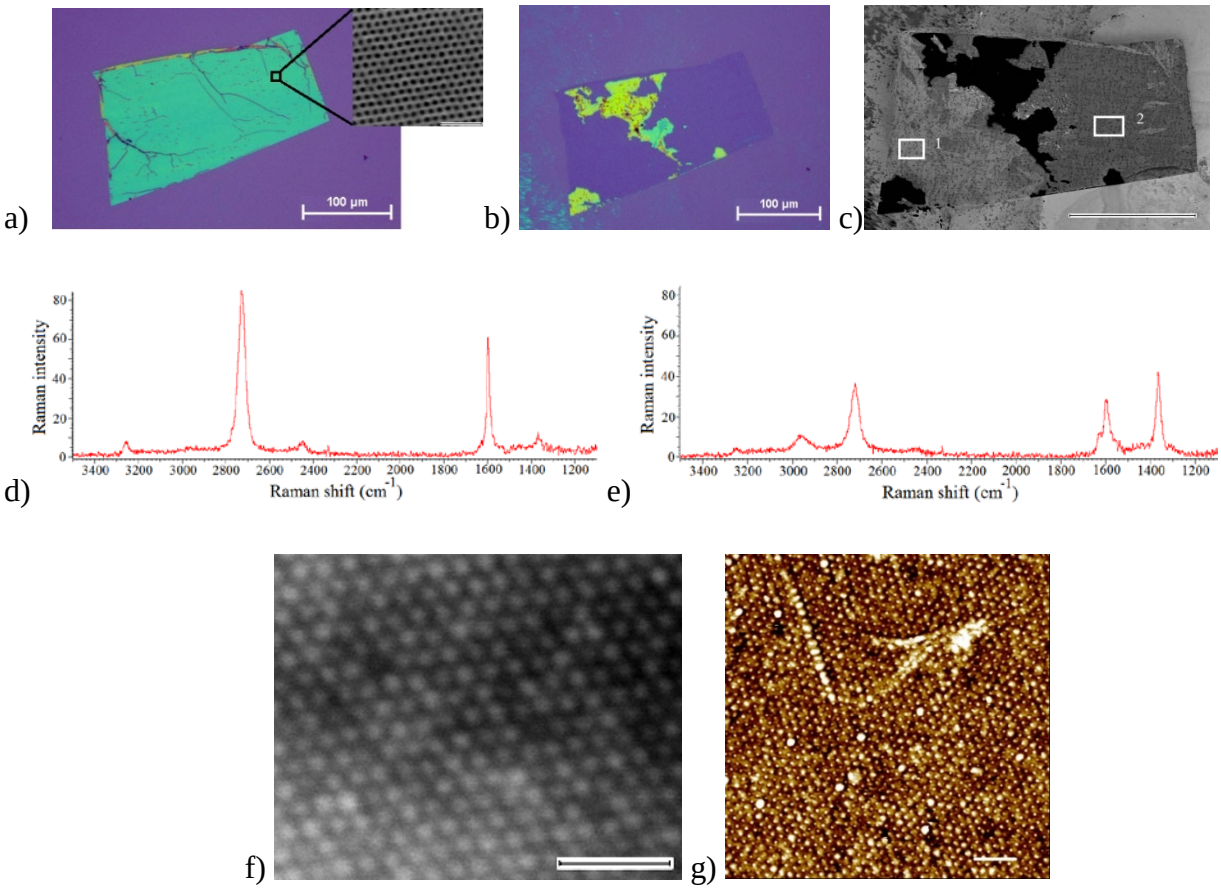

Figure 2. Images of nPB flake on the graphene. a) Optical image of nPB on graphene, insertion is mask nanostructure in SEM (100 nm scale bar); b) optical image of graphene flake after the etching and mask peeling by the tape; c) SEM image of graphene flake; Box1 shows color of unstructured region, box 2 shows color of nanostructured graphene. Scale bars for a,b,c 100 µm; d,e) Raman spectra for unstructured and nanostructured graphene. f) High-resolution graphene nanomesh in SEM and g) AFM with 100 nm scale bars.

A back-gated graphene device was fabricated for electric measurements (fig. 3).

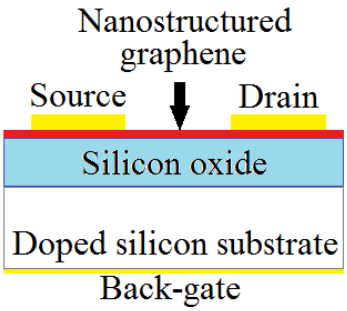

Figure 3. Schematics of fabricated back gated nanopatterned graphene device.

After the sample was annealed to remove as much of remaining contaminants as possible, stencil contacts 2/50nm Cr/Au were deposited on top of the graphene flake (fig. 4 a). A Raman map of the patterned part of the flake shows an increased D peak (fig. 4 b) and a decreased 2D to G intensity ration (fig. 4. c) due to nanopatterning. Silver paint was used to create larger contact for graphene resistance measurements (gray on fig. 4 a). The device conductance vs. gate bias was measured at different temperatures as shown in fig. 3 d. The dependence of resistance on temperature can show whether charge carriers in graphene are hopping between subgap impurity states or whether they are thermally excited between valence and conduction bands over the energy gap Δ. In hopping regime the temperature dependence of conductivity σ in 2D systems is described by [27]:

$\sigma = \sigma_0 e^{-(\frac{T_0}{T})^n}$, where

n and T_0 depend on the conduction mechanism, σ_0 is constant. Thermally activated electrical current in intrinsic semiconductor is described by:

$\sigma = \sigma_0 e^{-\frac{\Delta}{2kT}}$

If log of conductance depends linearly on (1/T) then Δ is the only fitting parameter for the slope; Δ is in such case an indication of what could be an energy gap. The results of measurements for our sample a shown in the fig. 4 e. The logarithm of the conductance is linearly dependent on 1/T with a strong correlation (coefficient $R^2 = 0.996$). Therefor the nanopatterned graphene can be considered as a thermally activated intrinsic semiconductor with a ~20 meV bandgap.

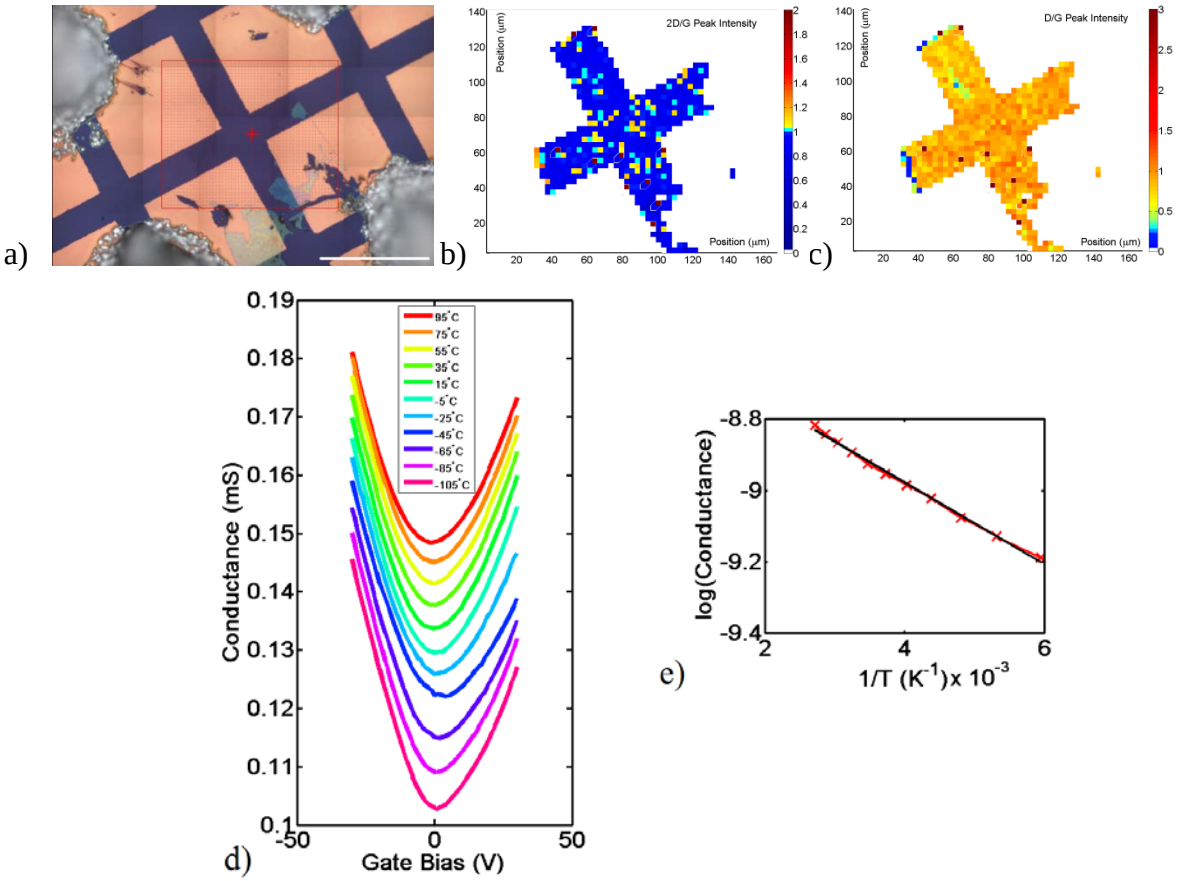

Fig. 4. a) Optical microscope image of graphene flake with stencil contacts; Red box indicates place where Raman map was taken; (b-c) Raman map of graphene device for 2D/G and D/G intensities ratios; e) conductance vs. gate voltage plot at different temperatures and e) extracted bandgap. Red crosses- experimental data, black line is 1st linear fitting attempt.

However, the temperature-dependent conductance of nanoconstricted graphene is more complex than that of an intrinsic semiconductor. It was shown, that electric transport in graphene nanoribbons is dominated by a chain of disorder-induced quantum dots with cotunneling between conductance resonances at low temperatures and activated transport at higher temperatures [28]. In order to understand the type of mechanisms contributing in the formation of the measured 20 meV gap, additional meticulous characterization is required.

Conclusions.

Graphene nanomesh with 10 nm hole size, period 20 nm and crystalline order on 50 μm extension was fabricated by pattern transfer from microtomed polymer mask. Microtome-based fabrication method has advantages over the traditional lithography methods. Method is surface-independent and mask can be easily removed by scotch tape to conduct electronic measurement. To determine mechanism of the 20 meV gap formation additional experimental research is required.

Materials and methods.

CVD graphene on the wafer with a 300 nm silicon oxide was ordered from Spanish company Graphenea.

Nanoporous polymer monolith was made of 1,2-polybutadiene-*b*-polydimethylsiloxane (PB-*b*-PDMS) block copolymer. It has molecular weight of 17800 g/mol, polydispersity index of 1.03 and mass composition of 66 : 34 PB : PDMS and was synthesized in our laboratory by living anionic polymerization. In a bulk this block copolymer has morphology of hexagonally packed PDMS cylinders in PB matrix. Dicumyl peroxide was used as cross-linker. Polymer with 1% mole fraction of cross-linker relative to double bonds was put between two parallel plates with 1mm spacer and manually shear aligned by moving plates back and forward relative to each other. Shearing orients cylinders parallel to the shearing plates with high degree of crystalline order. To fix cylinders in aligned position, PB was thermally cross-linked at 140°. Finally the PDMS block was degraded by tetrabutylammonium fluoride (TBAF) in THF. The period measured on the SEM image is 20 nm, which is 7% smaller than the period of the unetched monolith; the shrinkage could be due to structure relaxation after PDMS etching.

Nanoporous polymer pieces were sliced with an ultrasonic oscillating diamond knife from DiATOME on a Leica EMFCS ultracut UCT microtome. Samples were sliced at resonance frequency 24.9-25.3 kHz at amplitudes 1-4 V. Sections floating in the groove of the knife filled with DI water were picked up with a PERFECT LOOP and deposited directly onto CVD graphene, fully covering silicon wafer with thick oxide layer. Afterwards the sample on wafer was cleaned by rinsing in water and in isopropanol.

A Nikon ECLIPSE L200 microscope with 20x magnification lense was used for optical imaging. SEM imaging was done in a high resolution field emission Zeiss Ultra Plus SEM with a Gemini column. The scanning electron microscopy (SEM) images were obtained at acceleration voltage 5 keV in high vacuum.

Etching of graphene was performed with reactive ion etcher. Recipe for highly anisotropic etching with oxygen-argon plasma (O2 : Ar 5 : 45 sccm, pressure 10 mTorr, power 30 W, mask etch rate ~1 nm/s). Mask removal is made by scotch tape: sample is fully covered with a tape, which is pressed into the surface and then slowly pulled off together with polymer mask.

Atomic force microscopy (AFM) in tapping mode with non-contact PPP-NCHR-10 tips (purchased from nanoandmore.com) was performed on a Park System equipment XE-150 Advanced Scanning probe microscope. Images were processed with the XEI Park System Corp. Software.

References:

1. Bolotin, K. I.; Sikes, K. J.; Jiang, Z.; Klima, M.; Fudenberg, G.; Hone, J.; Kim, P.; Stormer, H. L. Ultrahigh electron mobility in suspended graphene. *Solid State Commun.*, **2008**, 146 (9-10), 351–355.

2. Novoselov, K. S.; Geim, A. K.; Morozov, S. V.; Jiang, D.; Zhang, Y.; Dubonos, S. V.; Gregorieva, I. V.; Firsov, A. A. Electric Field Effect in Atomically Thin Carbon Films. *Science*, **2004**, Vol. 306, no. 5696, 666-669.

3. Stoller, M.D.; Park, S.; Zhu, Y.; An, J.; Ruoff, R.S. Graphene-based ultracapacitors. *Nano Letters*, **2008**, 8 (10), 34983502.

4. Lee, C.; Wei, X.; Kysar, J.W.; Hone, J. Measurement of the Elastic Properties and Intrinsic Strength of Monolayer Graphene. *Science*, **2008**, 321 (5887), 385-388.

5. Frank, I. W.; Tanenbaum, D. M.; van der Zande, A. M.; McEuen, P. L. Mechanical properties of suspended graphene sheets. *J. Vac. Sci. Technol. B*, **2007**, 25 (6), 2558-2561.

6. Schwierz, F. Graphene transistors. *Nat. Nanotechnol.*, **2010**, vol. 5, 487-496.

7. Park, C. H.; Yang, L.; Son, Y. W.; Cohen, M. L.; Louie, S. G. Anisotropic behaviours of massless Dirac fermions in graphene under periodic potentials. *Nat. Phys.*, **2008**, *4* (3), 213–217.

8. Balog, R.; Jørgensen, B.; Nilsson, L.; Andersen, M.; Rienks, E.; Bianchi, M.; Fanetti, M.; Lægsgaard, E.; Baraldi, A.; Lizzit, S.; Sljivancanin, Z.; Besenbache, F.; Hammer, B.; Pedersen, T.G.; Hofmann, P.; Hornekær, L. Bandgap opening in graphene induced by patterned hydrogen adsorption. *Nature Materials*, **2010**, vol. 9, 315-319.

9. Vázquez de Parga, A. L. V.; Calleja, F.; Borca, B.; Passeggi, M. C. G.; Hinarejos, J. J.; Guinea, F.; Miranda, R. Periodically Rippled Graphene: Growth and Spatially Resolved Electronic Structure. *Phys. Rev. Lett.*, **2008**, 056807 (4).

10. Raza, H. Zigzag graphene nanoribbons: bandgap and midgap state modulation. *J. Phys.: Condens. Matter.*, **2011**, 23-382203, (5pp).

11. Hung Nguyen, V.; Chung Nguyen, M.; Viet Nguyen H.; Dollfus, P. Disorder effects on energy bandgap and electronic transport in graphene-nanomesh-based structures. *J. Appl. Phys.*, **2013**, 113, 013702.

12. Pirkle, A.; Chan, J.; Venugopal, A.; Hinojos, D.; Magnuson, C. W.; McDonnell, S.; Colombo, L.; Vogel, E. M.; Ruoff, R. S.; Wallace, R. M. The effect of chemical residues on the physical and electrical properties of chemical vapor deposited graphene transferred to SiO2. *Appl. Phys. Lett.*, **2011**, 99, 122108.

13. Lin, Y.-C.; Lu, C.-C.; Yeh, C.-H.; Jin, C.; Suenaga, K.; Chiu, P.-W. Graphene Annealing: How Clean Can It Be? *Nano Lett.*, **2012**, 12, 414–419.

14. Jiao, L.; Xie, L.; Dai, H. Densely Aligned Graphene Nanoribbons at ~35 nm Pitch. *Nano Res.*, **2012**, 5(4), 292–296.

15. Son, J.G.; Son, M., Moon, K.J.; Lee B.H.; Myoung, J.M.; Strano M.S.; Ham M.H.; Ross C.A. Sub-10 nm Graphene Nanoribbon Array Field-Effect Transistors Fabricated by Block Copolymer Lithography. *Adv Mater.*, **2013**, 25(34), 4723-4728.

16. Kim, M.; Safron, N. S.; Han, E.; Arnold, M. S.; Gopalan, P. Fabrication and Characterization of Large-Area, Semiconducting Nanoperforated Graphene Materials. *Nano Lett.*, **2010,** 10 (4), 1125–1131.

17. Bai, J.; Zhong, X.; Jiang, S.; Huang, Yu; Duan, X. Graphene nanomesh. *Nat. Nanotechnol.*, **2010**, 5, 190-194.

18. Liang, X.; Jung, Y.-S.; Wu, S.; Ismach, A.; Olynick, D. L.; Cabrini, S.; Bokor, J. Formation of Bandgap and Subbands in Graphene Nanomeshes with Sub-10 nm Ribbon Width Fabricated via Nanoimprint Lithography. *Nano Lett.,* **2010,** 10, 2454—2460.

19. Liu, L.Z.; Tian, S.B.; Long, Y.Z.; Li, W.X.; Yang, H.F.; Li, J.J.; Gu, C.Z. Tunable periodic graphene antidot lattices fabricated by e-beam lithography and oxygen ion etching. *Vacuum* **2014**, 105, 21-25.
20. Fischbein, M.D.; Drndic, M. Electron beam nanosculpting of suspended graphene sheets. *Appl. Phys. Lett.*, **2008**, 93, 113107.
21. Qi, Z. J.; Rodríguez-Manzo, J. A.; Hong, S. Ju; Park, Y. W.; Stach, E. A.; Drndic, M.; Charlie Johnson, A. T. Direct electron beam patterning of sub-5nm monolayer graphene interconnects. *Proc. of SPIE,* **2013**, 8680, 86802F-1.
22. Bell, D.; Lemme, M.; Stern, L.; Williams, J.; Marcus, C. Precision cutting and patterning of graphene with helium ions**.** *Nanotechnology*, **2009**, 20, 455301.
23. Winston, D.; Manfrinato, V.R.; Nicaise, S.M.; Cheong, L.L.; Duan, H.; Ferranti, D. Neon ion beam lithography (NIBL). *Nano Lett*, **2011**, 11, 4343–4347.
24. Tapaszto, L.; Dobrik, G.; Lambin, P.; Biro, L.P. Tailoring the atomic structure of graphene nanoribbons by scanning tunnelling microscope lithography. *Nat. Nanotechnol*., 2008, 3, 397–401.
25. Giesbers, A.; Zeitler, U.; Neubeck, S.; Freitag, F.; Novoselov, K.; Maan, J. Nanolithography and manipulating of graphene using an atomic force microscope. *Solid State Commun.*, **2008**, 147, 366–369.
26. Shvets V., Hentschel T., Schulte L., Tschammer L.K., Cagliani A., Bøggild P., Almdal K., Ndoni S. Transfer of Direct and Moiré Patterns by Reactive Ion Etching Through Ex Situ Fabricated Nanoporous Polymer Masks. *Langmuir*, **2015**, 31 (22), 6245-6252.
27. Shklovskii, B. I.; Efros, A. L. Electronic Properties of Doped Semiconductors. Springer Series in Solid State Sciences; *Springer,* Berlin, 1984; Vol. 45.
28. Dröscher, S.; Knowles, H.; Meir, Y.; Ensslin, K.; Ihn, T. Coulomb gap in graphene nanoribbons. *Phys. Rev. B*, **2011**, 84, 073405.

Published by:
DTU Nanotech
Department of Micro- and Nanotechnology
Technical University of Denmark
Ørsteds Plads, building 345B
DK-2800 Kgs. Lyngby